Field Emitters with Integrated Focusing Electrode

by

Leonard Dvorson

B.S. Physics
California Institute of Technology

Submitted to the Department of Electrical Engineering and Computer Science in Partial Fulfillment of the Requirements for the Degree of

MASTER OF SCIENCE

at the

MASSACHUSETTS INSTITUTE OF TECHNOLOGY

September 1998

© 1998 Massachusetts Institute of Technology
All rights reserved

The author hereby grants to MIT permission to reproduce and to distribute publicly paper and electronic copies of this thesis document in whole or in part.

Signature of Author_____
Department of Electrical Engineering and Computer Science
September 2, 1998

Certified by_____
Tayo Akinwande, Associate Professor of Electrical Engineering
Thesis Supervisor

Accepted by_____
A.C. Smith, Chairman, Committee on Graduate Studies

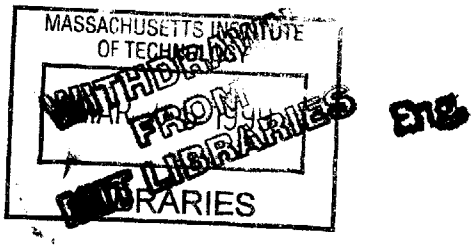

Eng.

MIT Libraries
Document Services

Room 14-0551
77 Massachusetts Avenue
Cambridge, MA 02139
Ph: 617.253.2800
Email: docs@mit.edu
http://libraries.mit.edu/docs

DISCLAIMER OF QUALITY

Due to the condition of the original material, there are unavoidable flaws in this reproduction. We have made every effort possible to provide you with the best copy available. If you are dissatisfied with this product and find it unusable, please contact Document Services as soon as possible.

Thank you.

The images contained in this document are of the best quality available.

Field Emitters with an Integrated Focusing Electrode.

by Leonard Dvorson

Submitted to the Department of Electrical Engineering and Computer Science on October 8, 1998 in Partial Fulfillment of the Requirements for the Degree of MASTER OF SCIENCE

Abstract.

Microfabricated field emission arrays (FEA) can be used to make flat panel displays (FPD) with high brightness, large viewing angle and high luminous efficiency. However, the current implementations of field emission displays (FED) require a trade-off between luminous efficiency and display resolution, which arises because of the structural / materials limitations and the consequent danger of dielectric breakdown posed by proximity focusing. The present work addresses this problem by fabricating and testing FEA with an integrated focusing electrode as well as by analytical and numerical modeling of FEA behavior.

Thesis Supervisor: Tayo Akinwande
Title: Associate Professor of Electrical Engineering

Acknowledgements

Guidance and support from Professor Tayo Akinwande of the Massachusetts Institute of Technology have helped me greatly throughout this work. His kindness and encouragement -- especially when things didn't work -- are greatly appreciated. The research specialists from the Microtechnologies Laboratory have been very helpful. Some of the fabrication and test equipment which I used for this project was built by a senior graduate student in the group, David Pflug. I am also grateful to David for his help and valuable advice on numerous occasions.

TABLE OF CONTENTS

CHAPTER 1

INTRODUCTION

1.1 Components of the Field Emission Display

Field emission devices are a promising technology for Flat Panel Displays. Like a CRT, a Field Emission Display (FED) is an *emissive* display; thus, its luminous efficiency, brightness, and viewing angle characteristics are superior to transmission-based displays, such as LCD's. Unlike a CRT, which contains a single electron gun that is scanned across the display, an FED is based on an addressable array of mini electron guns. This produces a thin and compact display suitable for use in portable technologies.

A typical FED consists of a base plate containing the addressable mini electron guns and a phosphor coated screen; the screen and the base are separated by insulating spacers. In a monochrome display, each mini electron gun addresses a single pixel on the phosphor screen. In a color display with an RGB color map, every mini electron gun is further subdivided into three or four guns, each of which addresses one of the color subpixels. (Fig. 1.1) The mini electron gun is an array of micron-sized field emitters. The cones of the field emitters have small tip radii of curvature and are centered in annular openings of the gate metal. High electric field at the cone tips result when a voltage of about 100 V is applied between the metal gate and the tip. These high fields at the tips lead to quantum mechanical tunneling of electrons from the tips.

The current emitted by a mini electron gun, composed of the electrons extracted from individual cones, is attracted to the phosphor screen by an electric field produced by a large potential difference between the anode, which is at the phosphor screen, and the

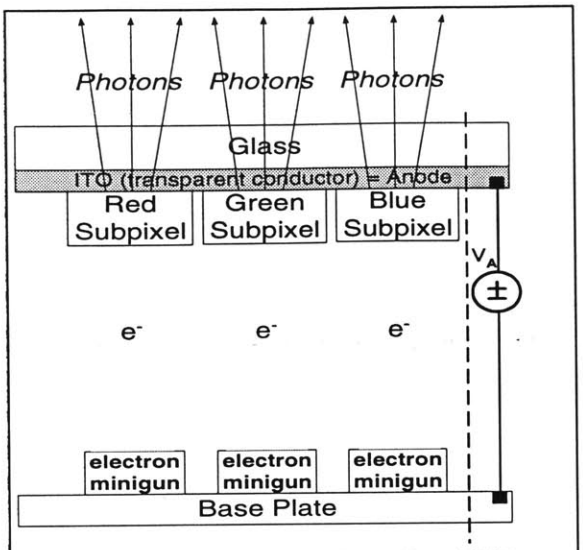

Figure 1.1 One pixel of a color FED. Subpixels are addressed by electron miniguns.

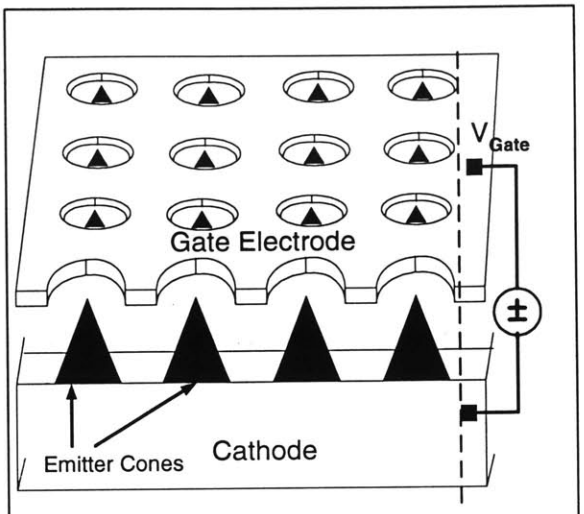

Figure 1.2 Structure of electron minigun (composed of a 4x4 array of emitters).

cathode (fig. 1.1). When emitted current is collected by the appropriate pixel on the phosphor screen, that pixel is activated and emits light. Operation of the display as a whole is achieved by periodically activating each electron gun with the appropriate voltage. This is done through a matrix addressing scheme driven by specialized control electronics.

1.2 The FED Problem of Trade-off – Brightness and Luminous Efficiency vs. Display Resolution – and Our Approach to Its Solution

Now, let's shift the discussion focus from the cathode part of a FED (field emission display) to the anode, which is the screen, specifically to the phosphor used on the screen. There are two types of phosphors -- high-voltage phosphors, which operate at 5-10 kV (i.e. require activation by electrons with energies of 5-10 keV), and low voltage phosphors, which operate at around 500 Volts. At present, in a typical commercial FED,

the cathode/anode distance is about 0.2-0.5 mm, separated by insulating spacers. (The drawbacks of increasing this distance will be described below.) The voltage difference between the cathode and the anode is thus limited to about 500 Volts, which subjects the spacers to the field of 10 kV/cm. Higher anode voltages would cause the spacers to undergo a dielectric breakdown. This necessitates the use of low-voltage phosphors in today's FED's.

High-voltage phosphors are well developed materials that have been used in TV screens and other CRT screens for several decades. In contrast, low-voltage phosphors are a new and as yet imperfect technology. Lower voltage operation of the phosphors is attained by removing the Al conducting layer. Electrons reaching the phosphor from the cathode have lower penetration depth. Thus, removal of Al allows electrons to impinge on the phosphor rather than the Al. The phosphor has lower efficiency because of the small penetration depth resulting in poor luminous efficiency due to the surface effect. Lifetime of the phosphor is based on the total charge received from the cathode. For the same brightness operation, low voltage phosphors require higher current density, resulting in lower lifetime than high voltage phosphors.

Using a high voltage phosphor in a field emission display would require increasing spacer thickness, and hence the cathode-anode separation, to about 1-2 mm The drawback of this approach arises from the fact that emitted electrons have a certain horizontal velocity, and thus follow a parabolic trajectory to the anode. As a consequence of this, horizontal displacement of the electrons is proportional to cathode-anode separation, so if the latter is increased to over 1 cm, a fraction of electrons will miss the target pixel and impinge on the neighboring one. This lowers display resolution.

We know of several factors contributing to the horizontal velocity of emitted electrons. One is implied by the uncertainty principle. Since at the instant of emission the maximum position uncertainty of the electron is equal to the circumference of the tip, the uncertainty in momentum perpendicular to the direction of emission is equal to Plank's constant over the tip circumference. Another factor arises from the thermal velocity electrons have in the instant before emission. The component of the thermal velocity directed perpendicular to the direction of emission is retained after emission. However, by far the most significant source of the horizontal velocity of emitted electrons is the fact that not all electrons are emitted vertically up. The emission beam has an intrinsic spread because electrons are emitted not only from the apex, but also from points adjacent to it, and direction of emission is in all cases perpendicular to the surface. Of course, in a regular cone with a spherical tip, emission has a sharp maximum at the apex. However, in some cases emission may also come from a local mini-protrusion on the surface near the apex and is directed away from the vertical. The extent of the effect of the last two factors depends on the tip material and shape, which in turn is determined by fabrication technology. Empirical estimations of intrinsic beam spreading put it at about 20 degree half-angle.

To summarize: the use of high voltage phosphors would necessitate increasing cathode-anode separation, leading to cross-talk between neighboring pixels, and thus lowering display resolution. Keeping the cathode-anode separation small and thus preserving display resolution, permits the use of only low-voltage phosphors, which have lower luminous efficiency and lifetime. Thus, in today FED's there exists a trade-off: luminous efficiency plus screen lifetime *vs.* screen resolution.

A way to overcome this tradeoff is to collimate the emitted electron beam by focusing. Of the two generally used ways to collimate electron beams -- magnetic focusing and electric focusing -- only electric, i.e. electrostatic focusing, can provide focusing fields of adequate strength using microscale components. Because the upper limit on the size of the electrostatic lenses to be used is imposed by the fact that at least each pixel (with sizes that could be less than 0.1 mm) – or, optimally, each emitter -- requires an individual focusing lens. A focusing device that provides a lens per pixel could be fabricated separately from the cathode and then manually installed between the cathode and the anode. Alternatively, a focusing electrode could be fabricated in the same process and the emitter tips and the gate electrode and thus be integrated with the cathode. With this approach it is possible to provide each tip with a separate focusing lens.

The present work adopts the latter approach because (a) it allows optimal focusing by providing each emitter with a separate focusing lens (b) it employs microfabrication, which automatically integrates and aligns the focus electrode to the cathode. Thus, it eliminates the need for assembly and potentially reduces the cost of production.

1.3 Thesis Outline

The rest of the thesis gives an all-sided description of this project and the results in the following sequence: first, an overview of the fabricated structure is presented, drawing attention to the underlying principles, operation modes, device structure, and important criteria. Next, Chapter 2 reviews other approaches to the same problem, providing summary and critique of the devices fabricated by other research groups.

Chapters 3-5 are devoted to presenting our work – Chapter 3 describes the analytical model of the device, which we constructed before starting fabrication. The model was intended to show the feasibility of our approach and to provide quick, intuitive insight into device operation and important issues. We believe, the model achieved both goals. Chapter 4 focuses on the main (the most time-consuming) part of this work – device fabrication. Chapter 5 presents and analyses the data collected from the devices, and compares it to the data collected by other research groups, described in Chapter II. Finally, Chapter VI gives conclusions from the research project.

1.4 Overview of Our IFE FEA – Field Emission Array with an Integrated Focusing Electrode

Pictures of the device – both a schematic and a scanning electron micrograph of the actual device – are shown on Figures 1.3 and 1.4 respectively. To understand operation of the device, consider an electron emitted from the cone tip. As mentioned above, it is an empirical fact as well as a theoretical expectation that while the greatest number of the electrons are emitted straight up, i.e. at 0 degree angle to the vertical, a number of electrons are emitted at a certain finite angle, typically up to 20 degrees. Such an electron (shown on the figure) then has a component of velocity in the x-direction. The purpose of the focus electrode is to reduce this x-velocity to zero. In a typical focusing setup, the focus electrode is biased below the gate electrode (e.g. if V_G = 100 V, V_F = 20 V). Thus, while positive charge is accumulated around the rim of the gate

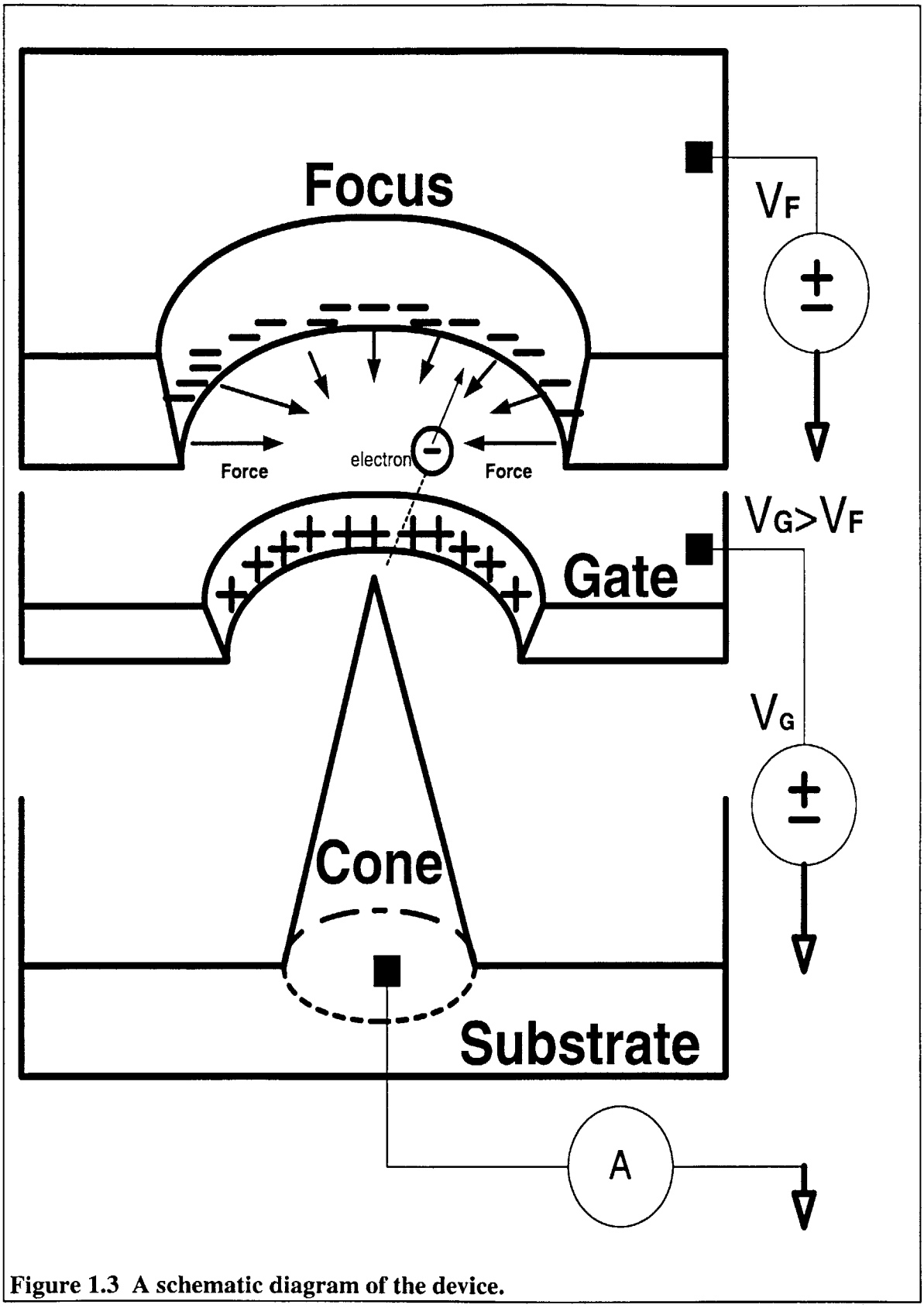

Figure 1.3 A schematic diagram of the device.

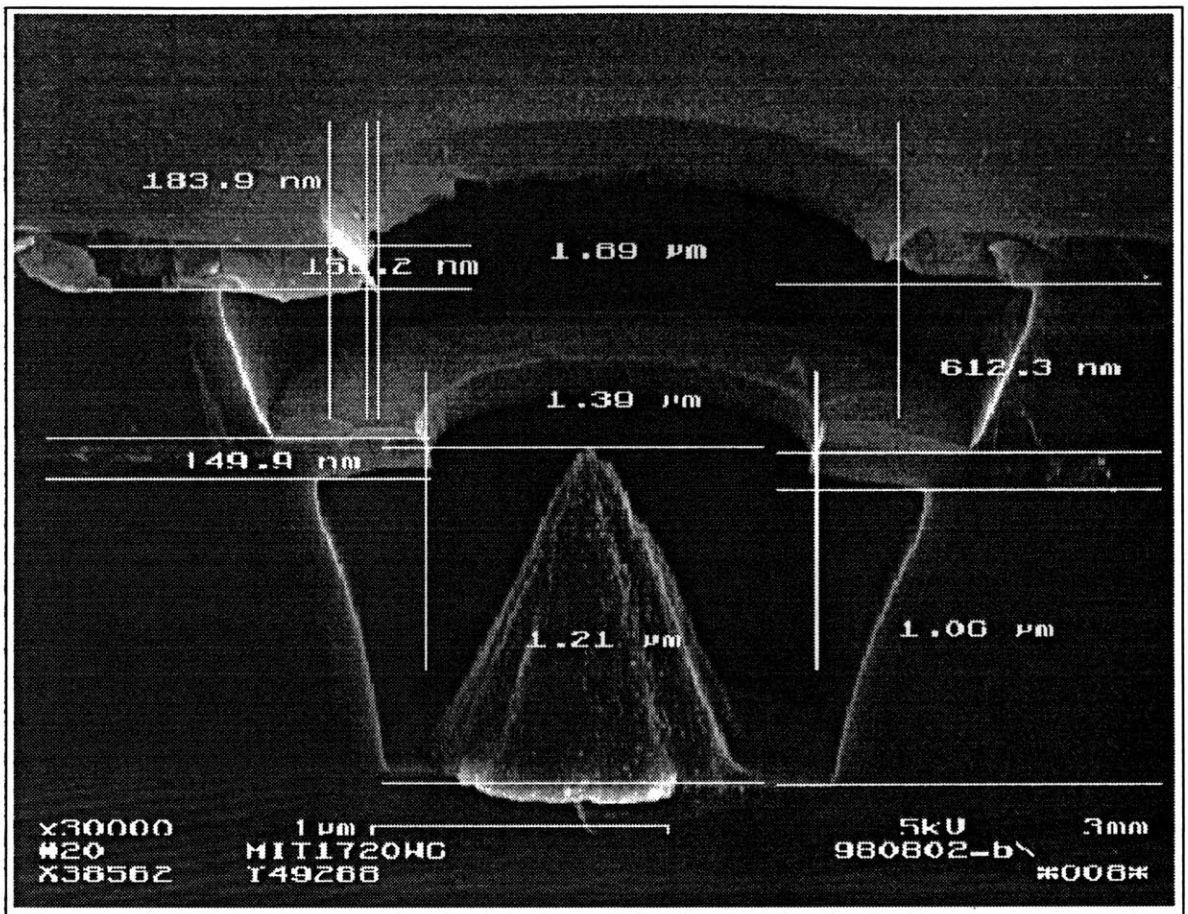

Figure 1.4 SEM micrograph of a fabricated device (with physical measurements)

electrode, negative charge is accumulated around the rim of the focus electrode. This negative charge exerts a repelling force on the emitted electron that's straying away from the center axis, providing it with the horizontal acceleration that is always directed toward the center axis. The preceding is true as long as the electron is within the focus bore or nearby – this the range of action of the focal lens. By the time electron has moved more than a few bore radii above the plane of the focus, i.e. out of the range of the focus lens, the electron's x-velocity has been considerably reduced. The electron is likely to retain a small component of it original x-velocity (which may be opposite in sign from the

original one!) which will make it follow a highly elongated parabolic trajectory until it is captured by the anode.

Having described the mechanisms behind device operation, we shift our attention to the structural parameters that affect device performance and potential problems. The two main criteria to gauge the performance of IFE FEA are emission current density and collimation of the electron beam. Emission current density depends strongly (exponentially) on the electric field at the tip, which in turn is determined by tip sharpness and gate radius, and to a large extent by the proximity and position of the focus electrode. Reducing gate radius and/or the radius of curvature of the tip can greatly increase emission current density. In fabrication, gate radius is fairly easy to control, but has a low limit, which set by lithography limitations -- about 0.5 μm for our equipment. The tip radius of curvature is much more difficult to control, especially for metal tips. One fabrication parameter that may affect tip sharpness is the temperature at which the cones are deposited. Proximity and position of the focus electrode can also be controlled in fabrication. Increasing the thickness of the gate to focus interlayer dielectric, or increasing the radius of the focus will reduce the suppressing effect that the negative charge on the focus electrode has on the field at the apex. Another approach is to position the focus, so that the tip is shielded from its field by the gate (e.g. position the focus in the same plane as the gate.)

Although the focus poses the problem of suppressing the emission current, it is also the main factor determining the second criterion of device performance – collimation of the beam. Thus, reducing the effect of the focus electrode field on the tip at the same

time reduces focusing ability. This is one of the main performance issues in IFE FEA's. It will be mentioned and discussed in more detail in subsequent chapters.

Another performance issue is interception of the emitted current by the gate and focus electrodes. Ideally, all of the emitted current would reach the anode, which would be perfect transmission or perfect collection efficiency. However, in practice this is not always the case. If emitted electrons are captured by the gate or the focus, the problem is not only the current loss at the anode, but also potential damage to electrodes resulting from electron bombardment.

Three other interrelated issues that can lead to device breakdown are (i) stray electrons charging or damaging the gate-to-focus dielectric; (ii) leakage currents in the cathode-to-gate and gate-to-focus dielectrics; (iii) dielectric breakdown in the dielectrics due to ultra high electric fields. Since typical operation voltages are on the order of 100 Volts, and the oxide isolation, as evident from figure 1.3, is only 0.5 to 1 micron thick, the oxide isolation layers have to withstand fields of 10^6 V/cm or more. Accordingly, special attention was given to obtaining quality oxides during device fabrication. This will be discussed in more detail in the fabrication chapter.

CHAPTER 2

PREVIOUS WORK – SUMMARY AND CRITIQUE

2.1 Motivation for a Focused FED and Summary of Possible Focusing Schemes.

The need to use low voltage phosphors in FED is one of the major shortcomings that prevents it from becoming a true flat CRT and achieving the brightness, luminous efficiency, and screen lifetime of the latter. A number of research efforts have aimed at overcoming this problem by implementing focusing in a FED. As explained in Chapter 1, a focused FED would not lose resolution if cathode-anode separation is increased. This means that the dielectric spacers between cathode and anode can be made thick enough to sustain the 5-10 kV voltage difference required for using high voltage phosphors. Thus, focusing is a way to overcome the current FED trade-off of luminous efficiency and screen lifetime versus display resolution.

A number of focusing schemes, summarized in Figure 2.1, have been investigated and are being developed, but so far none that we know of have been successfully implemented in the industry. Commercial field emission displays, manufactured by companies like Pixtec, for the most part still resort to what is called 'proximity focusing'. This is the method where cathode-anode separation is kept below 500 μm, thus eliminating pixel crosstalk and maintaining high display resolution. Since no additional focusing electrodes are present, we say that this method uses no active focusing (fig. 2.1). A minimal amount of focusing is implemented here by the vertical anode field, which eventually changes the electron trajectories from divergent linear into parabolic. But most of the effect comes about because the screen simply intercepts each pixel beam

before it has time to spread. The drawback of this method, as explained above, is that small distance to the anode confines the anode-cathode voltage difference to about 500 Volts, which precludes the use of high voltage phosphors. The performance limitation associated with low voltage phosphors prevents FED from achieving its full potential in the areas of brightness and luminous efficiency. The following methods, which implement active focusing, offer great improvement.

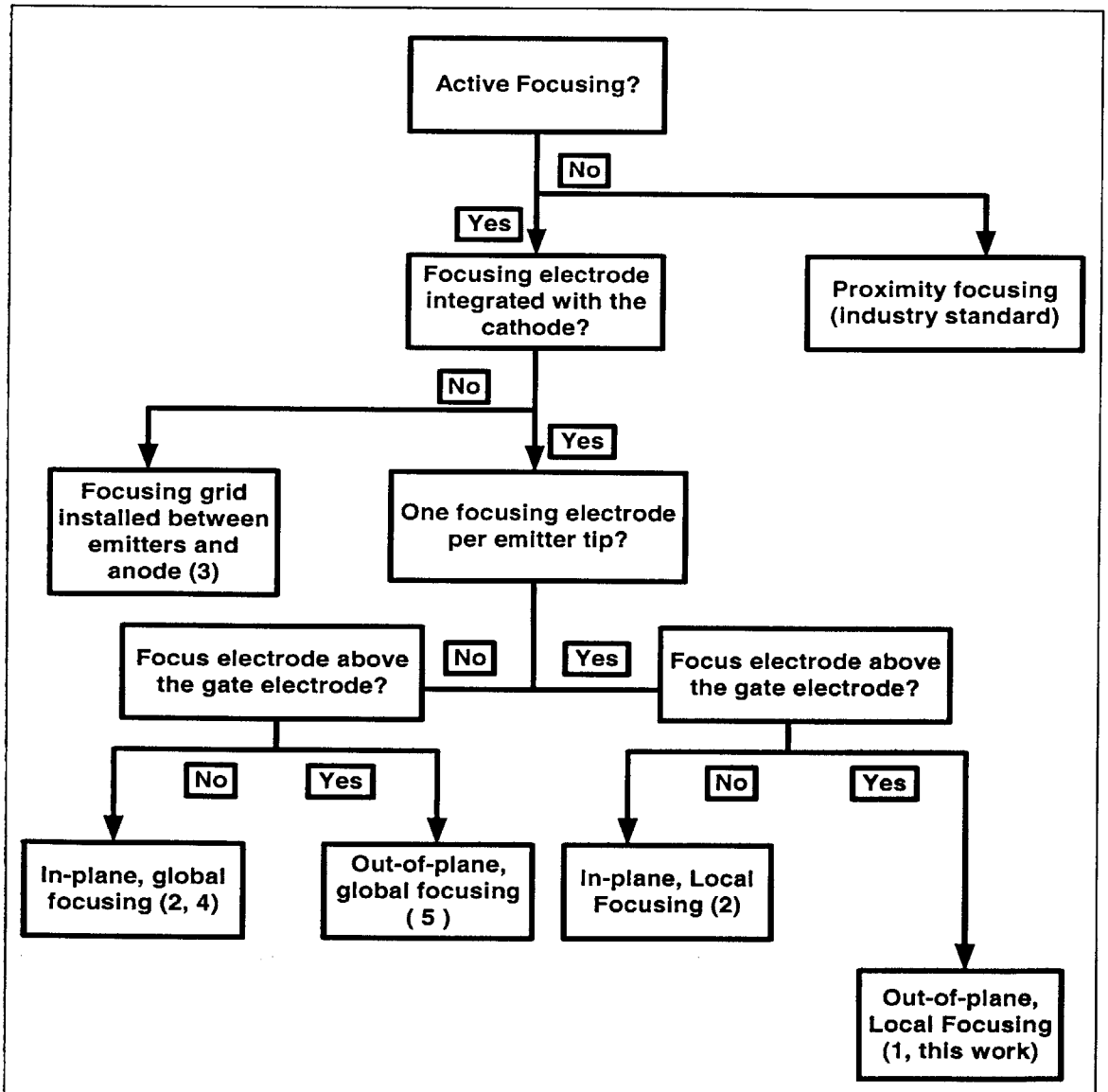

Figure 2.1. A Flowchart of the currently available FEA focusing schemes.

2.2 External Focusing Grid [1,2]

The approach adopted by Raytheon [1] uses a focus grid inserted between the cathode and the anode. There is one grid opening, 70-200 microns is diameter, for each emitter array that drives a pixel. For color displays, there is one grid opening for each color subpixel. The grid serves three functions: 1.— It directly intercepts stray electrons. 2.— It actively (electrostatically) *focuses* the beam on the screen, which is to say that spot size is less than the diameter of grid openings. Moreover, the focal point can be controlled with the voltage applied to the grid. 3.— If any positive ions are created at the anode, without the grid, they would be accelerated back to the cathode and cause damage. The grid can shield the cathode from this ion bombardment.

Electrons impinging on the grid can result in secondary electrons, some of which may reach the anode and also impair display performance. To prevent this, the authors suggest coating the focusing grid with a material which has a low coefficient of secondary electron generation, or mounting a second focusing grid above the first one and biasing it below the first one. Secondary electrons emitted from the first focusing grid have low energy and thus will be reflected by the second grid , while the electrons emitted from the cathode will make it through to the anode. The second focusing grid would also contribute to focusing the primary electron beam.

The authors demonstrated a display with a built it focusing grid [2]. A metal grid with 100 micron holes was mounted one millimeter in front of the cathode. Since the periodicity of the grid did not match that of the cathode, the tests were performed on one pixel that happened to be aligned. The anode was placed 3 mm away from the cathode (2 mm away from the grid) and biased at 3.5 kV. The gate was biased at 75 V, and the grid

was swept from 100 to 500 V. The minimum spot size (achived at the focus grid voltage of 200 V) was 30 microns, i.e. three times smaller than the grid opening. This demonstrated that the grid functions as an active electrostatic focus.

This approach has a number of strong points. In addition to the advantages described above, this device also avoids current suppression by the focus electrode – a problem in many integrated focusing schemes, where the negative charge on the focus electrode interacts with the cone and decreases the electric field at the tip, thus greatly reducing the field emission current (see below). Moreover, it doesn't have the difficulties involved in fabricating IFE FEA and doesn't have the additional problems of power dissipation and dielectric breakdown, introduced by an integrated focus. The main drawback of this method is that it does not take advantage of microfabrication. Making the FEA cathode by microfabrication, making the grid separately, and then aligning the two is intrinsically more laborious than implementing a FEA cathode together with a self-aligned focusing electrode in a single microfabrication process. Hence, this approach has an inherent cost disadvantage as compared to a process that integrates a focusing electrode by microfabrication.

2.3 IFE FEA Structures: 1. Global, in-plane focusing [3]

Now we proceed to discuss structures that have been fabricated with an integrated focusing electrode. Cha-Mei Tang et al. at NIST [3] have fabricated an in-plane global focusing structure, which has a 1x100 array enclosed between two long parallel focus electrodes. The phosphor screen is placed at 2,500 V, 10 mm above the cathode. When the gate is at 50-60 V, an unfocused image is 4-5 mm long by about 3 mm wide. With

optimal focusing (achieved for focus voltages of 3-11 V), "the full width, half maximum of the image is no more than 35 microns wide." In other words, focusing provides a factor of 10 reduction in the image dimensions. 35 microns certainly meets the requirements of today's most demanding display applications, but the present structure can only produce this result in 1D, where it can function as a local focusing structure. If several columns of emitters are placed between one pair of focusing electrodes, focusing efficiency will begin to drop, as illustrated by [4], described below. Even if one emitter could drive a pixel, there still remains a problem of crosstalk between neighboring emitters, i.e. there is a need for 2D focusing. Of course, this structure was intended mostly for study and demonstration of concept; further development is needed to make it usable in a display application.

2.4 Work of J. Itoh et al. on Silicon Tips – Global and Local In-plane Focusing and Local Out-of-Plane Focusing [4,5,6]

J. Itoh et al. at the Electrotechnical Laboratory in Japan have done perhaps the most extensive fabrication of FEA's with integrated focusing electrodes. They used silicon undercut technology to form Si tips and make various structures with global or local in-plane focusing electrodes [4], as well as out-of-plane local focusing electrodes [5]. The latter structure is identical to the one made in the present work; however, our fabrication method is completely different. It is worthwhile to describe here Itoh's fabrication method to get a better idea of his results and to look at the strengths and weaknesses of his approach. This will be presented following a brief summary of his results.

2.4.A Electrical and Optical Performance.

In the case of local, out-of-plane focusing structures, the turn-on voltage was around 60 Volts. As a typical figure for emission current, a 5x5 array produced a current of 3.2 μA at 80 V. Emitter currents followed the Fowler-Nordheim relation closely and were roughly proportional to the number of tips. The latter fact is evidence of a uniform distribution of the tip radius of curvature. Oxide resistivity was $3x10^7\ \Omega\ cm$ at the field of $2x10^6\ V/cm$. Such high quality oxide permitted stable operation with large voltage differences between gate and focusing electrodes. The authors investigated focus transfer characteristic by keeping the gate voltage at 80 V, and varying the focus voltage between 0 and 40 V. Anode current showed a roughly exponential decrease as focus voltage was reduced from 40 to 10 V; however, below 10 V, anode current abruptly decreased down to a few nanoamperes. The authors suggest that the current decrease between 40 and 10 V on the focus is due to suppression of the electric field at the tip, while the abrupt decrease below 10 V *may* be due to space charge. Current stability over time in the focusing mode (with gate voltage at 80 V, and focus voltage equal to 8 V) is rather poor. Over approx. 40 minutes the current fluctuated from 5 to 10 μA. However, in his most recent work [6], presented at IVMC 98, Itoh et al. incorporated a MOSFET transistor as a current stability control for the FEA with great results.

The optical performance of Itoh's device is excellent. With the anode at 1000 V, 20 mm above the cathode, gate voltage at 80 V, and focus voltage at 50 V, there a circular spot on the screen, about 6 mm in diameter. (For focus voltages above 50 V, the whole screen apparently lights up.) Then, as focus voltage is reduced to 40 V, then 30 V and

gradually down to 4 V, the spot size gradually decreases from 6 mm to approximately 0.5 mm, i.e. five times the original array size (100 μm x 100 μm). This more than a factor of 10 improvement, about the same as in the C.-M. Tang's work [3], described above, but here the improvement is achieved in two dimensions. However, most demanding display applications call for pixel size of under 0.1 mm. It is unclear whether this approach can achieve the ultimate limit of having the spot size equal to the array size. Special instrumentation is needed to get precise measurements of diameters of such minute light spots. In conclusion, local, out-of-plane focusing undoubtedly provides the strongest focusing of all the integrated focus geometries. However, the cost is lower emission current or, equivalently, higher operating voltage for a given current, which in turn brings up issues of power dissipation and device lifetime.

2.4.B Device Fabrication

Itoh's fabrication process begins with the growth of a thin layer of thermal oxide, which is then patterned into 2 micron diameter discs. Next, isotropic reactive ion etching of silicon is used to form silicon tips under the 2 micron oxide caps. Then, a layer of silicon oxide, SiO_x, is evaporated for gate-to-cathode isolation. Special attention was given to oxide evaporation (here and with gate-to-focus isolation oxide) to obtain an oxide film with good insulation quality. After the oxide, 0.2 μm of niobium was deposited for the gate electrode, and on top of it a layer of photoresist was patterned to prepare for opening gate contacts. Next, another layer of silicon oxide and niobium was deposited, identical to the first ones. Finally, photoresist over the gate contacts and oxide

caps on the emitter tips were lifted off by ultrasonic agitation in buffered hydrofluoric acid.

2.4.C Evaluation of the Process

The strong points of this process are that 1.— It achieves highly uniform silicon tips. 2.— It's relatively simple in that it takes only two masks and does not require angular evaporation, which calls for a special setup and – as we found out -- could be quite difficult for such stacked gate structure.

However, the process also has its drawbacks, the main one being that the gate radius is greater than or at best equal to the thickness of the gate oxide; thus, the fabricated structure has a gate diameter of 2 microns and the focus diameter of 3 microns. Large gate diameter leads to high operating voltages. (This problem may be partially overcome if the RIE etch that defines the silicon cone is made partially anisotropic). Another drawback is the inability to use thermal oxide – which has the best isolation properties – for gate isolation.

2.4.D Devices with an In-plane Focusing Electrode

Itoh et al. have applied a very similar to process to fabricating field emitters with an in-plane, global focusing electrode. They concluded that global focusing was effective for 2x2 and 1x1 arrays (1x1 is essentially a local focusing case), and inadequate for larger arrays, such as 10x10. An additional benefit of in-plane focusing electrodes is that the focus electrode is shielded by the gate electrode and does not suppress the field at the emitters. Also, the fabrication technology is simpler. The drawbacks are increased area

requirement and thus lower emitter packing density, and asymmetry of the focusing electrode, which needs to have opening for the gate contact lines. This asymmetry leads to distortion of the spots from circular to elongated.

2.5 Global Out-of-plane Focusing on Metal Tips [7] and an Attempt to Overcome Tip Field Decrease due to the Local, Out-of-Plane Focus Electrode [8]

Another globally focused structure was fabricated by Tsai et al. [7]. They used a Spindt cone process to fabricate a structure that has one square out-of-plane focusing electrode per four emitters. With the screen 5 mm away from the cathode and at 5 kV, and the gate at 60-80 V, the authors found that focusing can bring the spot size from 1.6 mm down to 0.6 mm (from 0.33 mm x 0.33 mm pixel), i.e. approx. a factor of 2.5 reduction. However, using the focus electrode also reduces the emission current by a factor of 10.

A. Hosono et al. [8] attempted to overcome the current suppresion caused by a local, out-of-plane focusing electrode. Their approach was to increase the thickness of the gate electrode from 0.3 microns to 3 microns. With gate voltage at 100 V, reducing the focus voltage to 20 V (i.e. placing the device in the focusing mode) caused the emission current to decrease by 85% in the thinner gate device, while the thicker gate device lost only 30% of its current. However, in my opinion, this improvement is achieved at the cost of impaired focusing performance. (The optimal focusing the authors could produce was a factor of 4 reduction in spot diameter, as compared to Itoh's factor of 10 reduction [5]) Emitters in the device with a 3 micron thick gate are less susceptible to the effect of the focus electrode because (i) greater separation between the tip apex and

the rim of the focus electrode (ii) depending on geometry, the tip apex may simply be shielded from the focus electrode by the upper rim of the gate electrode. However, the longer electrons travel in the divergent fields of the tip and gate, out of the influence of the focus electrode, the greater transverse velocity they will obtain and the harder it will be to focus. Moreover, if the upper rim of the gate electrode is between the focus and the tip apex and is shielding the tip, the upper rim of the gate accumulates positive charge which functions as another diverging lens and may also intercept electrons. Whether this tradeoff is worth it depends on the performance requirements and has to be verified by numerical modeling, including trajectory calculations.

2.6 Summary of Advantages and Disadvantages of Different Focusing Schemes.

Hence, each focusing scheme has its strengths and weaknesses, as summarized in table 2.1. The choice thus depends on what is deemed to be the more important FED parameters, which in turn, is often determined by the application. For example, if the best possible focusing is desired, local, out-of-plane focusing is the way to achieve it, at the cost of higher operating voltage. If, on the other hand, optimal focusing is not critical, an in-plane, local focusing scheme may do the job with a lower operating voltage, but at the cost of lower tip density (and hence lower total current). Since the primary purpose of our project was focusing the electron beam, we opted for the scheme that was expected to provide the most effective focusing. Thus, we fabricated devices with an integrated, local, out-of-plane focusing electrode.

Table 2.1. Advantages and disadvantages of various focusing schemes.

	Advantages	Disadvantages
Proximity Focusing	• simple to fabricate the cathode • adequate focusing	♦ lower luminous efficiency ♦ lower brightness ♦ shorter lifetime
External Focusing Grid	• effective focusing • protects the cathode from stray ions ejected from the anode • easier and more reliable than microfabrication of IFE at the beginning stage • focus does not reduce emission current	♦ Laborious manufacture and assembly ⇒ higher cost than IFE
Global, In-Plane IFE	• probably the easiest IFE to fabricate • focus does not reduce emission current • No gate-focus leakage or $\frac{1}{2}CV^2$ power dissipation	♦ inadequate focusing (except for 2x2 arrays) ♦ lower tip packing density ♦ asymmetry in the focusing electrode, leading to spot distortion
Global, Out-of-Plane IFE	• possibly better focusing than global, in-plane IFE	♦ inadequate focusing (except for 2x2 arrays) ♦ lower tip packing density ♦ usually harder to fabricate ♦ Greater chance of gate-focus leakage; more power dissipation; greater chance of breakdown.
Local, In-plane IFE	• easier to fabricate • focus does not reduce emission current • No gate-focus leakage or $\frac{1}{2}CV^2$ power dissipation	♦ lower tip packing density ♦ asymmetry in the focusing electrode, leading to spot distortion
Local, Out-of-plane IFE	• the most effective and efficient focusing (hence, lower focusing voltage) • higher tip packing density	♦ probably, the hardest to fabricate ♦ focus reduces emission current ⇒ higher operating voltage ♦ gate-focus leakage, power dissipation, and greater chance of breakdown (due to failure of the gate-focus isolation)

References for Chapter 2.

1. United States Patent # 5, 543,691. Granted to Palevsky et al. (Raytheon)
2. A. Palevsky et al, SID 94 DIGEST, p. 55
3. C.-M. Tang et al. SID 97 Digest, 10.1 (p. 115)
4. C. Py, J. Itoh et al. IEEE Trans. on Electron Devices, Vol. 44, No 3, March 1997
5. J. Itoh et al. J. Vac. Sci. Technol. B 13(5), Sept/Oct 1995
6. J. Itoh et al., IVMC 98 Bulletin, p. 128
7. C.H. Tsai et al., SID 97 Digest, 10.2 (p. 119)
8. A. Hosono et al., IVMC 98 Bulletin, p. 97

CHAPTER 3

DEVICE DESIGN AND MODELING

3.1 A Brief Overview of Prior Modeling Work, Numerical and Analytical.

Field emitters have been the subject of extensive numerical simulations [see for example, Refs. 1, 2, 3, and 4]. The models published to date are mostly confined to two dimensions and deal primarily with (i) emission current density and (ii) electron trajectories. In contrast, analytical modeling of field emitters has not been nearly as extensive, despite the fact that it can offer quick, intuitive insight into the key parameters that determine device performance. The only analytical model developed recently for microscopic field emitters is the "Saturn Model," from the Naval Research Labs [5]. This approach represents the FEA unit cell as a sphere in the presence of a circular ring of charge, and uses a combination of analytical and seminumerical techniques to estimate the field enhancement factor and tip to gate capacitance.

More extensive analytical investigation of electrostatics in conic geometries [6], with specific applications to macroscopic field emitters [7], was carried out in the 40's and 50's. These early models were in turn based on mathematical and theoretical electrostatics work first published in the 30's [8,9]. The article by R.N. Hall [6] became the starting point for our approach.

3.2 A Qualitative Picture of the Out-of-Plane Local IFE FED.

One aim of the model described in this chapter was to gain an intuitive, qualitative – or maybe even semiquantitative – picture of device performance and to acquire an

understanding of how it depends on various geometrical parameters of the structure. This understanding guided device design and specification of geometrical parameters. The out-of-plane, local IFE FED consists of a cone, whose tip is approximately level with the opening in the gate electrode [fig. 3.1]. Stacked above the gate electrode and centered around the same axis of symmetry is the focus electrode, which has an opening with a somewhat larger radius than the gate. Gate and focus electrodes are separated by an insulating layer. Another, thicker, insulating layer separates the gate from the cathode – the base of the cones.

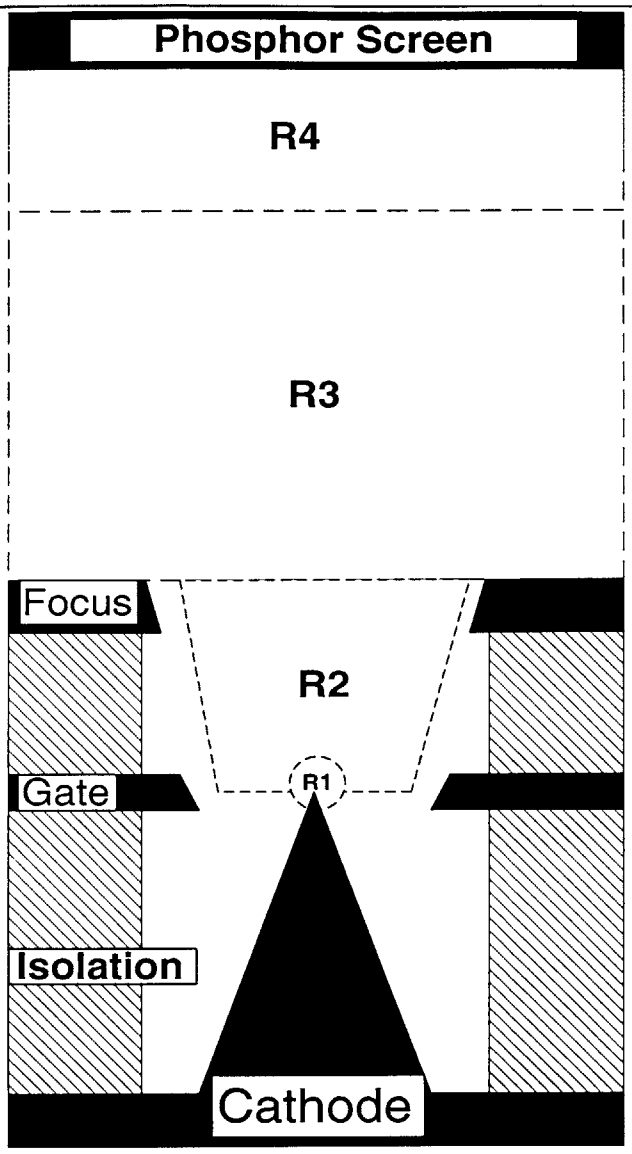

Figure 3.1. Out-of-plane, local IFE FED. Showing the regions of model validity.

Two important criteria of IFE FED performance are brightness and spot-size, i.e. resolution. Brightness, which is the amount of light emitted by the phosphor in response to the electron charge it captures, is thus directly determined by the magnitude of the emission current. Spot-size is depends on a combination of three factors (for a given

cathode-anode separation) – (i) inherent angular spread in the electron beam (ii) beam divergence by the gate aperture and (iii) focusing efficiency of the focus electrode.

The only variable parameter that controls emission current magnitude is the electric field at the apex. This field is produced by a superposition of gate and focus voltages and strongly depends on the combination of tip sharpness, defined by tip radius of curvature, and the distance from the gate to the tip, defined by the gate radius. Besides gate proximity, electric field at the tip is also affected by the proximity of the focus electrode, but in this case there is a negative correlation. That is, since there a total minus charge on the focus under normal operating conditions, the closer it is to the tip, the more it reduces the field at the tip. Tip-to-focus distance is determined by the sum of squares of the focus radius and the vertical separation between the gate and the focus, i.e. by the thickness of the gate-to-focus insulation. It has been shown that anode voltage has very little effect on the tip field.

However, if one is now tempted to design a device with a large tip-to-focus distance, there is a competing consideration. Namely, the ability to effectively focus the emitted electron beam is optimized when the focus electrode is close to the tip. This is due to three factors. First, when the focus is close to the gate and the tip, it would accumulate greater negative charge for a given value of focus voltage (due to stronger electrostatic interaction) and thus exert a stronger focusing field on the electrons. This factor, however, can be easily compensated for at higher tip-focus distances by simply lowering the focus voltage. Another factor is that the fields of the tip and the gate tend to *diverge* the electrons; thus, the sooner electrons enter the converging field of the focus electrode, the better focusing could be achieved. The last factor is related to the amount

of time the electrons spend in the focusing field. The effect of the focusing field is measured by the total x-impulse imparted to the electron, which is proportional to the time electrons spend in the focusing field.

$$I_x = \int_0^{t_{Fin}} F_x[x(t), y(t)]\,dt = e\int_0^{t_{Fin}} E_x[x(t), y(t)]\,dt$$

Since an electron is gaining vertical velocity from the moment of emission onward, the sooner it enters the focusing field, the longer it will take to traverse it. Conversely, if the focus electrode is far away from the tip, by the time the electron has entered the focusing field, it has already gained substantial vertical velocity in the field of the cone tip, and thus would traverse the focusing region very quickly. In principle, increasing anode voltage also contributes to focusing by reducing the travel time of the electrons and thus reducing the transverse spread of the beam; however, this effect is small.

3.3 A Quantitative Analytical Model for the Single Gate FED.

The preceding considerations will now be backed up and quantified with the help of an analytical model. To construct one, we first need to find a way to approximate the elements of the device with simpler geometries that would yield to an analytical solution. As indicated on Figure 3.1, there are four components to be modeled: cathode (in reality, conducting plane with a cone); gate and focus(in reality, conducting slabs with circular holes); gate-focus and gate-cathode isolation (in reality, insulating slabs with circular holes.) (We could not find a way to incorporate the isolators in the model. The error introduced by this omission is believed to be small.) Fortunately, any approximation only has to be accurate in the regions traversed by electron trajectories – the immediate

vicinity of the tip (R1 in fig. 3.1), inside the gate and focus bores and between the two electrodes (R2 in fig 3.1), within a few focus radii above the plane of the focus (R3), and high above the plane of the focus (R4).

By far the strongest fields are present in the region R1, region R2 comes second; hence, the model has to be most accurate in these areas, where electron trajectories are most strongly affected. An electron traversing regions R1 and R2 without closely approaching the electrodes sees the focus and the gate as *rings of charge*. This is the case because (a) the height of the electrodes is small compared to their radii and (b) from electrostatic considerations, most of the charge on the slanted electrode sidewalls is usually concentrated on one of the rims (e.g. on the bottom rim of the focus electrode.) Next, consider how the cone plus plane cathode appears to an electron in regions R1 or R2. By proximity argument, the cone becomes the most dominant feature of the cathode, and the effect of the underlying plane is almost negligible. Thus, it is a good approximation to model the cathode as an infinite cone, i.e. a cone with sidewalls extending infinitely far down. In spherical coordinates, an infinite cone is defined by a very simple equation:θ = constant.

Now, from the point of view of region 2, the microscopic details of the cone tip should not matter, thus the cone can first be assumed to be infinitely sharp. For simplicity, the following formulas are developed for a single electrode (the gate) and are later generalized by superposition to include the focus. An infinite cone plus a charged ring system is a well-known problem. The solution, found in electrostatics textbooks [9], is:

$$V(r < r_G, \theta) = \frac{Q_G}{4\pi\varepsilon_0 r_G} \sum_{k=0}^{\infty} \frac{P_{\nu_k}(\mu_1)}{\left(\nu_k + \frac{1}{2}\right)\int_{\mu_0}^{1}\left[P_{\nu_k}(\mu')\right]^2 d\mu'} * P_{\nu_k}(\mu) * \left(\frac{r}{r_G}\right)^{\nu_k} \quad (3.1)$$

$$V(r > r_G, \theta) = \frac{Q_G}{4\pi\varepsilon_0 r_G} \sum_{k=0}^{\infty} \frac{P_{\nu_k}(\mu_1)}{\left(\nu_k + \frac{1}{2}\right)\int_{\mu_0}^{1}\left[P_{\nu_k}(\mu')\right]^2 d\mu'} * P_{\nu_k}(\mu) * \left(\frac{r_G}{r}\right)^{\nu_k+1} \quad (3.2)$$

The parameters in the equation are defined in figure 3.2.

α -- cone half-angle, (measured from $\theta = 0$, i.e. sharp cone = large α)

r_G – radius of the charged ring that represents the gate

θ_1 – angular position of the gate ring

Q_G – charge on the gate ring

$\mu = \cos(\theta)$;

$\mu_1 = \cos(\theta_1)$;

$\mu_0 = \cos(\alpha)$; [thus, the integral in the denominator provides normalization of the Legendre function P_ν]

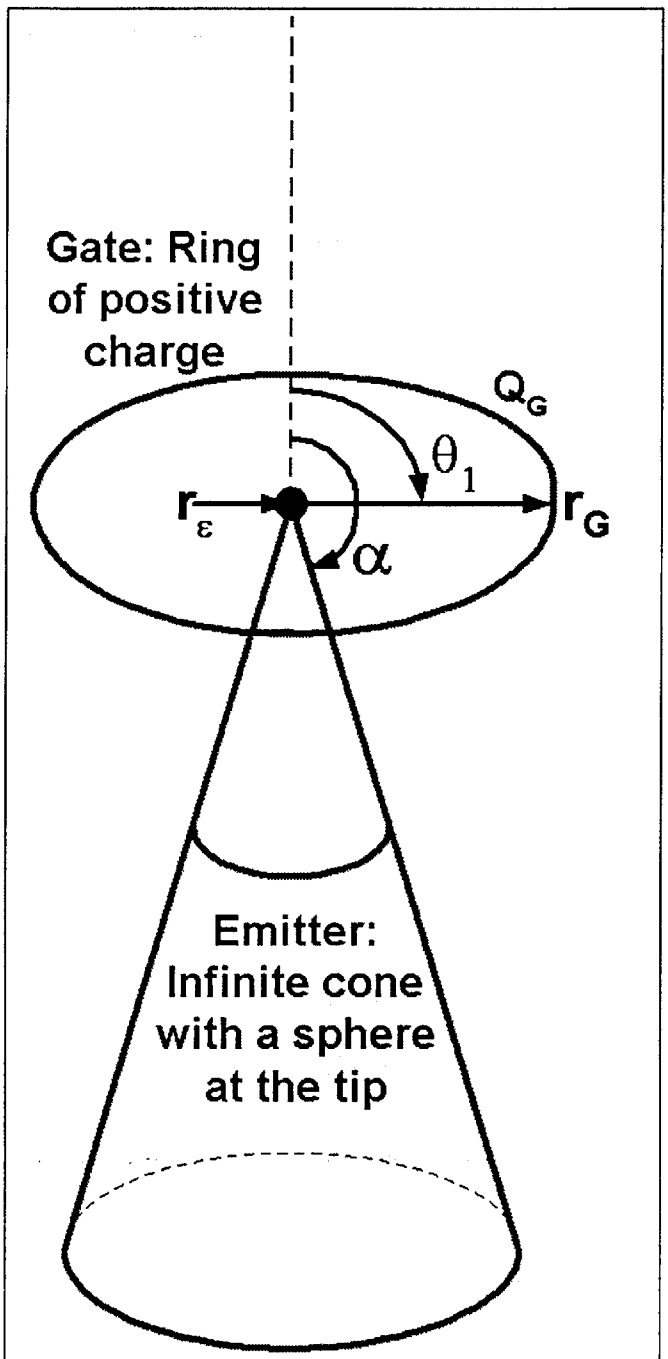

Figure 3.2. Diagram for the Analytical Model.

Obtaining the solution is for the most part straightforward. After Laplace's equation is separated in spherical coordinates, in a problem with azimuthal symmetry in free space, the radial functions would be integer powers of r, and the angular functions would be Legendre polynomials. However, we have here a problem not in free space but with a conical boundary, i.e. the solution is required to vanish at the angle $\theta = \alpha$ (cone angle). Thus, Legendre polynomials are generalized to *Legendre functions,* $P_{\nu_k}(\mu)$, where ν_k are real numbers but not integers. Whereas the degrees of the first few Legendre polynomial are 0, 1, 2, 3..., the degrees of the first few the Legendre functions always fall in the similar intervals – $0<\nu_0<1$, $1<\nu_1<2$, $2<\nu_2<3$ ..., (Correspondingly, the radial functions become non-integer powers of r.) Legendre functions are special functions that are defined by the same differential equation as Legendre polynomials and also form a complete, orthonormal basis. However, Legendre functions vanish for a certain value of $\mu = \cos(\theta)$ that is determined by the degree, ν_k, of the Legendre function. Using a special algorithm, detailed in Appendix A, the numbers ν_k are chosen to make the Legendre functions vanish for $\mu = \cos(\alpha)$. Thus, the solution for the potential is equal to zero on the surface of the cone. The remaining constants come about from orthogonality and normalization integral of Legendre functions.

The above solution works well in region 2 (except when the radius is near gate radius, in which case an asymptotically large number of terms is needed for an accurate solution. In practice, taking the first 15 or 30 terms, which is not difficult with Mathematica [10], gives an accurate solution in most of the region. The unavoidable spike at $r = r_G$ can be smoothed out and does not introduce a major error in trajectory

calculations.) However, the solution is inappropriate for region R1. The leading term of the radial electric field at small r goes as r^{ν_0-1}, which diverges at the origin. But R1 is the region we are most interested in; thus, the model needs a modification, which consists of adding a small sphere concentric with the cone tip. In **figure 3.2**, the radius of the sphere is $\mathbf{r_\varepsilon}$, which can be taken as the tip radius of curvature. Now, the equation for the potential throughout all space between $\mathbf{r_\varepsilon \le r \le r_G}$ is given by:

$$V(r<r_G,\theta)=\frac{Q_G}{4\pi\varepsilon_0 r_G}\sum_{k=0}^{\infty}\frac{P_{\nu_k}(\mu_1)}{\left(\nu_k+\frac{1}{2}\right)\int_{\mu_0}^{1}\left[P_{\nu_k}(\mu')\right]^2 d\mu'}*P_{\nu_k}(\mu)*\left(\left(\frac{r}{r_g}\right)^{\nu_k}-\frac{r_\varepsilon^{2\nu_k+1}}{r_g^{\nu_k}\,r^{\nu_k+1}}\right) \quad (3.3)$$

Equation 3.3 was obtained by observation. Notice that the radial part vanishes when r = $\mathbf{r_\varepsilon}$, making the potential equal to zero at the cone tip. The expression also satisfies Laplace's equation, since $\frac{1}{r^{\nu_k+1}}$ is also a solution of the radial part of Laplace's equation. Since the expression in (3.3) both satisfies Laplace's equation and meets the boundary conditions, it is the solution for the potential of a sphere plus a cone in R1 and R2. Gate charge, Q_G, can be replaced with a measurable parameter, which is gate voltage, via: $Q_G = C_G V_G$, where C_G is gate capacitance (unknown).

Before generalizing equation 1 to include the focus electrode, it is worthwhile to derive several important results related to intrinsic beam spread and the magnitude of field emission current from the single gate formula. While the following results are not confined to the one electrode case, the single electrode formula does provide a way to give a simple, analytical representation of the results as well as to compare the analytical results with the results of *numerical* simulations done by others.

3.4 Radial Field on the Tip as a Function of Angular Position and the Effect of the Cone Base Angle.

One of the main causes of intrinsic beam spreading is emission from the points adjacent to the apex. On a cone with a spherical tip, as well as in the present model, the radial electric field at the tip has a peak at zero angle from the vertical. If this peak is sharp, i.e. if the electric field decreases rapidly away with angle from the vertical, the fraction of the total current that's emitted away from the vertical will be small. Thus, making the electric field peak sharply at the apex is a way to reduce intrinsic beam spreading for emission from spherical tips.

On the surface of the tip, $r = r_\varepsilon << r_G$; thus, the first term dominates the electric field, obtained by taking the radial derivative of equation 3.3:

$$E_r(r_\varepsilon,\theta) = -\partial V/\partial r = -\frac{C_G V_G}{4\pi\varepsilon_0 r_G r_\varepsilon} A_0 P_{\nu_0}(\mu)(2\nu_0+1)\left(\frac{r_\varepsilon}{r_G}\right)^{\nu_0} \quad ; \qquad (3.4)$$

where A_0 represents the constant fraction term involving the integral in equation 3.3.

The rate of decrease of the radial electric field with cone angle is measured by the ratio of the radial field at angle θ from the apex to the radial field at the apex (i.e. at θ=0)

$$\frac{E_r(r_\varepsilon,\theta)}{E_r(r_\varepsilon,\theta=0)} = \frac{P_{\nu_0}(\mu)}{P_{\nu_0}(1)} = P_{\nu_0}(\mu) \approx 1 + \frac{\nu_0(\nu_0+1)}{2}(\mu-1) \approx 1 - \frac{\nu_0(\nu_0+1)}{4}\theta^2 \qquad (3.5)$$

approximation is good for $0 \le \theta \le 30°$

Now, the model makes it possible to bring out the effect of another structural parameter not mentioned up till now, namely the cone angle (base angle or, in this case, apex half-angle.).

This is possible because the degree of the Legendre function, ν_0 in eq. 3.4 and 3.5, is determined by the cone angle, α, as follows (for more detail, see Appendix A):

$$\begin{aligned} \nu_0 &\approx 0.975 + 0.731\cos(\alpha) \quad [for\ 95° < \alpha < 155°] \\ &\approx -15.91 - 35.76\cos(\alpha) - 19.7\cos^2(\alpha) \quad [for\ \alpha > 155]; \end{aligned} \tag{3.6}$$

$$\boxed{\frac{E_r(r_\varepsilon,\theta)}{E_r(r_\varepsilon,\theta=0)} \approx P_{\nu_0}(\mu) \approx 1 - \frac{(0.975+0.731\cos(\alpha))(1.975+0.731\cos(\alpha))}{4}\theta^2} \tag{3.7}$$

Figure 3.3 shows the plot of the electric field on the tip as a function of angle from the vertical. (The Legendre polynomial is plotted because the approximation is only valid for θ<30°.)

Note that according to equation 3.7, the only parameter which determines the drop-off of electric field with angle from the apex is the base angle of the cone. Thus, base angle (i.e. aspect ratio) of the cone is directly related to intrinsic beam spread. **The model predicts that cones with lower aspect ratio will have a smaller angular spread of the emitted current.**

Note also that the model predicts a much slower drop-off than a numerical calculation. This is due to an artifact in the analytical model. Since the model has almost a complete sphere at the cone tip, there is a larger angle from the apex (the position of the maximum field) to the point where the spherical tip meets the cone "sidewall" (which is the position of zero field). This leads to the prediction of slower drop-off. (In fact, it can be easily shown that the angle subtended by a spherical cap on a cone is 90° smaller than the angle subtended by the spherical tip in the present model.)

To compensate for this systematic error, the curve was calculated with the cone apex angle (apex angle = 90 - base angle) equal to twice the actual value. The result, showed by the dashed line in Figure 3.3, is in surprisingly good agreement with the numerical results, obtained by a completely independent method.

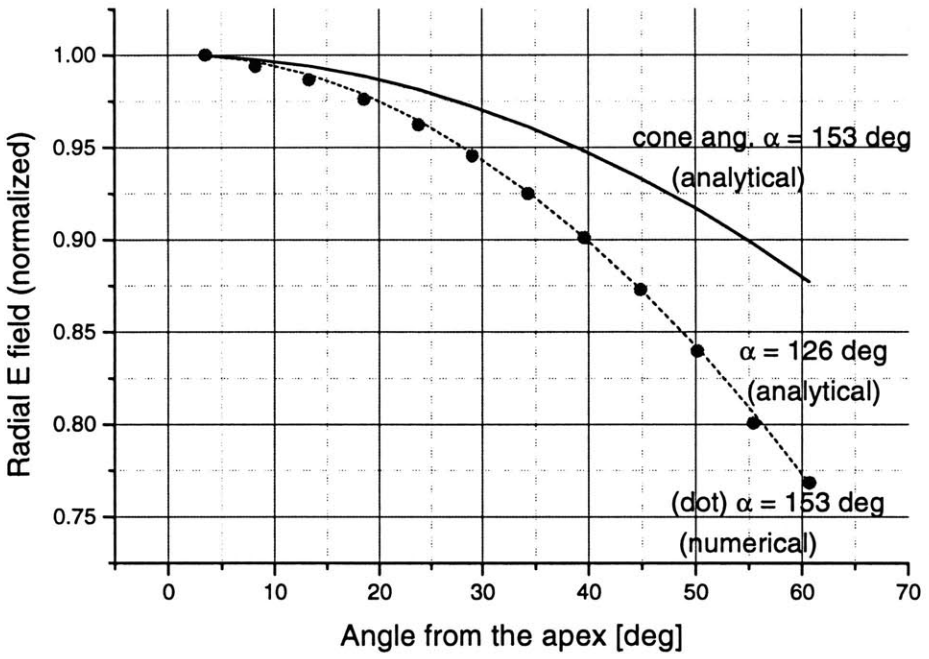

Figure 3.3. Radial Field on the Tip as a Function of Angle from the Vertical (Comparison of analytical and numerical [11] results.

3.5 Radial Field at the Apex

The magnitude of the radial electric field at the apex determines the magnitude of the field emission current, which is probably the most important evaluation criterion of FED performance. Increasing the field at the apex leads to lower operating voltage or greater emission current.

From equation 3.3 we can obtain the field at the apex:

$$E_r(r_\varepsilon,0) = -\frac{C_G V_G}{4\pi\varepsilon r_g r_\varepsilon} * \frac{P_{\nu_0}(\mu_1)}{\left(\nu_0+\frac{1}{2}\right)\int_{\mu_0}^{1}\left[P_{\nu_0}(\mu')\right]^2 d\mu'}(2\nu_0+1)\left(\frac{r_\varepsilon}{r_g}\right)^{\nu_0} \qquad (3.8)$$

(since $\frac{r_\varepsilon}{r_g} \approx 0.01 << 1$, only the first term of the summation in eq. (1) remains. Set $\nu_0=\nu$. Again the substitution $Q_G = C_G V_G$ has been made.) From Ref. [6],

$$\left(\nu+\frac{1}{2}\right)\int_{\mu_0}^{1}\left[P_\nu(\mu')\right]^2 d\mu' \approx 1-\frac{2\sin^2(\nu\pi)}{\pi^2}\Psi'(\nu+1)-(2\nu+1)\frac{\sin^2(\nu\pi)}{\pi^2}(1+\mu_0)+O\left((1+\mu_0)^2\right)$$

(The $O(1+\mu_0)$ term turns out to be negligible.)

If $\theta_g \approx 90°$, *i.e.* $\mu_1 \approx 0$, (the tip is in the plane of the gate opening), then [6]:

$$P_\nu(\mu_1) \approx \frac{\sqrt{\pi}}{\Gamma\left(\frac{1}{2}-\frac{\nu}{2}\right)\Gamma\left(1+\frac{\nu}{2}\right)}+\frac{\nu(\nu+1)\sqrt{\pi}}{2\,\Gamma\left(1-\frac{\nu}{2}\right)\Gamma\left(\frac{3}{2}+\frac{\nu}{2}\right)}\mu_1+O(\mu_1^2)$$

(but with Mathematica this approximation is unnecessary.)

Thus the radial field at the apex as a function of cone angle becomes:

$$E_r \approx \frac{C_G V_G}{4\pi\varepsilon_0 r_G r_\varepsilon} \times P_\nu(\mu) \times \left(1 - \frac{2\sin^2(\nu\pi)}{\pi^2}\Psi'(\nu+1)\right)^{-1} \times (2\nu+1)\left(\frac{r_\varepsilon}{r_G}\right)^\nu ; \qquad (3.9)$$

This formula brings out the exact analytical form of dependence of the apex field (and hence emission current) on gate radius, gate voltage, and emitter radius of curvature. Up till now these relationships have been discussed only qualitatively. The formula proves the intuitive result that **the apex field is proportional to gate voltage**.

The dependence of the apex field on the emitter radius of curvature is seen to be:

$$E \propto r_\varepsilon^{-1+\nu} \propto r_\varepsilon^{-0.025+0.731\cos(\alpha)} \qquad (3.10)$$

where the last approximation, is valid for cone apex half-angle of no less than 25° i.e. aspect ratio no greater than 1.07. (eq. 3.6) The formula also shows than **the apex field increases with aspect ratio.**

The plot of $\mathbf{E_r}$ **vs.** $\mathbf{r_\varepsilon}$ and comparison to the numerical simulation data [1] is shown in **figure 3.4**. The analytical solution, $E_r \propto r_\varepsilon^{-1+\nu} = r_\varepsilon^{-0.69}$ (for α=155°, the value used in [1]) shows excellent agreement with numerical results obtained by a completely different approach.

Next, we extract the dependence of the apex field on gate radius. Since the gate capacitance, C_G, should be proportional to the gate radius, one factor of r_G in equation (3.9) cancels out and we are left with:

$$E \propto r_G^{-\nu} \propto r_G^{-0.975-0.731\cos(\alpha)} \qquad (3.11)$$

Again, the last approximation is valid for cone apex half-angle of no less than 25° (i.e. aspect ratio no greater than 1.07) **The dependence of the apex field on gate radius further confirms that the apex field increases with aspect ratio.**

The plot of $\mathbf{E_r}$ **vs.** $\mathbf{r_G}$ and comparison to the numerical simulation data [1] is shown in **figure 3.5**. Again, the analytical solution, $E_r \propto r_g^{-\nu} = r_g^{-0.31}$ shows excellent agreement with the numerical data.

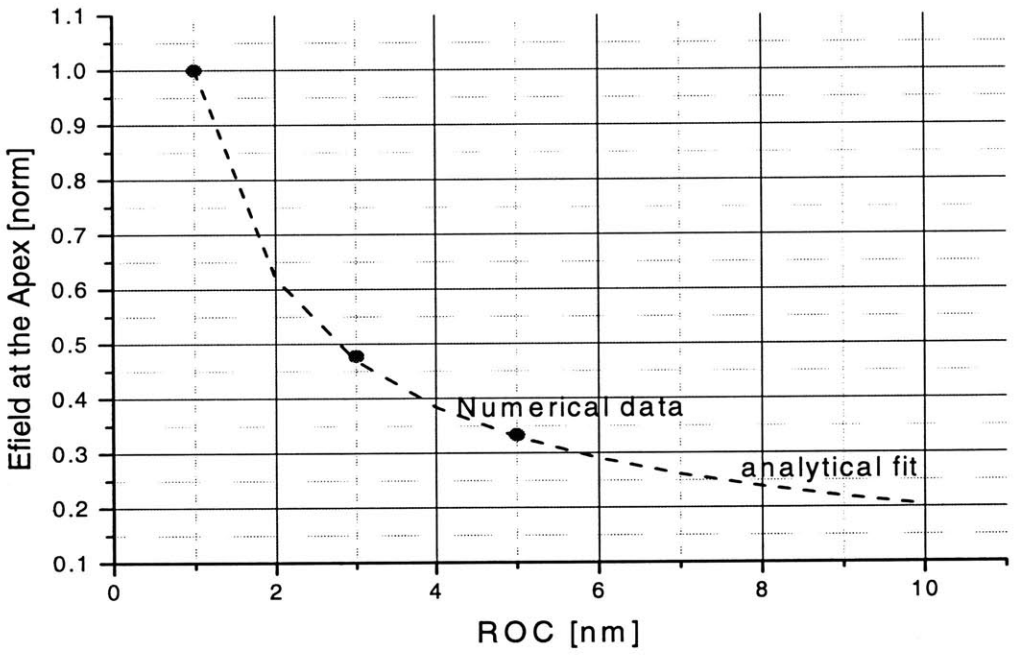

Figure 3.4. Radial Field at the Apex as a Function of the Tip Radius of Curvature (Comparison of Analytical and Numerical [1] Results.

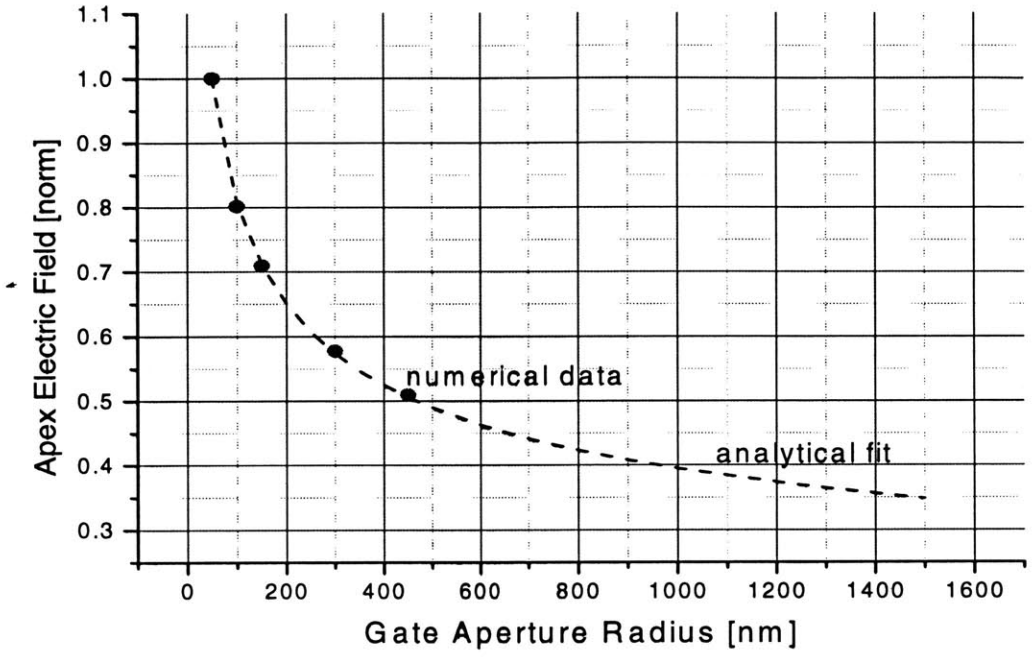

Figure 3.5. Radial Field at the Apex as a Function of the Gate Aperture Radius (Comparison of Analytical and Numerical [1] Results.

In the preceding analysis we have observed twice that the apex field increases with cone aspect ratio. Now we specifically focus our attention on the form of this dependence. Equation (3.9) shows that parameter ν, and hence cone angle, enters the expression for the apex field in several complicated functions. Results plotted on figure 3.6 were obtained by substituting the expression for ν as a function of cone angle into equation (3.9) and computing the resulting values in Mathematica.

The plot of the electric field at the apex vs. cone angle (figure 3.6) shows qualitative agreement between analytical and numerical [1] solutions, however the analytical model predicts a much stronger dependence than that shown in the numerical simulation. The discrepancy is probably due to the artifact in the analytic model, whereby

the tip is modeled as an almost full sphere rather than a more realistic spherical cap (as used in the numerical model). As mentioned above, the spherical cap subtends an angle from the vertical that is smaller by 90° than the angle subtended by the sphere in the present model.

However, in this case, we could not successfully compensate for this artifact, as was done for the data in Fig. 3.4

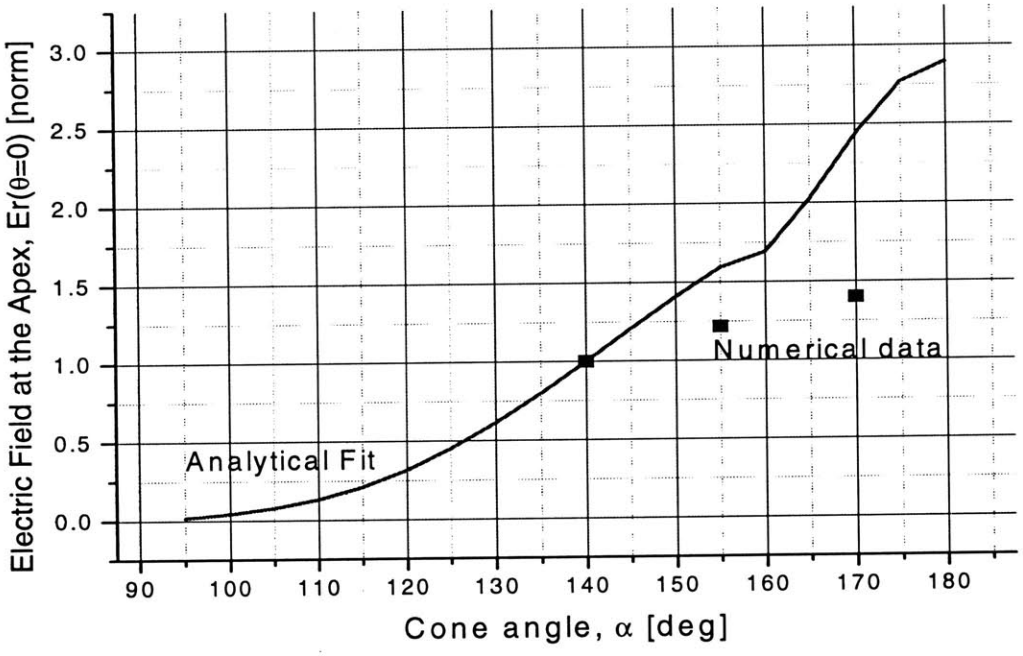

Figure 3.6. Electric Field at the Apex (E_r) vs. Cone Angle (α). (Comparison of analytical and numerical results.)

3.6 Analytical Model for the Double Gate FED

Generalization of the model to incorporate the focus electrode is straightforward. Following the same arguments as those in the beginning of this chapter, we represent the focus electrode by another charged ring (fig. 3.7), whose position is defined in spherical coordinates by two parameters: distance from the origin, r_F, and angle from the vertical. The preceding are two mathematically convenient parameters; however, the more intuitive parameters are vertical distance from the gate, h_{GF} and radius of the ring, R_F. By superposition we obtain the equivalent of equation (3.1) for the double gate model: (3.12)

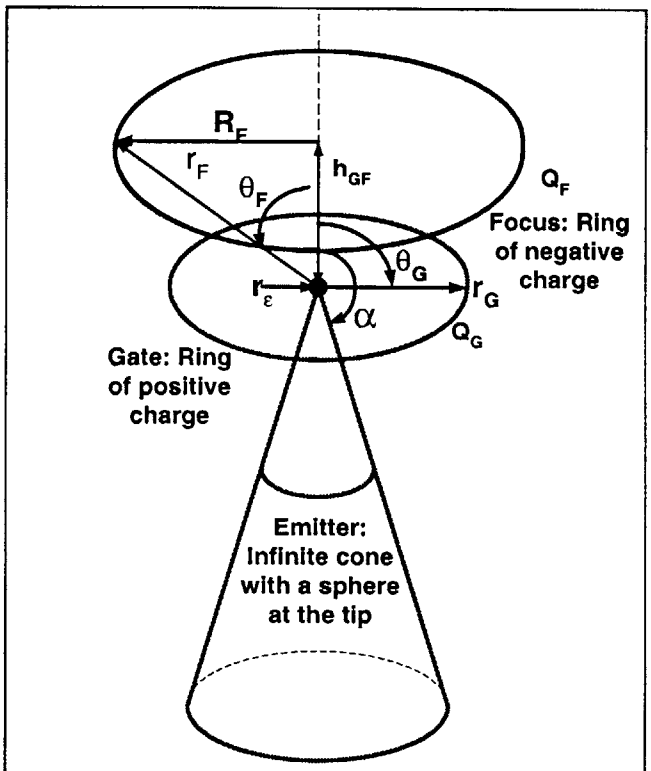

Figure 3.7. Double Gate Analytical Model.

$$V(r<r_G,\theta)=\frac{Q_G}{4\pi\varepsilon_0 r_G}\sum_{k=0}^{\infty}\frac{P_{\nu_k}(\mu_1)}{\left(\nu_k+\frac{1}{2}\right)\int_{\mu_0}^{1}\left[P_{\nu_k}(\mu')\right]^2 d\mu'}*P_{\nu_k}(\mu)*\left(\left(\frac{r}{r_G}\right)^{\nu_k}-\frac{r_\varepsilon^{2\nu_k+1}}{r_G^{\nu_k}\,r^{\nu_k+1}}\right)$$

$$+\frac{Q_F}{4\pi\varepsilon_0 r_F}\sum_{k=0}^{\infty}\frac{P_{\nu_k}(\mu_2)}{\left(\nu_k+\frac{1}{2}\right)\int_{\mu_0}^{1}\left[P_{\nu_k}(\mu')\right]^2 d\mu'}*P_{\nu_k}(\mu)*\left(\left(\frac{r}{r_F}\right)^{\nu_k}-\frac{r_\varepsilon^{2\nu_k+1}}{r_F^{\nu_k}\,r^{\nu_k+1}}\right)$$

$$\mu_2 = \cos(\theta_F)$$

All the other parameters in eq. 3.11 are defined the same as in eq. 3.1.

Again, there is a way to write the charges, Q_G and Q_F, in terms measurable parameters – gate and focus voltages.

$$\boxed{\begin{aligned} Q_G &= C_G V_G + C_{GF} V_F \\ Q_F &= C_F V_F + C_{GF} V_G \end{aligned}} \tag{3.13}$$

The coefficients in eq. 3.12 are mathematical quantities that may be different from capacitances between pairs of conductors.

Equation (3.11) is too complicated to extract simple and illuminating analytical results. However, all of the insights we gained from a single gate model are still qualitatively true in the double gate case. One important use of the double gate model is to serve as a basis of numerical trajectory calculations. Hence, after a brief discussion of the effect of focus electrode on emission current, we will turn to that subject.

3.7 Radial Field at the Apex in a Double Gate Analytical Model

The double gate equivalent of equation (3.8) is (3.14)

$$\boxed{E_r(r_\varepsilon,0) = -\frac{1}{4\pi\varepsilon r_\varepsilon} * \frac{(2v_0+1)}{\left(v_0+\frac{1}{2}\right)\int_{\mu_0}^{1}\left[P_{v_0}(\mu')\right]^2 d\mu'} * \left[\frac{Q_G}{r_G}\left(\frac{r_\varepsilon}{r_G}\right)^{v_0} P_{v_0}(\mu_1) + \frac{Q_F}{r_F}\left(\frac{r_\varepsilon}{r_F}\right)^{v_0} P_{v_0}(\mu_2)\right]}$$

Since the focus charge, Q_F, is negative, it will reduce the field at the apex leading to the decrease in emission current. This effect has an obvious power law dependence

(identical to the dependence of the gate-induced field on the gate radius) on tip-to-focus distance given by:

$r_F = \sqrt{R_F^2 + h_{GF}^2}$.

The effect of the angular position of the focus electrode contained in the factor $P_{\nu_0}(\mu_2)$ is expected to be of secondary importance because, as shown on figure 3.8, the Legendre function varies rather slowly.

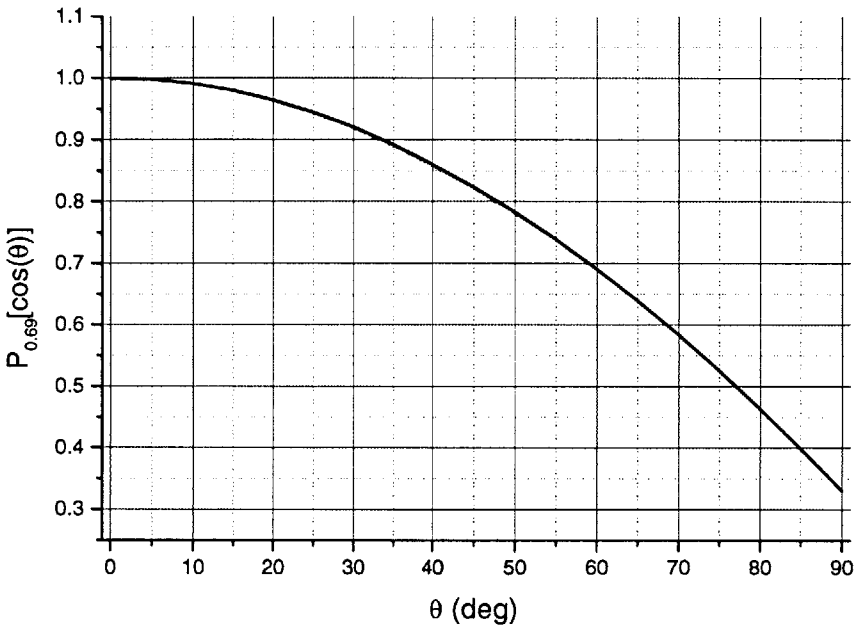

Figure 3.8. Variation of the Legendre function $P_{0.69}$ [cos(θ)] with θ.

In the analysis of field emission data, electric field on the tip is often written in terms of gate voltage as $E = \beta V_G$. It is useful to explore an equivalent formulation for a double gated device. With the help of eqtn (3.12), eqtn (3.13) can be recast in that form:

$$E_r(r_\varepsilon,0) = -\frac{1}{4\pi\varepsilon r_\varepsilon} * \frac{(2\nu_0+1)}{\left(\nu_0+\frac{1}{2}\right)\int_{\mu_0}^{1}\left[P_{\nu_0}(\mu')\right]^2 d\mu'} * \left[C_G \frac{1}{r_G}\left(\frac{r_\varepsilon}{r_G}\right)^{\nu_0} P_{\nu_0}(\mu_1) + \frac{C_{GF}}{r_F}\left(\frac{r_\varepsilon}{r_F}\right)^{\nu_0} P_{\nu_0}(\mu_2)\right] V_G$$
$$-\frac{1}{4\pi\varepsilon r_\varepsilon} * \frac{(2\nu_0+1)}{\left(\nu_0+\frac{1}{2}\right)\int_{\mu_0}^{1}\left[P_{\nu_0}(\mu')\right]^2 d\mu'} * \left[C_{GF} \frac{1}{r_G}\left(\frac{r_\varepsilon}{r_G}\right)^{\nu_0} P_{\nu_0}(\mu_1) + \frac{C_F}{r_F}\left(\frac{r_\varepsilon}{r_F}\right)^{\nu_0} P_{\nu_0}(\mu_2)\right] V_F$$
$$= \beta_G V_G + \beta_F V_F$$

(3.15)

3.8 Trajectory Calculations

The focus electrode collimates the electron beam by reducing the x-velocity of the electrons. This is achieved by the x-directional electric field of the focus electrode. In the meantime, electrons are accelerated towards the anode by the y-directional field. These are given by:

$$E_x = \frac{\partial V}{\partial r}\sin(\theta) + \frac{\partial V}{r\partial\theta}\cos(\theta);$$
$$E_y = \frac{\partial V}{\partial r}\cos(\theta) - \frac{\partial V}{r\partial\theta}\cos(\theta) - \frac{V_A}{h_A}; \quad ; \qquad (3.16)$$

(here V_A is anode voltage and h_A is cathode-anode separation.)

Angular derivatives of the terms involving Legendre functions can be expressed in terms of recursion relations, found in the tables of special function. In the actual computation,

all these derivatives are analytically taken in Mathematica, which is then instructed to integrate the coupled equations of motion:

$$x'' = -eE_x / m$$
$$y'' = -eE_y / m$$

Initial position on the emitter tip and initial velocity are given.

As we stated, equation (3.12) is valid when $r < r_G$. When $r > r_G$, the radial dependence changes to $\left(\frac{r_G}{r}\right)^{\nu_k}$. Thus, we obtain the following formula (given for a single electrode for clarity): (3.17)

$$V(r > r_G, \theta) = \frac{Q_G}{4\pi\varepsilon_0 r_G} \sum_{k=0}^{\infty} \frac{P_{\nu_k}(\mu_1)}{\left(\nu_k + \frac{1}{2}\right) \int_{\mu_0}^{1} \left[P_{\nu_k}(\mu')\right]^2 d\mu'} * P_{\nu_k}(\mu) * \left(\frac{r_g}{r}\right)^{\nu_k}$$

(Note that equations (3.12) and (3.17) not give the same answer for $\mathbf{r = r_G}$. However, if $\mathbf{r_\varepsilon << r_G}$, the difference is insignificant.)

Thus, a complete calculation of electron trajectories required calculation of the field according to three different formulas, corresponding to the three different regions – Region I: $r_\varepsilon < r < r_G$; Region II: $r_G < r < r_F$; Region III: $r > r_F$.

One of the main purposes of the present model was to verify the feasibility of focusing with the double gate structure. Figure 3.9a-d illustrates this. The figure shows the

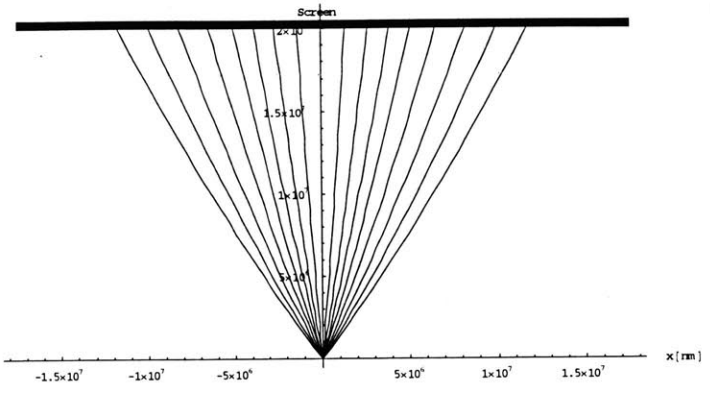

Figure 3.9a VG=100 V; No focus (x:y aspect ratio is 1:1)

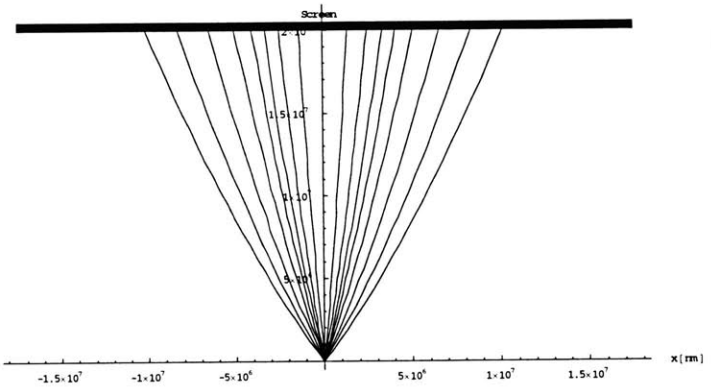

Figure 3.9b VG=100 V; VF = 40 V.

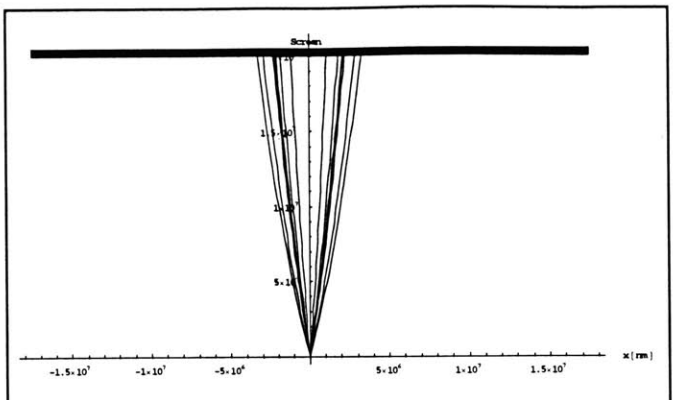

Figure 3.9c VG=100; VF=30;

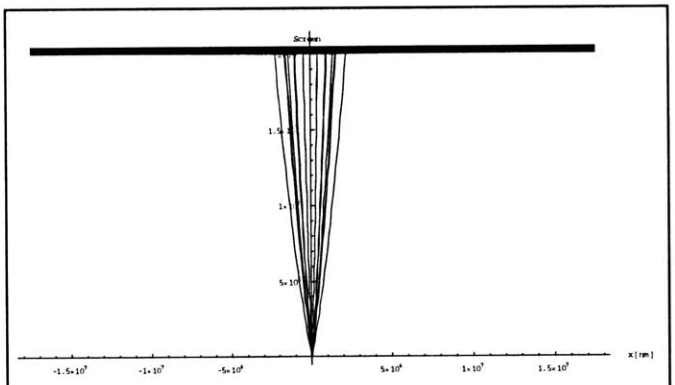

Figure 3.9d VG=100V; VF=28V;

trajectories computed under the following focusing conditions. Trajectories were launched at angles 5-40°, in 5° increments. (The left side of the plots, corresponding to emission angles of -5° to -40°, was obtained by reflecting the trajectories in the first quadrant around the vertical axis.) Gate and focus radii were 700 and 900 nm respectively, and the vertical separation between the two electrodes was 600 nm. Cone angle was 126°. Emitter tip radius was 10 nm, with the metal work function set at 3.5 eV (this was used for calculating the emission current.) Gate voltage was kept constant at 100 V. In Fig. 5.9a, the charge on the focus ring was set to zero, thus effectively turning the device into a single gate structure. Then, in figures 5.9b-d, the focusing voltage was systematically lowered, making the charge on the focus ring increasingly negative. The minimum possible focusing voltage is one at the which the charge on the focus ring is so negative that its repulsive field begins to turn back the electron trajectories, i.e. electrons cannot reach the anode.

3.9 Variation of the Total Emission Current with Focusing Voltage

As focusing voltage is decreased, and the beam becomes more collimated, the total emission current is also reduced. Emission current density for a given electric field can be computed from the Fowler-Nordheim equation:

$$J = \frac{AE^2}{\phi t^2(y)} \exp\left[-B\frac{\phi^{3/2}}{E} v(y)\right] Amp/cm^2 \qquad (3.18)$$

where E is the electric field on the surface, in V/cm; J is the emitted current density; ϕ is the work function in eV,

$A = 1.54 \times 10^{-6}$,

$B = 6.87 \times 10^{7}$,

$y = 3.79 \times 10^{-4} \dfrac{E^{1/2}}{\phi}$,

$t^2(y) = 1.1$,

$v(y) = 0.95 - y^2$.

The total current emitted from the tip is given by the integral of the current density:

$$I_{Tot} = \int_0^{40} J\left[E(r_\varepsilon, \theta)\right] \left(2\pi r_\varepsilon \sin(\theta)\right) r_\varepsilon \, d\theta \qquad (3.19)$$

The upper limit of integration is taken to be 40° to be consistent with the limits on the trajectory calculations and also because in a real cone the tip ends at approx. that angle. The preceding integral is evaluated numerically in Mathematica and shows that emission current is greatly affected by the focusing electrode, as summarized in Table 3.1.

Table 3.1 Variation of the emission current with focusing voltage.

V_G [V]	V_F [V]	const x Q_G [ ]	const x Q_F [ ]	E_{Apex} [V/cm]	I_{TOT} [nA]
100	--	174	0	-2.21 x 10^7	4.68
100	40	192	-29	-2.02 x 10^7	0.58
100	30	201	-44	-1.92 x 10^7	0.167
100	28	203	-47	-1.90 x 10^7	0.128

3.10 Implications of the Analytical Model on Device Design and Specifications of Structural Parameters

The analytical model has provided a number of clear insights into device operation and desirable device geometry, as well as into possible design problems and trade-offs.

The model has clearly shown that while focusing can overcome the problem of trade-off of luminous efficiency for display resolution, it can also introduce a new trade-off of its own. The principal trade-off in IFE FEA's arises because the focus electrode, in addition to collimating the electron beam, also reduces the electric field at the tip, thus decreasing field emission. Thus, a better collimated beam, and the resulting smaller spot size, is achieved at the cost of smaller emission current, which leads to reduced brightness. One way to overcome this new trade-off of brightness vs. resolution is to adjust the focus voltage to collimate the beam and then raise the gate voltage, which would make up for the drop in emission current. With this approach, a collimated beam is achieved at the cost of higher operating voltage.

Design of a IFE FEA involves specifying a number of structural parameters – gate and focus radii, vertical gate-to-focus distance, thicknesses of the gate and focus electrodes, and cone aspect ratio (i.e. cone apex angle or base angle – specified to some extent through the thickness of the gate-to-cathode isolator.) First, based on the predictions of the analytical model, we decided to minimize the gate radius in order to maximize emission current, or, equivalently, minimize the operating voltage. We aimed at the gate radius of 0.5 μm – the minimum aperture size achievable with our lithography

tools. Next, we opted to minimize vertical gate-to-focus distance, choosing more effective focusing at the cost of reduced emission (or higher operating voltage). We estimated that in order for the gate-to-focus insulator to be able to sustain the voltage difference between the two electrodes, it has to be at least 0.5 μm thick, and we designed the device with this minimal possible gate-to-focus distance. A similar choice was made with respect to the radius of the focus electrode, where we bypassed the option of making it much larger than the gate radius. This would have allowed the gate to partially shield the tip from the effect of the focus and thus avoid current suppression, but at the cost of reduced focusing efficiency. Here, we again opted for the best possible focusing and designed the focus radius to be just slightly larger than the gate radius. The reasoning behind seeking the most effective focusing possible is that this was our *first* investigation of IFE FEA. When we had determined what is the best possible focusing we can achieve, i.e. what is the smallest pixel size we can achieve, we would be able to weigh the benefits of giving up some focusing efficiency in a trade-off for better performance in other areas.

Thickness of the gate and focus electrodes was to be kept to the minimum, about 0.2 μm. One reason for this is that with slanting sidewalls of the gate and focus, the excess charge will likely concentrate of the innermost rims, both on the gate and on the focus, because that is the place of the strongest electric fields (due to electrostatic interaction with the cathode and between gate and focus.) Thus, electrode thickness was not expected to affect the operation much (independent numerical modeling also indicated so), and thinner electrodes were simpler to fabricate.

We did not experiment with cone aspect ratio, aiming to make cones with the aspect ratio of one. However, as suggested by the model, this parameter also holds a

trade-off (though, probably, of secondary importance). Cones with a *higher* aspect ratio have higher fields at the tip, and hence higher emission current. But at the same time, a different argument suggests that higher aspect ratio leads to greater intrinsic beam spreading, which in turn could impair display resolution. Lowering the aspect ratio is expected to reduce the intrinsic beam spread, but at the cost of lowering emission current somewhat.

Appendix. **Computing non-integral degrees, ν_k, of Legendre Functions.**

If Laplace's equation is separated in spherical coordinates, the general solution is [12]:

$$V(r,\theta,\phi)=\sum_{l=0}^{\infty}\sum_{m=-l}^{l}\left[A_{lm}r^{l}+B_{lm}r^{-(l+1)}\right]Y_{lm}(\theta,\phi);$$

Here, Y_{lm} are the spherical harmonics. For azimuthal symmetry (independent of ϕ), m=0, and spherical harmonics become Legendre polynomials, $P_l(\cos[\theta])$. If the solution is required to vanish for some fixed value of θ (i.e. we have a conical boundary condition: $\theta = \alpha$ -- cone angle), the order of the Legendre polynomial, l, becomes a non-integer, usually called ν_k, (and so does the power of r), and Legendre polynomials generalize to Legendre functions, which are well known and tabulated special functions. Computing the orders of the Legendre functions, ν_k, for a given cone angle was accomplished in three steps in the present work:

***Step I*:** Get the first estimate, $\nu_k^{(1)}$ using the analytical formula given in [8]:

$$\nu_k^{(1)}(\theta)=z_k+\frac{u\left(\frac{1}{2z_k}-1-\frac{u}{24(2z_k)^3}-\frac{4u^2}{3(8z_k)^3}\right)}{4\theta}-\frac{u^2\left(1+\frac{1}{2{z_k}^2}\right)}{64\,\theta^2\,{z_k}^3};$$

where,

θ is the cone angle (in radians) (called α on Figure 3.1.)

$$z_k=\frac{\pi}{2\theta}\left(2k+\frac{3}{2}-\frac{\theta}{\pi}\right);$$

$$u=\cot(\theta);$$

Step II.

Estimate the error introduced by the formula in Step I to calculate $\nu_k^{(1)}$ at the known zeros, $\theta = \theta_0$, of Legendre polynomials and Legendre functions of half-integral degree. (The table of these values of θ is given in [6]). The real answer is the integer or half-integer, l_k, so the error introduced by the formula in Step I is then given by: $\varepsilon(\theta) = \nu_k^{(1)} - l_k$. Note that epsilon depends only on the angle; it's dependence on the index, k, is not included. Interpolation yield a continuous function, ε(θ). Then the second estimate is given by:

$$\nu_k^{(2)}(\theta) = \nu_k^{(1)}(\theta) - \varepsilon(\theta)$$

Step III.

Using the numerical solver in Mathematica solve the equation

$$P_{\nu k}\left(\theta = cone\ angle\right) = 0;$$

for the values ν_k . The two starting points required by the numerical algorithm are supplied by $\nu_k^{(1)}$ *and* $\nu_k^{(2)}$.

The Mathematica implementation of the above steps is given at the end of this Appendix.

The most important and useful value for near-the-tip calculations is ν_0 . The linear and parabolic expression for ν_0 , given in the main text, where obtained by fitting a range of calculated values of ν_0 as a function of the angle θ. The plot of the data, **ν_0 vs. cos(θ)**, as well as the fits is shown below:

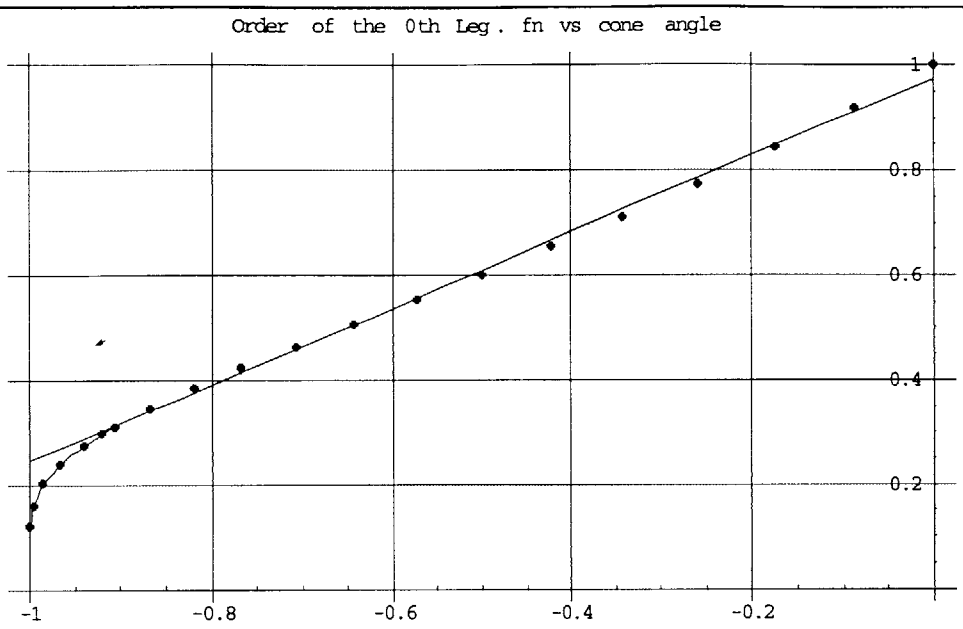

Figure 3.A.1 Order of the Legendre function vs. cosine of the cone angle.

Printout of the Mathematica Routine.

```
(* Step I *)
Print["Compute the first ten values Nu_k for 160 deg cone angle."];

ang = 160;
ph = ang 3.141592654 / 180;
num = 10;
x = Cos[ph]; k = Table[i, {i, num}];
u = Cot[ph];

z = (3.14159 (2 k + 3/2 - ph/3.14159)) / (2 ph);

n = z + (u (1/(2 z) - 1 - u/(24 (2 z)^3) - 4 u^3/(3 (8 z)^3))) / (4 ph) - (u^2 (1 + 1/(2 z^2))) / (64 ph^2 z^3);

Print["First Approximation:"];
Print[Prepend[n, n[[1]] - 1]];
(* ------------------------------------------------------------- *)


(* Step II *)

(* The next three commands obtain the error function, epsilon.*)
(* The data is in the form ( cos[ph], error ); the values were computed separately*)

eps = Sort[{{-.973907, .366292}, {-.865063, .164252},
   {-.978229, .399894}, {-.887063, .17997}, {-.96816, .332578}, {-.96029, .29869},
   {-.949108, .264565}, {-.93247, .230069}, {-.90618, .19497}, {-.981561, .433407},
   {-.904117, .195447}, {-.984183, .466858}, {-.917598, .210735}, {-.986284, .500248}, {-.928435, .225874}}];
eps2 = Append[eps, {0, 0}];
epsint = Interpolation[eps2];

(* "neps" is the second approximation *)
neps = n - epsint[x];
Print[ "Second approximation:"];
Print[Prepend[neps, neps[[1]] - 1] ];
(*-------------------------------------------------------------*)


(* Step III. *)

nfin = Table[FindRoot[LegendreP[ord, x] == 0, {ord, {n[[i]], neps[[i]]}}], {i, num}];

(* The first root, Nu_0 is a special case. *)
root0 = FindRoot[LegendreP[ord, x] == 0, {ord, {n[[1]] - 1, neps[[1]] - 1}}];

(* ------------------------------------------------------------*)


(* The following prints the data. *)

nfin = Prepend[nfin, root0];
Print["Computed degree values:"];
Print[ord /. nfin];

zeros = LegendreP[ord /. nfin, x];
Print["Values at angle pheta (i.e. on the cone)"];
Print[zeros];
```

```
Compute the first ten values Nu_k for 160 deg cone angle.
First Approximation:
{0.625517, 1.62552, 2.79144, 3.93136, 5.0642, 6.19404, 7.32233, 8.44972, 9.57653, 10.7029, 11.8291}
Second approximation:
{0.383517, 1.38352, 2.54944, 3.68936, 4.8222, 5.95204, 7.08033, 8.20772, 9.33453, 10.4609, 11.5871}
Computed degree values:
{0.274502, 1.42475, 2.56153, 3.69342, 4.82293, 5.95111, 7.07847, 8.20528, 9.33172, 10.4579, 11.5838}
```

Values at angle pheta (i.e. on the cone)

$\{1.35544\times10^{-7}, -1.12484\times10^{-8}, 7.8804\times10^{-11}, 3.25828\times10^{-7}, -7.8913\times10^{-9}, 9.63576\times10^{-9}, -3.11076\times10^{-8}, 4.36964\times10^{-8}, -4.8831\times10^{-8}, 4.97293\times10^{-8}, -4.84779\times10^{-8}\}$

Appendix 2. A simpler method for Computing Non-Integral Degrees of Legendre Functions.

A look at the "Computed degree values" listed above suggests an alternative way to compute the necessary degrees of Legendre functions. This way does not provide any analytical solutions, but it is simpler and more general (since the error estimates used in step II of the first method are only valid for a limit range of θ_0) if one has access to the necessary computing environment (such as Mathematica). As indicated in step III of the method described in Appendix 1, Mathematica can numerically solve an equation of the form:

$$P_{\nu_k}\left(\cos[\theta_0]\right) = 0$$

for the values of non-integral degrees, $\nu_k(\theta_0)$, $k = 0, 1, 2 \ldots$ The difficulty is that the numerical algorithm finds the root that is closest to the first two trial values provided by the user; thus, to insure that the numerical solver does not miss any solutions, one needs to have two fairly accurate estimates for each root. In the first method, Steps I and II served to provide these estimates. In the present method, these estimates are derived from the following three observations:

1. $0 \le \nu_0 \le 1$
2. $1 \le \nu_1 \le 2$
3. $\nu_{n+1} = \nu_n + x, \quad (1 \le x \le 2)$

The above conditions appear to hold for all Legnedre functions. (In the special case of Legendre *polynomials*, we have: $\nu_0 = 0;\ \nu_1 = 1;\ \ x = 1$.) The following Mathematica routine demonstrates the application of this method for θ_0=126°.

```
(* DEFINE THE VALUE FOR THE CONE ANGLE, 'PH' *)
ph = 126 3.141592654 / 180;
num = 15;
x = Cos[ph];

(* FIND THE FIRST TWO ROOTS, TAKING 0.5,0.6 AND
   1.5, 1.6 AS THE STARTING VALUES *)
nfin = Table[FindRoot[LegendreP[ord, x] == 0, {ord, {i - 0.5, i - 0.4}}], {i, 2}];

(* 'TRY1' IS A GUESS AT THE THIRD ROOT *)
try1 = 2 * (ord /. nfin[[2]]) - (ord /. nfin[[1]]);

preval = nfin[[2]];

(* COMPUTE THE NEXT THIRTEEN (OR 'NUM') ROOTS *)
For[ i = 3, i <= 15, i++,
   value = FindRoot[ LegendreP[ord, x] == 0, { ord, {try1, try1 - 0.1} }];
   try1 = 2 * (ord /. value) - (ord /. preval);
   preval = value;
   nfin = Append[nfin, value];
];
(* WRITE THE COMPUTED VALUES TO FILE NAMED 'DEGREES' *)
nfin >> "degrees";

(* PRINT COMPUTED DEGREE VALUES *)
Print["Computed degree values:"];
Print[ord /. nfin];
```

```
(* PLOT THE FIRST THREE LEGENDRE FUNCTIONS *)
Plot[{LegendreP[ord /. nfin[[1]], z], LegendreP[ord /. nfin[[2]], z], LegendreP[ord /. nfin[[3]], z]},
 {z, -.99, .99}, Frame → True, GridLines → Automatic, PlotLabel → "1st 3 Legendre functions of orders nk",
 AxesLabel -> {"Cos[ph]", ""}];

(* MAKE SURE THAT THE LEGENDRE FUNCTIONS OF THE CALCULATED DEGREES
  INDEED VANISH ON THE CONE *)
zeros = LegendreP[ord /. nfin, x];
Print["Values at angle pheta (i.e. on the cone)"];
Print[zeros];
```

{0.542838, 1.98494, 3.41851, 4.84963, 6.27973, 7.70931, 9.13861, 10.5677,
 11.9967, 13.4256, 14.8545, 16.2833, 17.712, 19.1408, 20.5695}

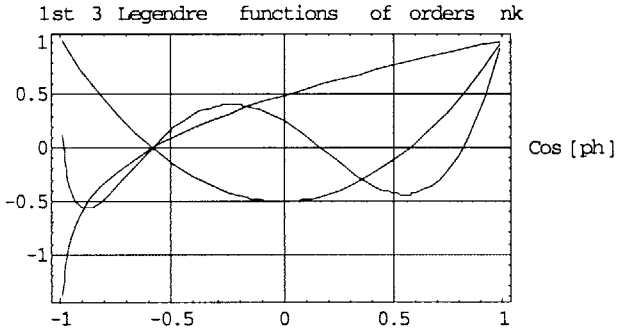

Values at angle pheta (i.e. on the cone)
{9.73515×10^{-10}, 3.54495×10^{-9}, 2.7851×10^{-8}, -6.23518×10^{-10}, 4.03798×10^{-7},
 -6.55281×10^{-7}, 5.17347×10^{-7}, -3.75434×10^{-7}, 2.70381×10^{-7}, -1.9728×10^{-7},
 1.46594×10^{-7}, -1.10993×10^{-7}, 8.55425×10^{-8}, -6.70077×10^{-8}, 5.32668×10^{-8}}

References for Chapter 3.

1. D. Pflug, MS Thesis, MIT, 1996
2. W. Dawson Kesling, Ph. D. Dissertation, UC Davis, 1995
3. W.B. Herrmannsfeldt et al., Nucl. Instr and Methods in Phys. Res., A298, 39-44, 1990
4. K.L. Jensen et al., J. Vac. Sci. Technol., B 14, 1947. 1996
5. K.L. Jensen et al., J. Vac. Sci. Technol. B 14(3), May/Jun 1996
6. Hall, J. of Appl. Physics, Vol. 20, October, 1949
7. W.P. Dyke et al., J. of Appl. Phys., Vol. 24, Num 5, May 1953
8. Hobson, The Theory of Spherical and Ellipsoidal Harmonics; Chelsea Publ. Co 1955
9. Smythe, Static and Dynamic Electricity; McGraw-Hill 1968
10. Mathematica 3.0, Student Version, by Wolfram Research
11. Joseph Young, Graduate Student in EECS, MIT, unpublished
12. Jackson, Classical Electrodynamics, 2nd Ed., Wiley 1975

CHAPTER 4

FABRICATION OF IFE FEA'S

A stacked, double-gated Spindt cone FED is fabricated. The gates are made of n^+ polysilicon and isolated from each other and from the cathode by layers of silicon dioxide. Since the oxide isolation layers were very thin (0.5-1 μm) and are required to withstand 50-100 V potential drops during normal device operation, it is necessary to obtain quality oxides with high dielectric strength. This factor is closely related to reliable operation and device lifetime. This is part of the rationale for using polysilicon rather than metal as the gate material. The best oxide (other than thermal) that can be deposited in our lab, is Low Temperature Oxide (LTO), deposited in a low-pressure chemical vapor deposition furnace. LTO can be densified and thus acquire properties close to those of the thermal oxide. Wafers with metal cannot go into the furnace for reasons of contamination. Thus, polysilicon gate is necessary. In addition, fairly resistive gates would provide feedback during device operation and contribute to device stability.

The process begins with 4 inch n-doped silicon wafers. First, one micron of thermal oxide is grown in an oxidation tube at around 1100 °C in H_20 ambient. Next, a thin layer (2500 Å) of polysilicon for the gate electrode is deposited by low-pressure chemical vapor deposition (LPCVD) and is then doped with phosphorous from a gaseous source. After a brief BOE (buffered oxide etch) dip to strip the thin layer of oxide grown during doping, the wafers went through chemical-mechanical polishing (CMP). The CMP step, described in more detail in Appendix B of this chapter, was added during the second run to eliminate polysilicon bumps which cause dents on the bottom of the second

a. A stack of poly/oxide/poly/oxide layers on the Si substrate

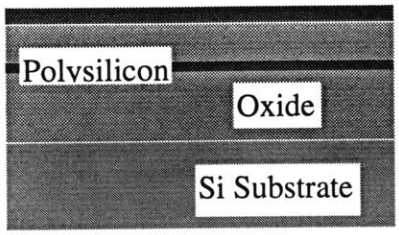

b. Patterning the gate contact (Mask 1)

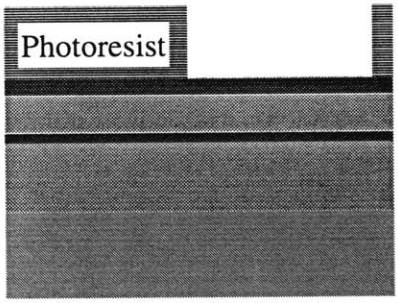

c. Etch to open the gate contact.

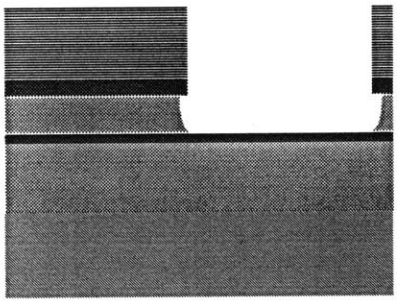

d. Patterning emitter openings (Mask 2)

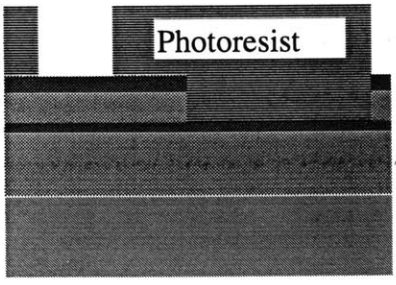

e. Dry etch of the emitter openings; followed by BOE dip and PR strip

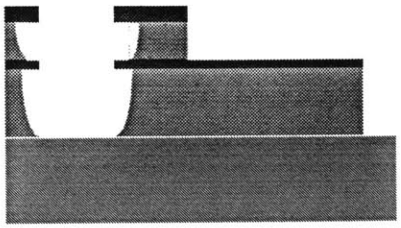

f. Angular evaporation of Al parting layer

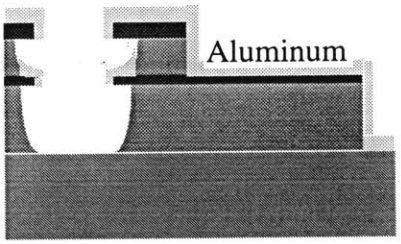

g. Evaporation of metal cone.

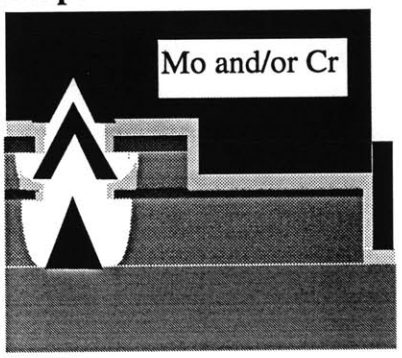

h. Finished FED after the lift-off

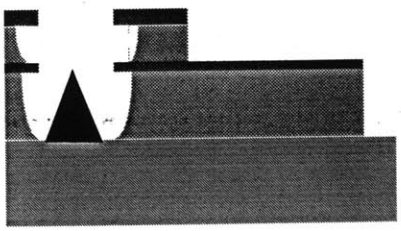

Figure 4.1 Process flow diagram

layer of polysilicon (as can be seen on fig. 4.2) and could also contribute to oxide breakdown. Following the CMP and subsequent cleaning, the wafers were taken back to the thermal oxidation tube. A very thin (~200 Å) layer of thermal oxide was grown on top of the gate poly in order to increase dielectric strength of the gate-to-focus isolation. After the thin layer of thermal oxide, about 0.5 microns of low-temperature oxide (LTO) was deposited (at 625 °C) and then densified. SEM examination of the oxide surface revealed roughness which was, however, much less than the roughness of polysilicon layers. Thus, we decided not to do CMP on the oxide layer. Polysilicon for the focus electrode was deposited, doped, and polished in the same steps as the gate electrode. The structure after this step is shown in the process diagram, figure 4.1a.

Next came the first of the two masking steps, intended to open gate contact. (We placed this step before etching the emitter openings to avoid having photoresist in the emitter openings.) Wafers were coated with HMDS (an adhesion promoter for the photoresist) and then with photoresist (standard thickness – 11,000 Å). Photoresist was baked, exposed with Mask 1, and developed (figure 4.1b.) Polysilicon was etched in an RIE (reactive ion etch) plasma etcher. Then, the LTO layer was removed in BOE. (fig. 4.1c) (In retrospect, it would have been safer to leave the LTO on top of the gate pads until after the second etch for extra protection of the thin gate layer.) Focus layer and gate-to-focus oxide were removed not only over the gate pads, but also over the gate leads to reduce gate-to-focus capacitance.

Next, after stripping the old photoresist, the wafers were again covered with photoresist and exposed with Mask 2, which defined 1 micron diameter emitter openings.

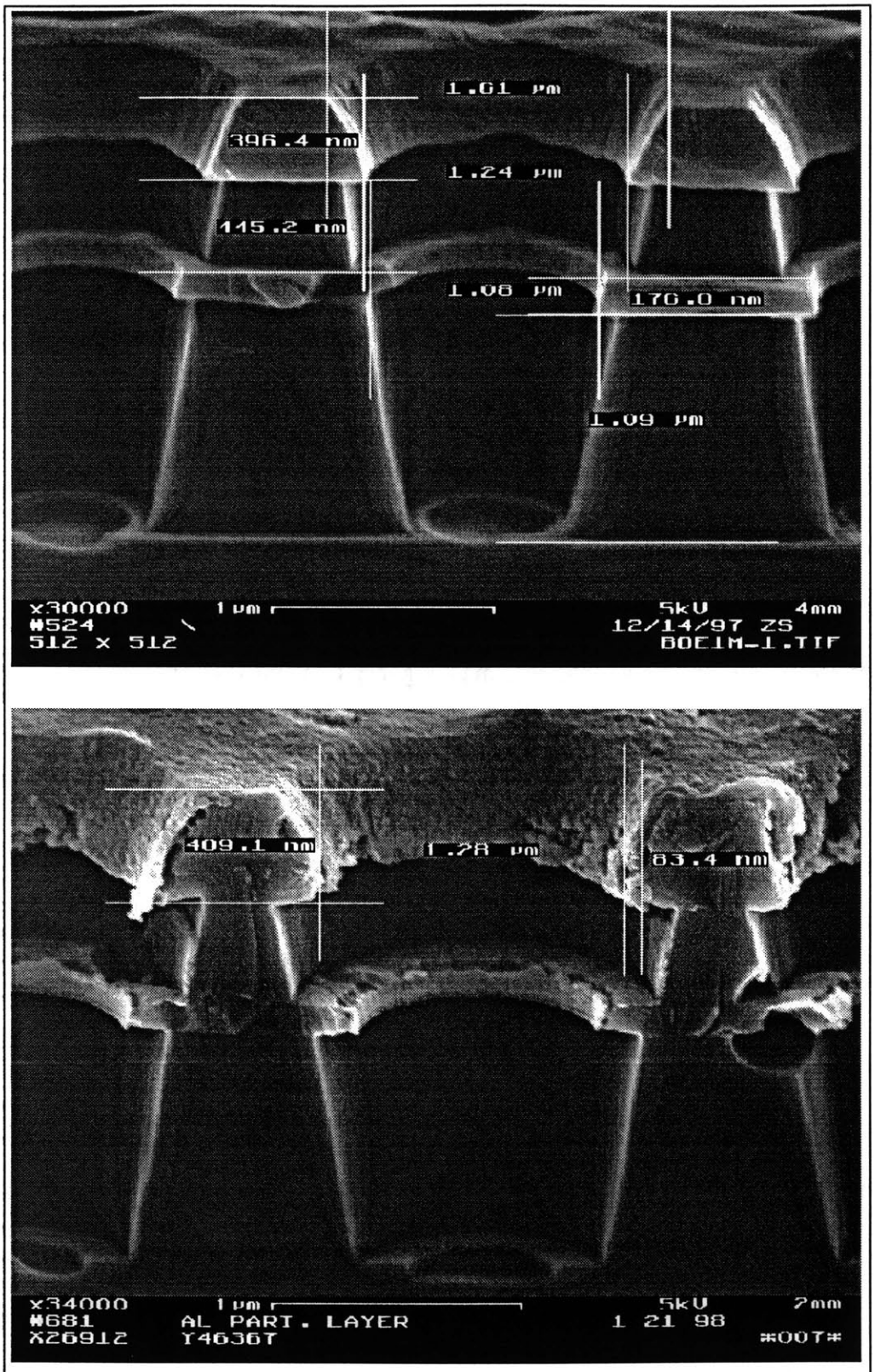

Figure 4.2 and 4.3 Emitter opening before (4.2) and after (4.3) Al parting layer evaporation (done at 35 degrees, ~ 3000 A.) Cf. Fig. 4.1e-f

Polysilicon of both gate and focus layers was etched as in the previous step; oxide was also etched with RIE plasma, in a different chamber of the same etcher. After the dry etch had reached the substrate, wafers were dipped in BOE for two and half minutes to recess the oxide under the electrodes, and then the remaining photoresist was striped by oxygen plasma. Figure 4.2 shows the devices after this step. (Note: figs. 4.2-4.6 show devices made during the first, unsuccessful, attempt. Figures from 4.7 on show completed devices, made on the second attempt.) Up to this point, with the exception of the CMP step, the process was CMOS compatible and has been carried out in ICL (Integrated Circuits Laboratory) – a class 10 cleanroom. Next, the wafers are taken to Technology Research Lab (TRL) – a class 100 cleanroom – for angular evaporation of the aluminum parting layer (fig. 4.3), done on a custom made evaporation plate. (Our attempts to deposit the parting layer by electroplating are described in Appendix B of this

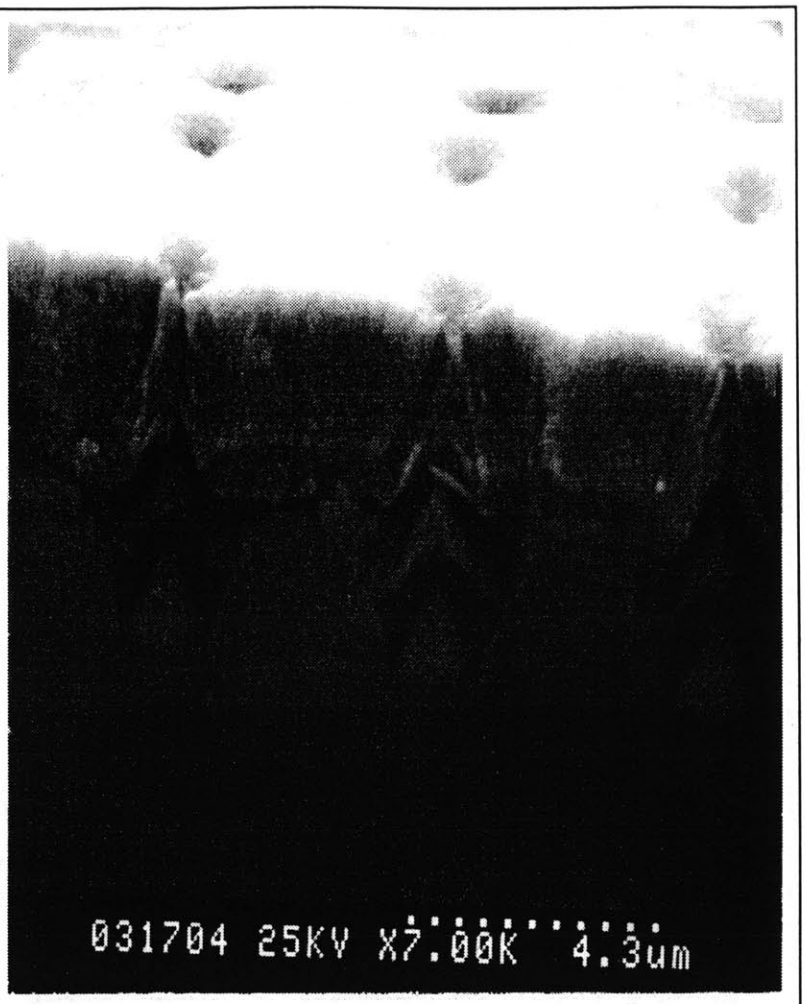

Figure 4.4 Mo cones before liftoff (note how the crack above the focus electrode damaged the rim of the focus aperture in the leftmost cone

chapter.) This is followed by a vertical evaporation of molybdenum (fig. 4.4), which was where we had encountered problems, to be described shortly. If the molybdenum evaporation was successful, devices were taken to an ultrasonic bath of sodium hydroxide to lift-off the Al parting layer and remove unwanted Mo. The lift-off was the second problem area.

The difficulty encountered during the deposition of the molybdenum layer was that the thick (17 kÅ) molybdenum film would peel due to built-in stress and take with it all of the underlying layers except the thermal oxide (fig 4.6). This would destroy both focus and gate electrodes. We tried depositing a thin layer of gold (a poor adhesive) on top of the aluminum before Mo evaporation. This was supposed to make the Mo film

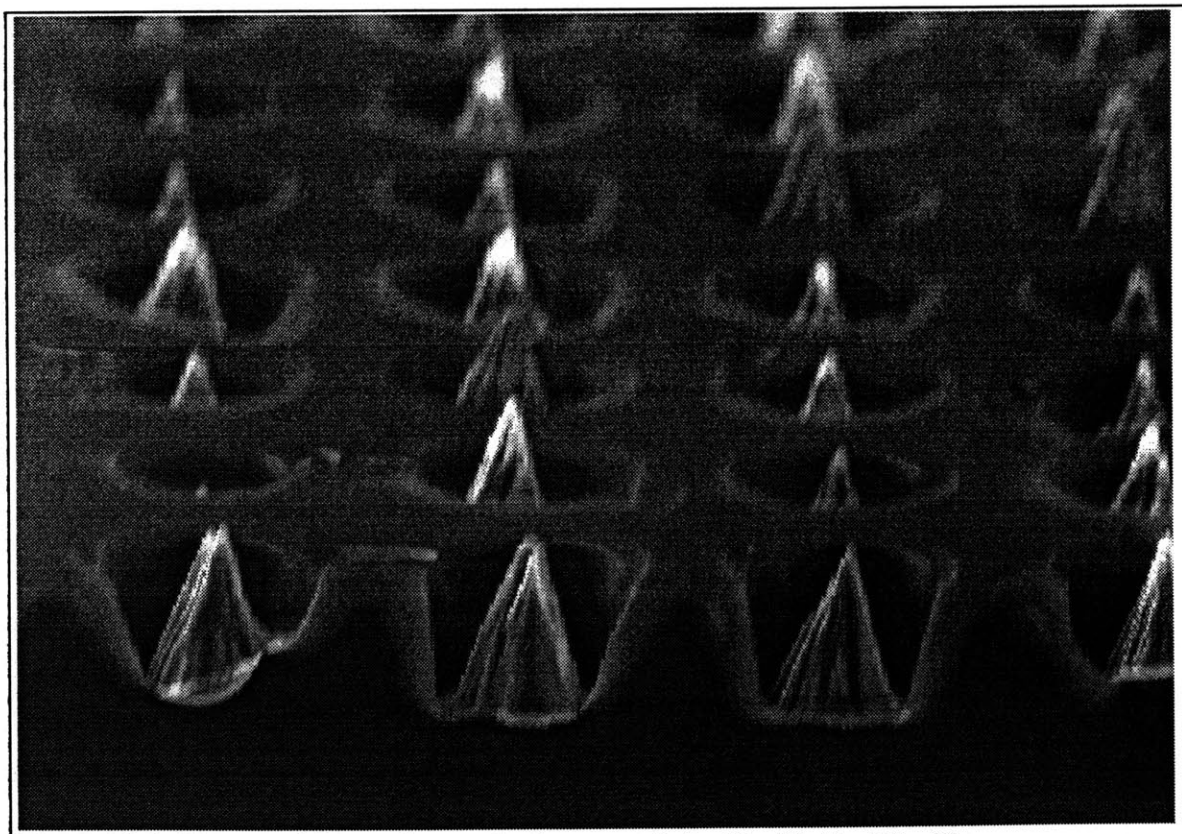

Figure 4.5 Gate and focus electrodes have peeled off with the Mo film

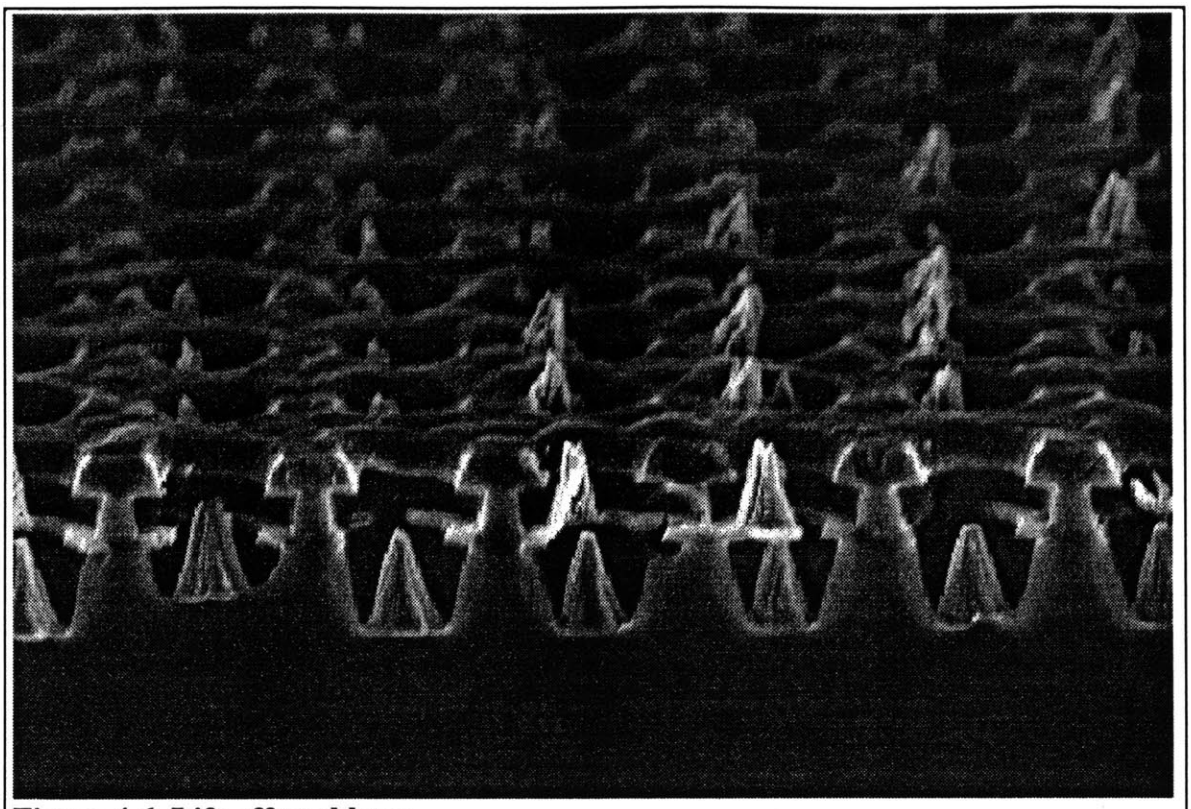

Figure 4.6 Lift-off problems

peel at the gold interface, without damaging the underlying layers. However, this technique did not fully solve the problem and did not always work.

The problem with the liftoff is illustrated on figure 4.6. The molybdenum deposited on the rim of the gate electrode (the bottom of the two electrodes) did not lift-off. These two difficulties defeated our first attempt at making an IFE FEA.

On the second attempt, we replaced Mo with chrome as the cone material. The peeling problem was not nearly as severe for chrome. Finally the combination of 12.5 kA Cr followed by 3.5 kA Mo showed no peeling and produced a working set of devices. The lift-off problem was solved by one or more of the following three techniques we used: 1. Suspecting that the aluminum target may be contaminated with crucible material (copper), we switched to single charge, i.e. "cruscibleless", targets. 2. We did two

angular evaporations, a shallow one followed by a deeper one. The idea was to limit the size of the top opening which would in turn limit the outer diameter of the buildup accumulated on the rim of the gate electrode. 3. During the 10 min lift off, samples were turned from the upside down position to the opening facing up position. This allowed any gas that might have been trapped in the openings to escape and thus permit the access of the etching solution.

Completed devices are shown on figures 4.7-4.11.

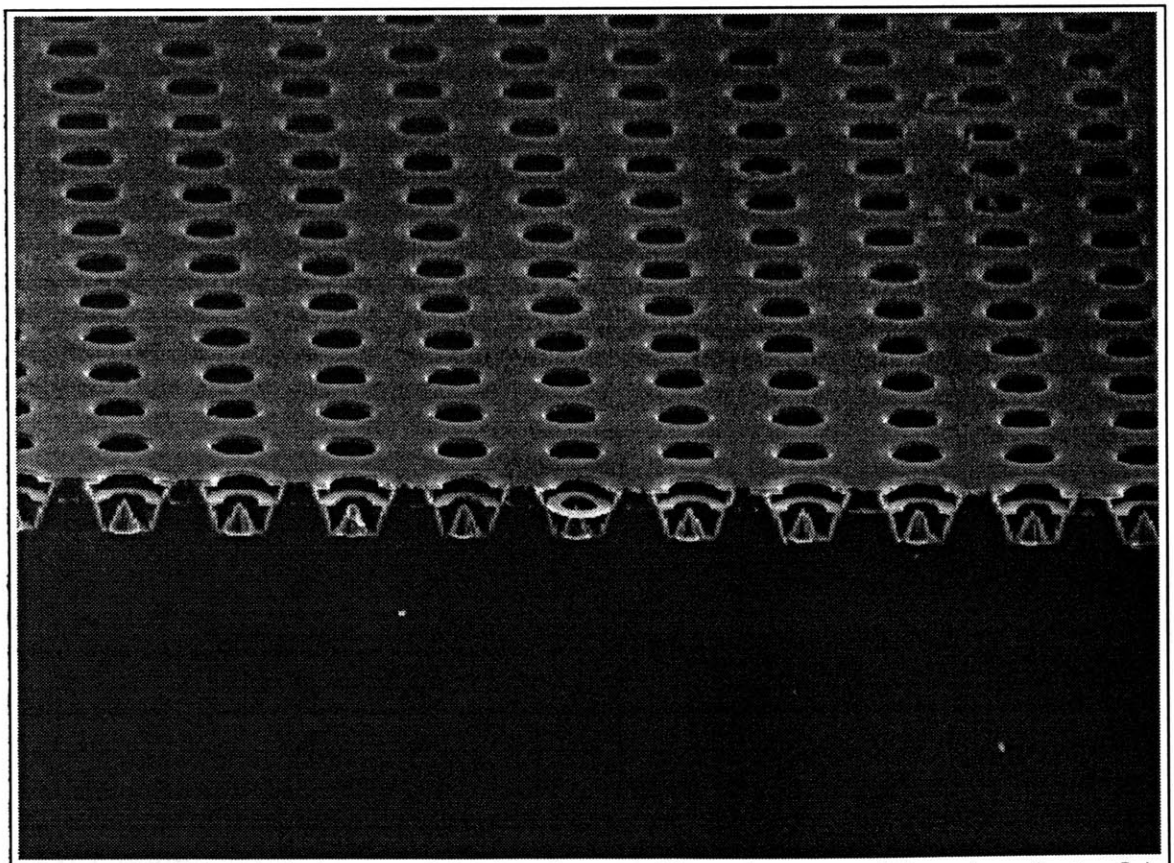

Figure 4.7 IFE FEA (array of field emitters with an integrated focusing electrode)

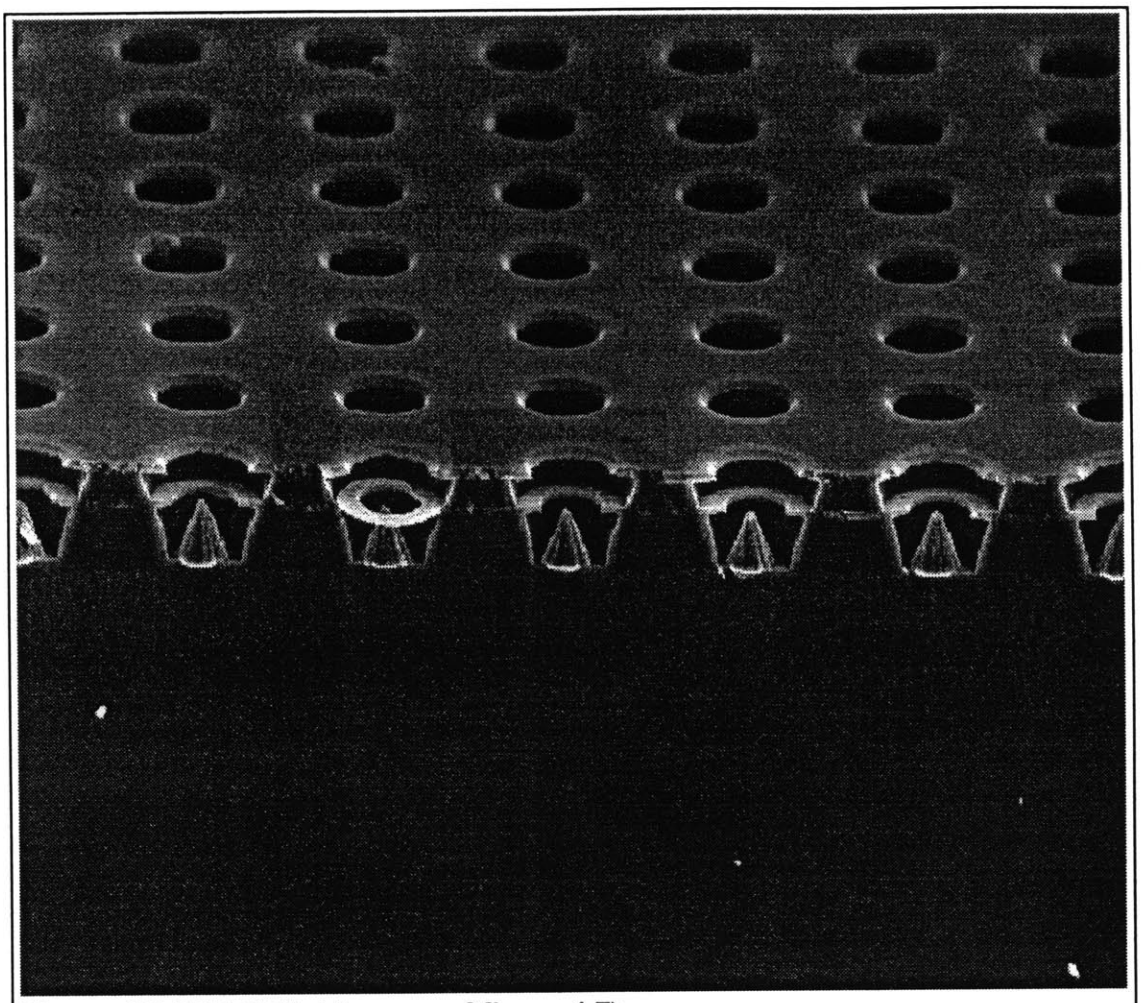

Figure 4.8 IFE FEA (close-up of figure 4.7)

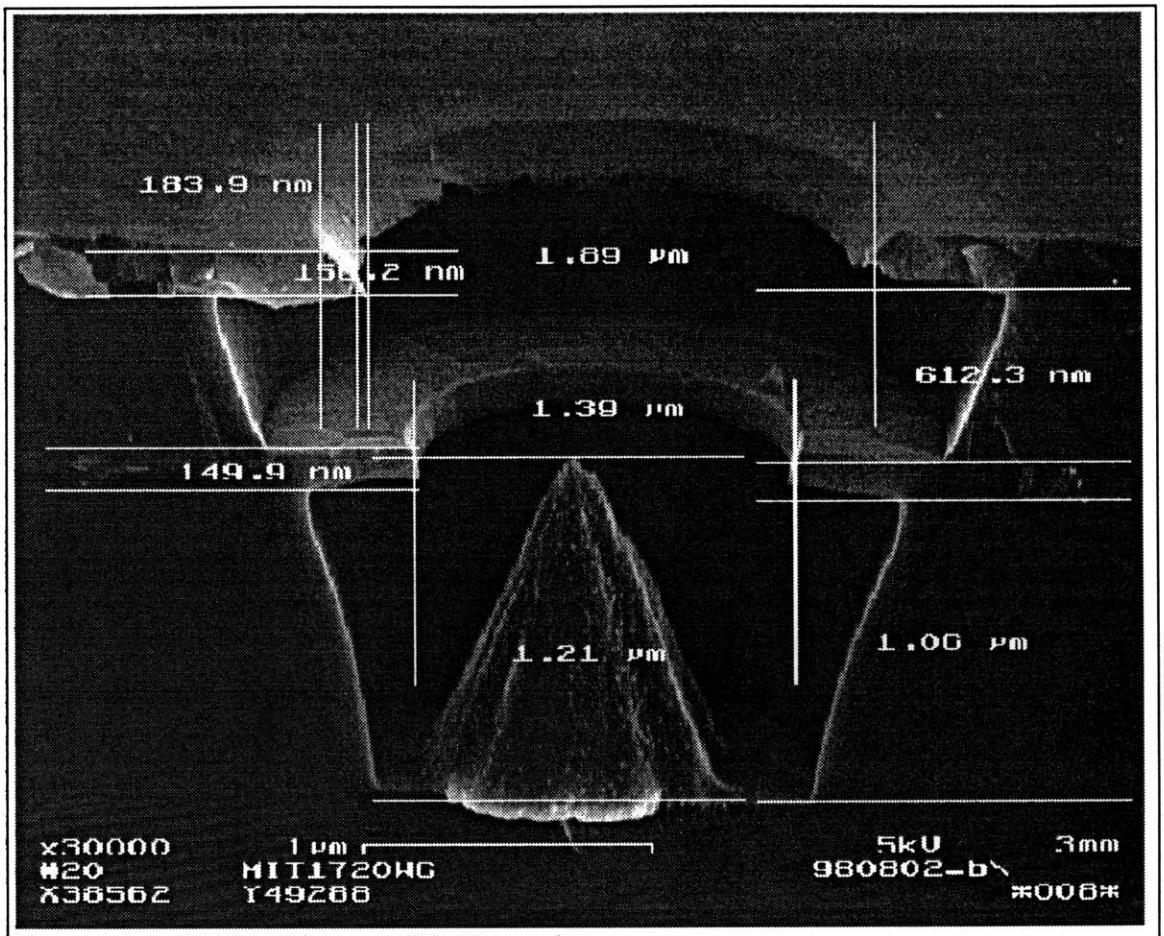

Figure 4.9 A IFE FE cone with dimensions.

Figure 4.10 A close-up picture of a sharp tip

Appendix A. Investigating the Use of Electroplating to Deposit the Parting Layer in FEA Fabrication.

If a parting layer is used in the fabrication of an FEA—as it is, for example, in Spindt cathodes—it is usually deposited by angular evaporation. We have explored the possibility of depositing the parting layer by electroplating. The possible advantages include applicability of this method to fabrication of large-area displays as well as a simpler set-up. Ni was chosen as the material for the parting layer because Al, the metal most commonly used for that purpose, is difficult to electroplate.

The following explains our process design and the mask layout. A die was designed to have square emitter arrays from 1x1 to 100x100 emitters, with the radii of the emitter openings going from 0.5 to 0.8 μm. Each die was also designed to have a number of test structures to examine leakage current between each pair of the electrodes as well as the relative magnitudes of the bulk vs. the edge leakage currents, and to provide feedback during various fabrication steps.

For the electroplating step, the electrodes of all the devices have to be shorted together, this is accomplished by mask # 1 which patterns the gate layer. (Electroless plating is unsuitable because it would deposit the parting layer everywhere, including the bottom of the opening. The deposited cone would then be destroyed during the parting layer lift-off.) Mask # 2, applied to the focus layer, defines the openings in which the emitter cones will be deposited. Mask # 3, applied after electroplating, isolates the different dies and the different devices from one another. Mask # 4 opens contacts to the gate layer pads. And Mask # 5 defines gate layer and focus layer pads for metallization.

We make gate and focus electrodes out of n^+ poly, rather than out of metal, for the following reasons: 1. To be able to deposit thermal oxide on top of the gate (for an isolation layer between gate and focus); this would be impossible with a metal gate since metal would contaminate the deposition tube 2. Poly electrodes have a higher resistance and thus are supposedly more stable against leakage current. However, precisely because of higher resistance poly proved to be a very poor electroplating base—only the area closest to the contact clip showed signs of plating, and the plated film was quite poor quality. After that we made a Pt polycide in an attempt to lower the resistance of the film and achieve better plating. (Although polycide, like metal, precludes deposition of thermal oxide.)

Ultimately, since the process called for five masks (and, according to one estimate, in a university environment 1 mask=1 month); required developing the electroplating step and building the electroplating setup; required developing the lift-off step for the Ni parting layer, we deemed the process too complicated to be pursued.

Appendix B. Chemical Mechanical Polishing of Polysilicon Electrodes.

The surface of polysilicon is covered with sparsely distributed bumps, about 2000 A in diameter and 500 A in height (fig. 4.12a) It is believed that these bumps appear when polysilicon is exposed to high temperatures (> 700-900 C), as during the doping step. Since these bumps can contribute to leakage and breakdown in the gate-to-focus LTO, in the second fabrication run, we decided to reduce surface roughness of both polysilicon electrodes by chemical-mechanical polishing. (CMP) We used the pressure of 1 LB, slurry flow rate of 150 ml / sec, and the polishing time of 45 sec. Figures 4.11b shows that CMP reduced surface roughness of polysilicon by a factor of 10-20. Maximum feature size was reduced from 200 nm to 10 nm, and average roughness went from 27 nm to 1.9 nm. About 500 A of polysilicon was lost to CMP (maybe around 700 A near the center of the wafer since CMP was somewhat nonuniform).

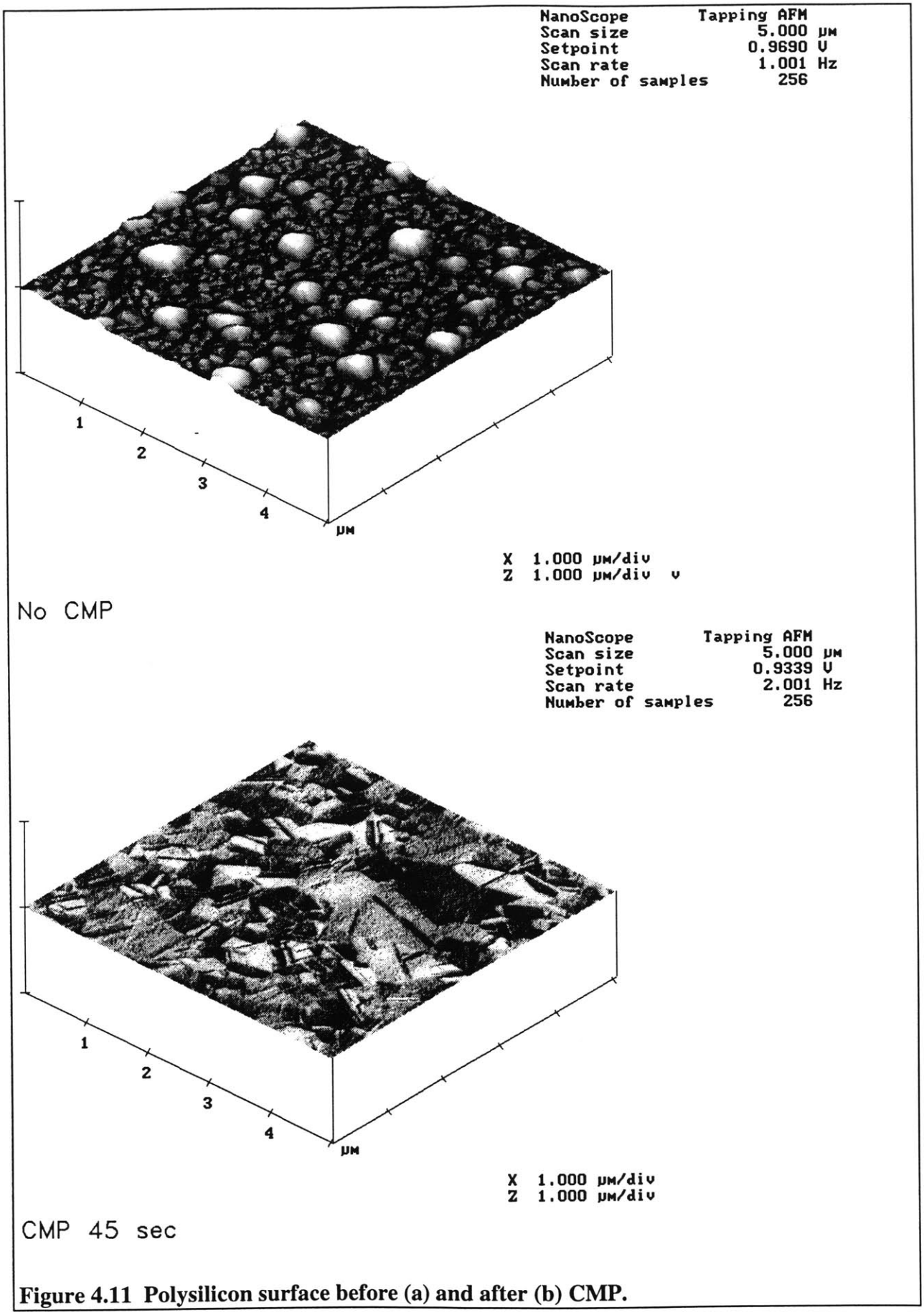

Figure 4.11 Polysilicon surface before (a) and after (b) CMP.

CHAPTER 5

CHARACTERIZATION OF IFE FEA

5.1 Measurement setup and strategy.

Measurements on the devices were carried out in a UHV chamber, at pressures of order 10^{-10} Torr. Instrumentation consisted of an ultrasensitive current meter, Keithly 6517; three Source-Measure units (Keithly 237), capable of simultaneously sourcing voltage and measuring current (or vice versa) at the same pair of terminals; Labview, a computer interface program which provided remote control of the instruments and collected the data over the GPIB.

Electrical contact to the gate and focus electrodes of the device was obtained through ultrasharp probes positioned on the sample with the aid of a microscope and micromanipulators. To eliminate vibration that would break the probe contacts, the whole UHV chamber was mounted on a floating optical table. Since the cathode of the device was built right on the wafer substrate, it was contacted directly through the metallic stage on which the wafer was mounted. (The stage was isolated from ground.) Shielded triaxial cable was used for all signals to minimize noise and interference. For *electrical* characterization (see below), the anode was a rectangular piece of Si wafer covered with platinum (labeled Anode 1 in Figure 5.1). For *optical* measurements, the anode was a phosphor screen (labeled Anode 2 in Figure 5.1) operated at 10 kV with a custom built power supply. (The power supply, which I built for this project, is capable of measuring currents as low as 1 nA while sourcing voltages as high as 15 kV.) The setup of the above components is shown on figure 5.1.

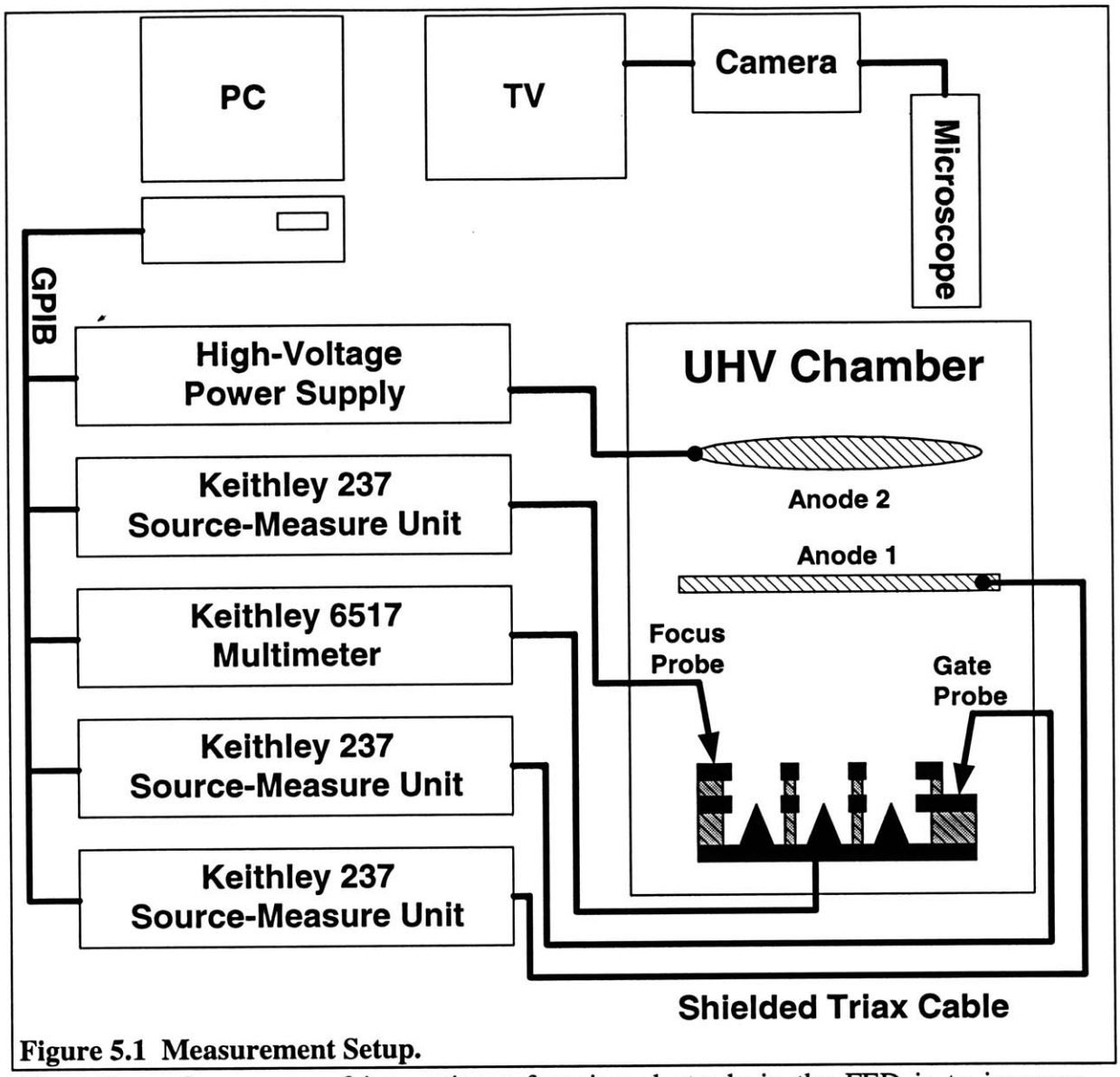

Figure 5.1 Measurement Setup.

Since the main purpose of integrating a focusing electrode in the FED is to improve display resolution, the ultimate characterization of IFE FEA should include optical measurements. However, at the present stage, since we do not yet have all of the necessary optical equipment, we only carried out preliminary optical characterization of the devices and devoted most of our attention to electrical measurements.

From the standpoint of electrical characterization, IFE FEA is ultimately a 4-terminal device; thus, it is different from typical FED's, which are 3-terminal devices.

However, we began the electrical characterization by operating IFE FEA as a 3-terminal device, which is done by keeping the gate and focus electrodes at the same voltage. Then, we carried out four terminal measurements, aimed particularly at determining the gate and focus transfer characteristics.

5. 2 Three terminal IV characteristics.

In these measurements we held gate and focus voltages equal to each other (V_G=V_F) and swept them from 0 to 100 Volts in steps of 2 Volts, keeping the anode voltage constant (V_A=1000 V), and measured the four currents – I_E, I_G, I_F, and I_A (emitter, gate, focus, and anode). We observed that at least 99% (in some cases >99.9%) of emission current is captured by the anode; thus, in the following figures we take anode current – rather than emitter current, which contains a small leakage component -- to be equal to emission current. Figures 5.2 and 5.5 show respectively linear and semilog plots of anode current vs. gate voltages for arrays of different sizes. Figure 5.3 is a zoom-in of figure 5.2 around the x-axis, showing turn-on voltages of different devices. With the anode at 1000 Volts, typical leakage currents were about 150 pA; with electronic nulling this can be reduced to below 50 pA, which is the noise floor for measurements of turn-on voltage. Turn-on voltage of various devices, defined here as the voltage at which emission current begins to rise above the noise floor, is seen to be 42-56 V, except for the single emitter device, whose turn-on voltage is around 72 Volts.

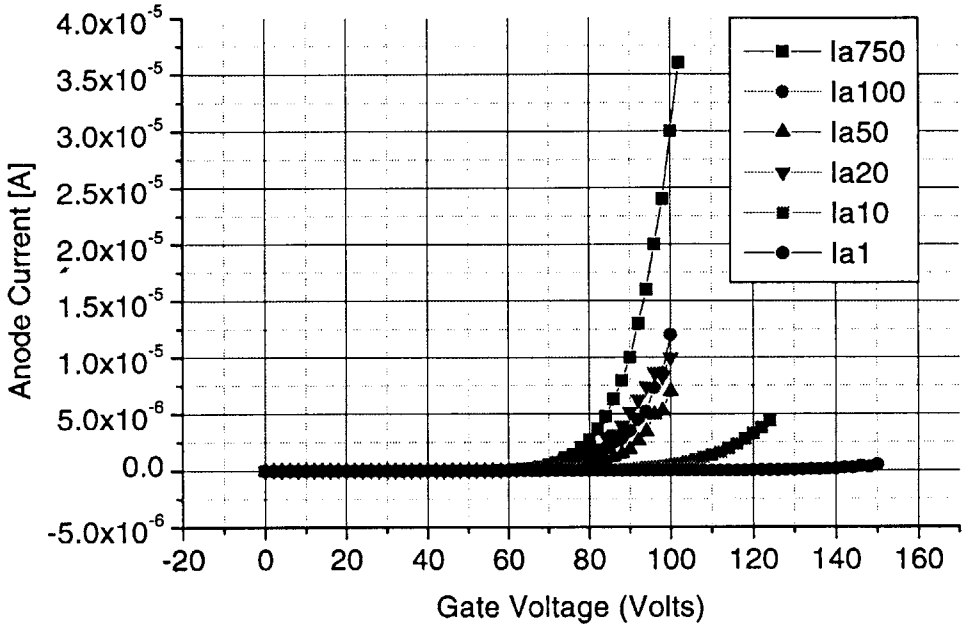

Figure 5.2 Plots of anode current vs. gate voltage for arrays of different sizes

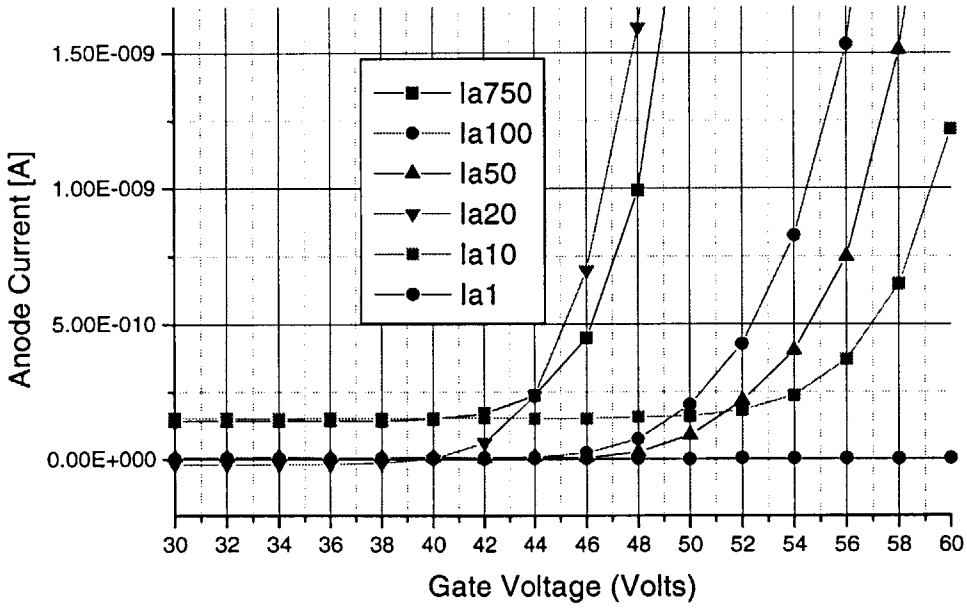

Figure 5.3 Zoom in around I=0 shows turn-on voltages for devices on fig. 5.1

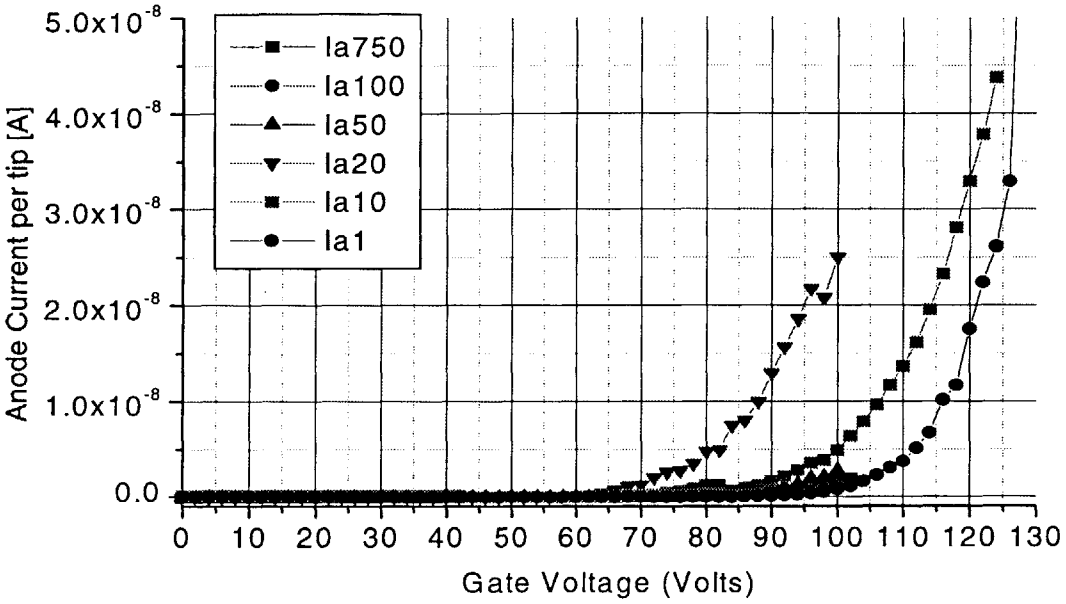

Figure 5.4 Anode current per tip vs. gate voltage for devices on fig. 5.1

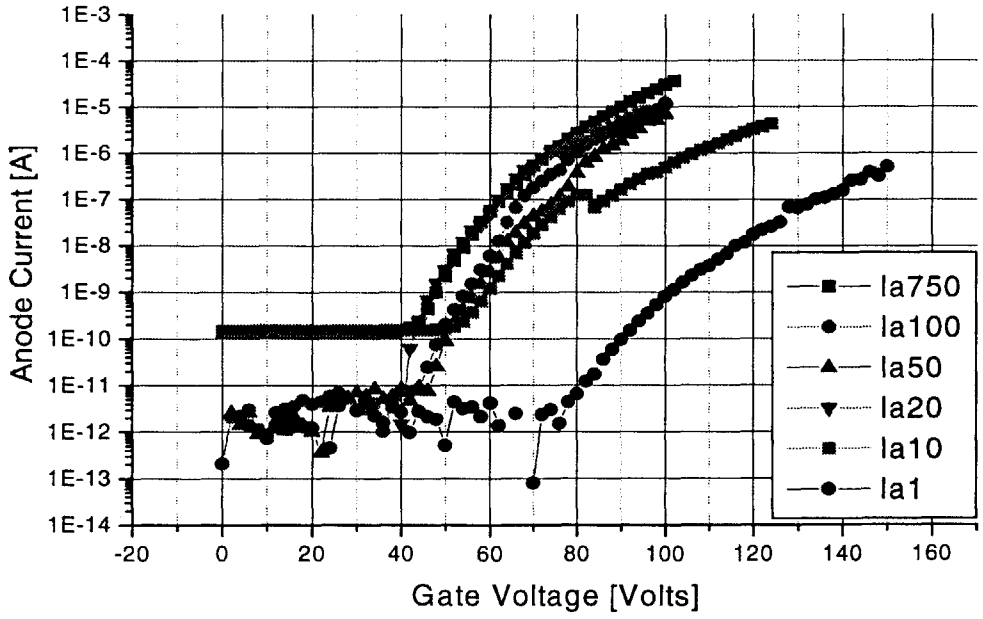

Figure 5.5 Semilog plots of anode current vs. gate voltage for arrays of different sizes (same data as on figure 5.2)

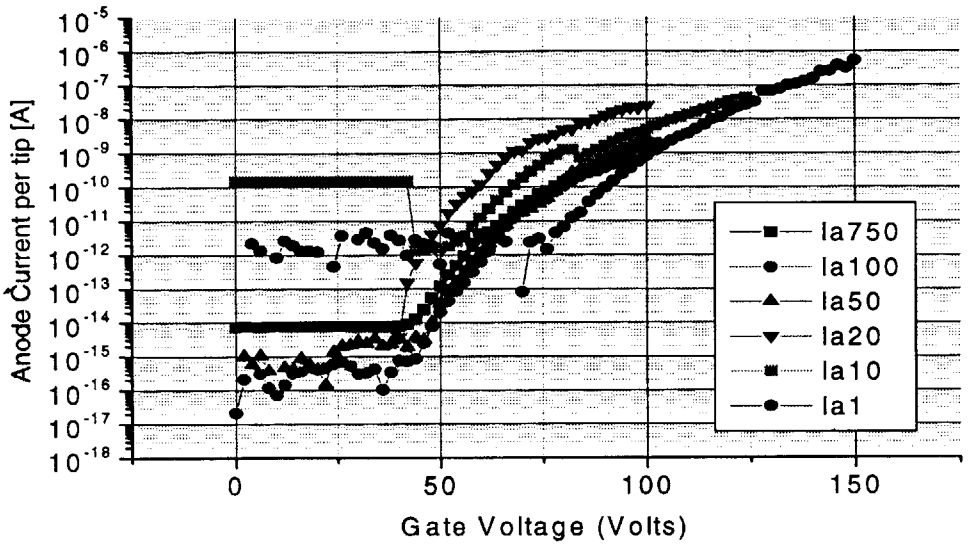

Figure 5.6 Semilog plots of anode current per tip vs. gate voltage for arrays of different sizes (same data as on figure 5.4)

Figures 5.4 and 5.6 contain the same data as figures 5.2 and 5.5, but normalized to the number of tips for each array. Among the devices shown, the 20x20 array, denoted by ∇, is seen to have the lowest turn-on voltage and the highest emission current.

Next, we examine Fowler-Nordheim plots of the total anode current data, shown on figures 5.7 - 5.12. The parameters of the linear fits for different arrays are summarized in Table 5.1. The intercept, A_{FN}, is related to the total emitting area and hence to the number of operating tips; the slope, B_{FN}, is related to field enhancement and thus to tip sharpness and gate radius, as well as to focus-to-tip distance. Standard deviation, SD, and the R parameter show how much data deviates from the linear fit.

Table 5.1. Summary of Fowler-Nordheim parameters of the total current data.

Array	A_{FN}	B_{FN}	SD	R
1 x 1*	-5.78	-736	0.054	-0.99927
10 x 10	-5.40; -6.23; -6.36	-423; -402; -392	0.019(01, 010)	-0.99969(99: 32)
20 x 20	-2.55; -6.74	-513; -219	0.068; 0.073	0.998; 0.973
50 x 50*	-4.36	476	0.067	0.9989
100 x 100	-4.55	426	0.124	0.995
25 x 750	-11.56	803	0.052	0.99978

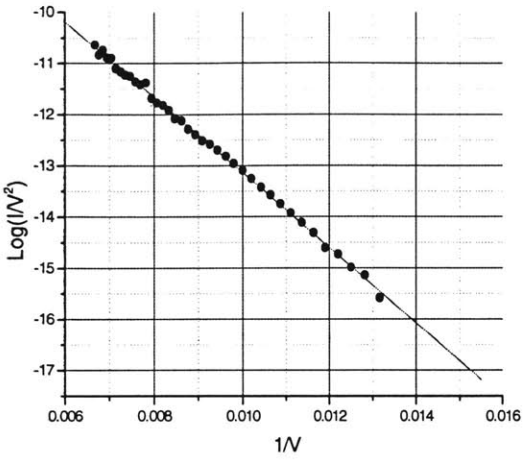

Figure 5.7 FN plot for a 1x1 array

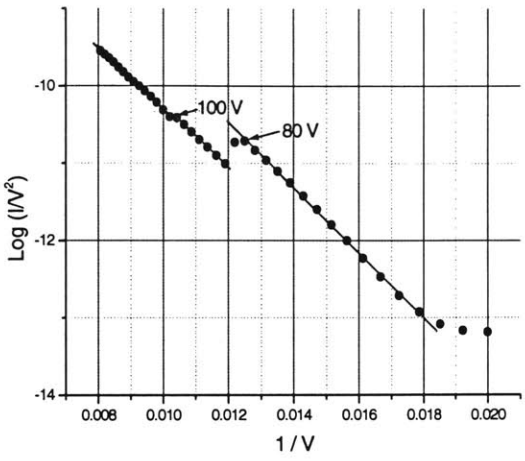

Figure 5.8 FN plot for a 10x10 array

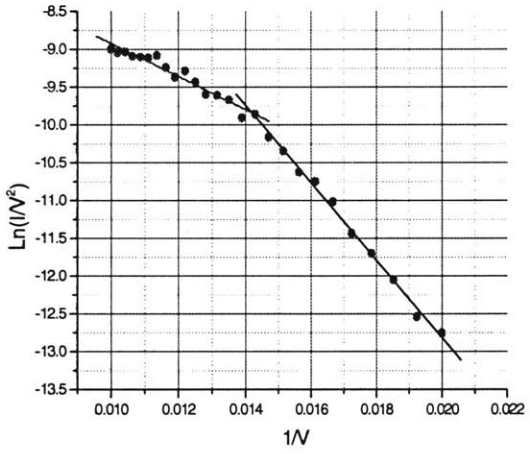

Figure 5.9 FN plot for a 20x20 array

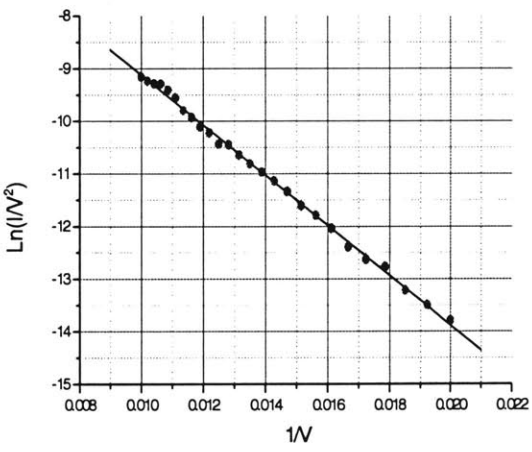

Figure 5.10 FN plot for a 50x50 array

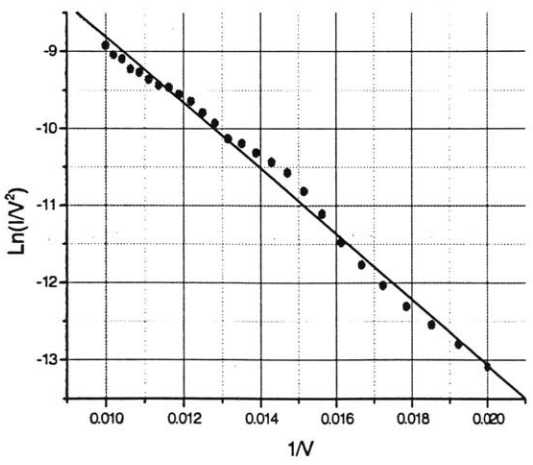

Figure 5.11 FN plot for a 100x100 array

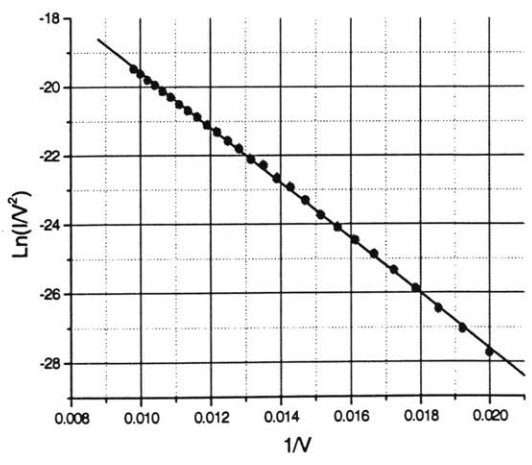

Figure 5.12 FN plot for a 25x750 array

The high-voltage end of the 50x50 data shows what could be a saturation effect, which becomes more pronounced in the 20x20 data, leading to the hypothesis that smaller arrays are subject to saturation. However, this was not confirmed by the 10x10 and 1x1 data, intentionally taken out to higher voltages. The 10x10 data does show a discontinuity at V_G=80 V. Since the two lines have almost the same slope and differ only at intercept, the discontinuity could be due to the change in the number of operating emitters, as is the case when one of the emitters blows up or dies. However, this would be inconsistent with the fact that the discontinuity is repeatable, as demonstrated in figure 5.13, which shows the data for gate voltage swept 0 V - 125 V - 0 V. At present, we do not know the cause of such repeatable discontinuities.

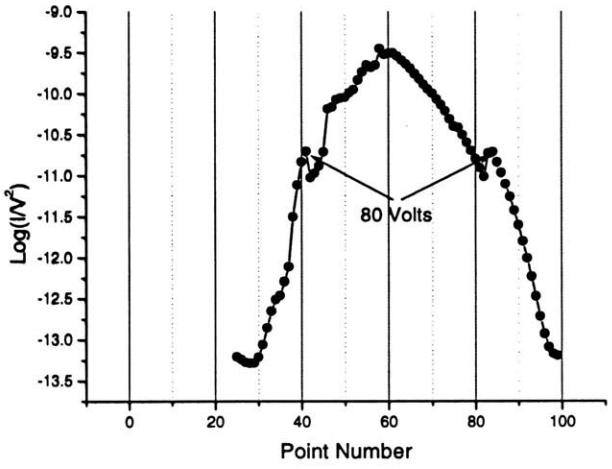

Figure 5.13 Discontinuities in the FN data plot of the 10x10 array

5.3 Four Terminal IV Characteristics

This section will discuss the following three types of data: A.– Output characteristics, namely anode current as a function of anode voltage, with gate and focus voltages held constant. B.—Focus transfer characteristics, i.e. gate and anode voltages are held constant, while the focus voltage is varied. This measurement is particularly

relevant to operating IFE FEA's in the focusing mode. C.— Gate transfer characteristics, whereby gate voltage is varied and anode and focus voltages are kept constant.

5.3.A Output characteristics

The data on current variation with anode voltage, shown on figures 5.14-5.16 is explained as follows: in the proper IFE FEA operation mode, virtually all of the emitted current is captured by the anode. This mode ensues when anode voltage is approximately 300-400 V. When anode voltage is below 300-400 V, an increasing fraction of the emitted current is captured by the focus and gate electrodes. After electrons pass the plane of the focus electrode, if there is no anode field to pull them up, the weak uniform field of the focus and gate electrodes (that are at around 100 V) eventually prevails and pulls the electrons back down. Most of the recaptured electrons land on the top electrode and a smaller number are pulled back into the opening; thus the focus electrode captures a greater percentage of current than the gate (fig. 5.14-5.15). The electrons captured by the gate are the ones that were initially emitted almost vertically up and thus have small transverse velocity. They come from a fairly small area immediately around the apex, which is also the area of maximum emission. Thus, the gate current is comparable to focus current even though it probably originates from a small fraction of the total emitting surface. It may be argued that electrons captured by the gate never leave the emitter aperture in the first place and are actually emitted at very large angles (e.g. straight into the gate). However, inside the aperture the anode field is dwarfed by the fields of the surrounding gate and focus electrodes regardless of how big it is; thus, the anode cannot

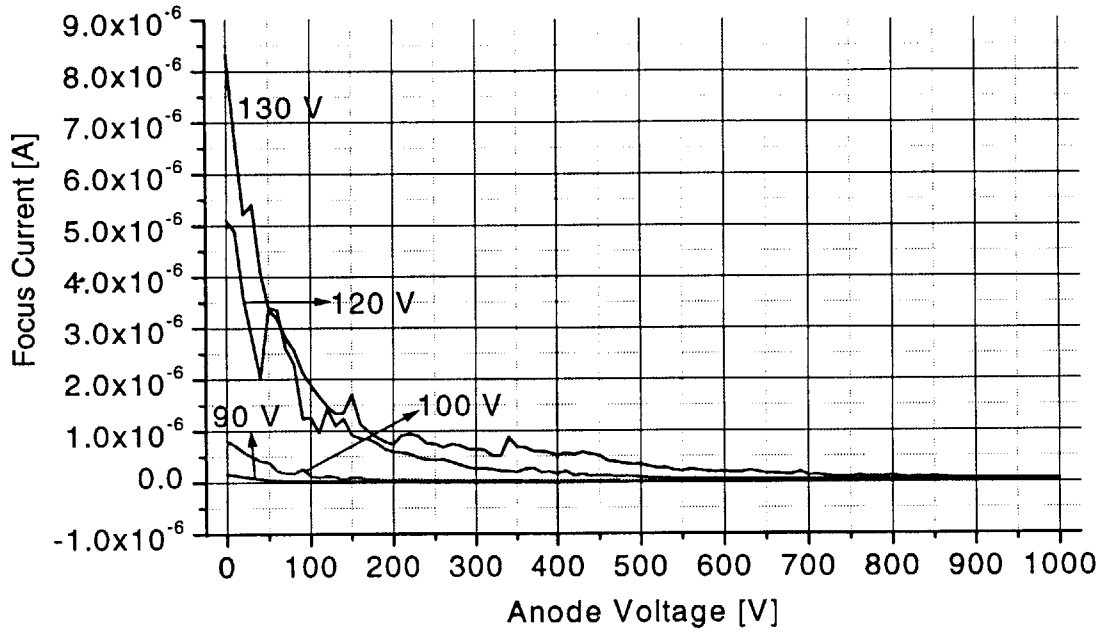

Figure 5.14 Focus current vs. anode voltage for different values of V_G (=V_F)

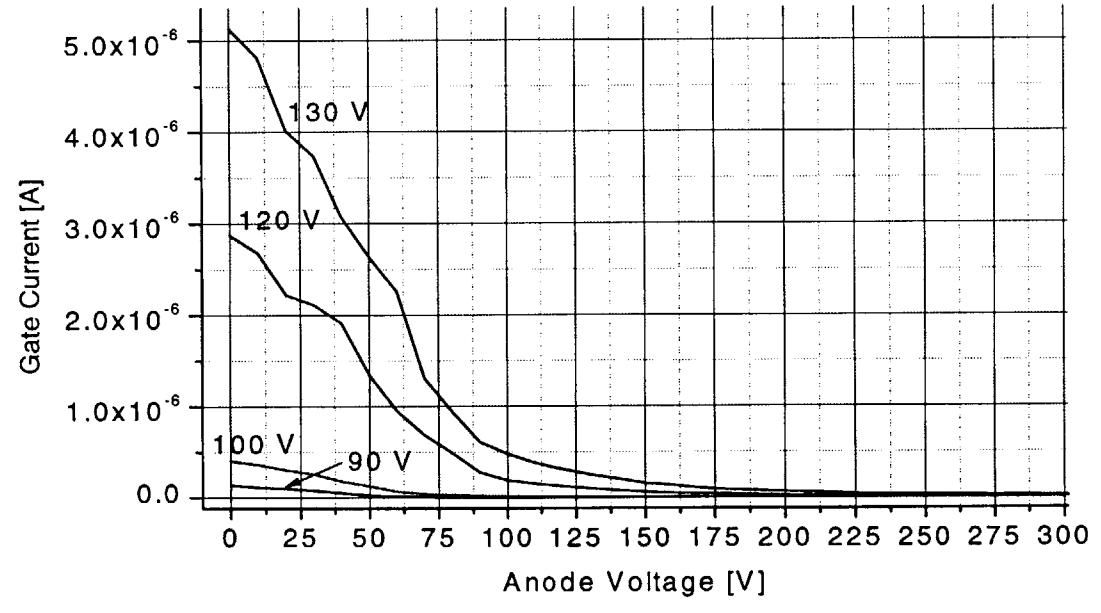

Figure 5.15 Gate current vs. anode voltage for different values of V_G (=V_F)

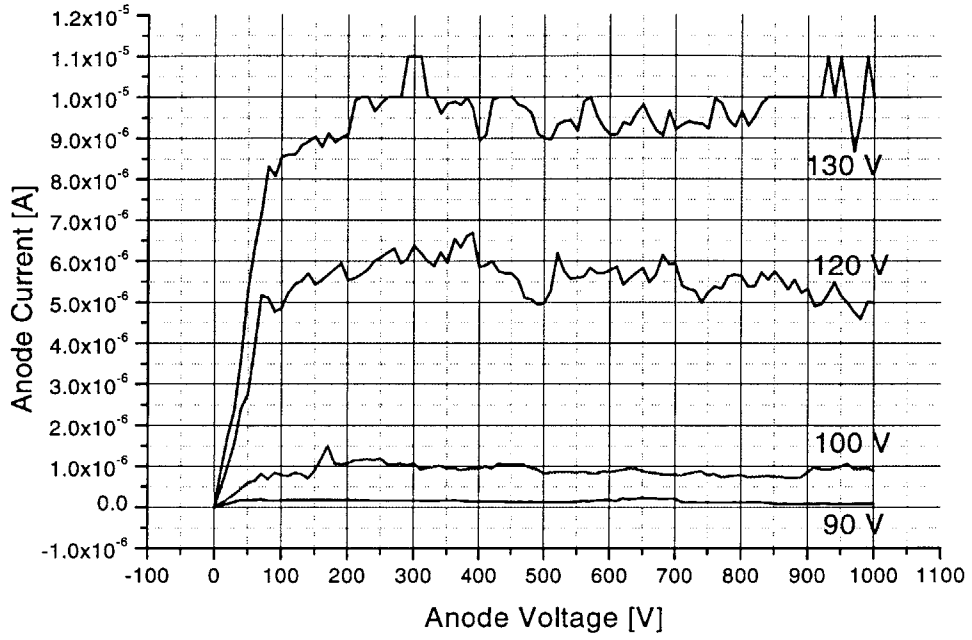

Figure 5.16 Anode current vs. anode voltage for different values of V_G (V_F)

change the trajectories that stay below the plane of the focus electrode (or a small distance above it.) The fact that application of anode voltage eliminated gate and focus currents proves that the electrons captured by the gate and focus electrodes in the absence of anode voltage actually escape the aperture before being pulled back

5.3.B Gate and Focus Transfer Characteristics.

The device used for measurements of gate and focus transconductance characteristics (sections B and C) was a 20x20 array, different from the devices described above. To measure FTC (focus transconductance characteristics), shown on Figure 5.17, gate voltage was kept constant at 80 V, anode voltage was kept constant at 1000 V, and

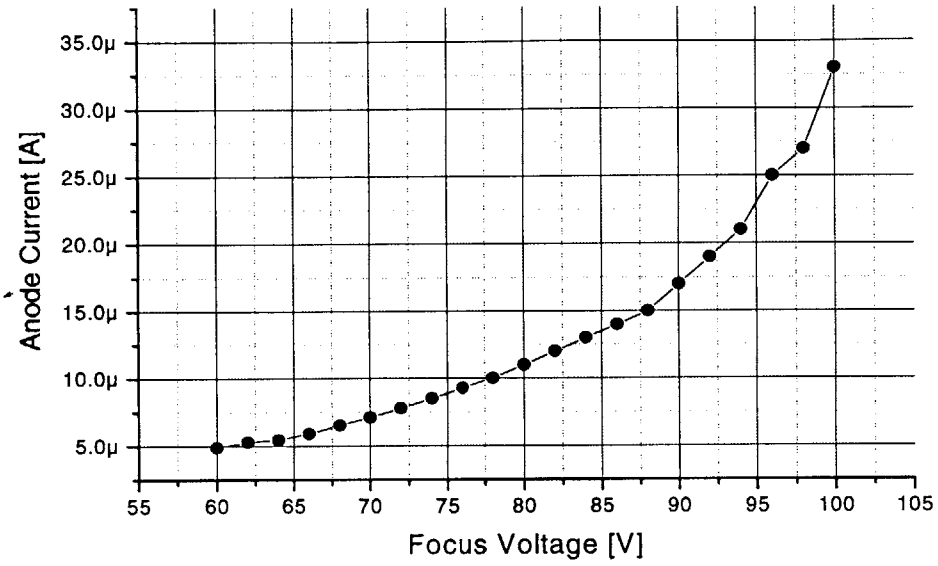

Figure 5.17 Emission current vs. focus voltage, with V_G = 80 V. (Focus Transfer characteristic)

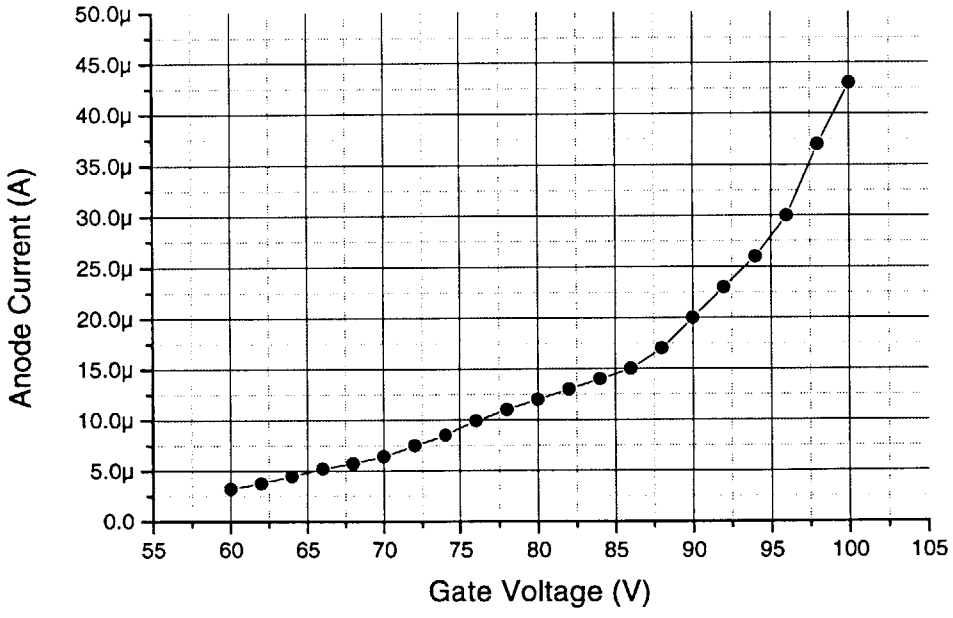

Figure 5.18 Emission current vs. gate voltage, with V_F = 80 V. (Gate Transfer Characteristic)

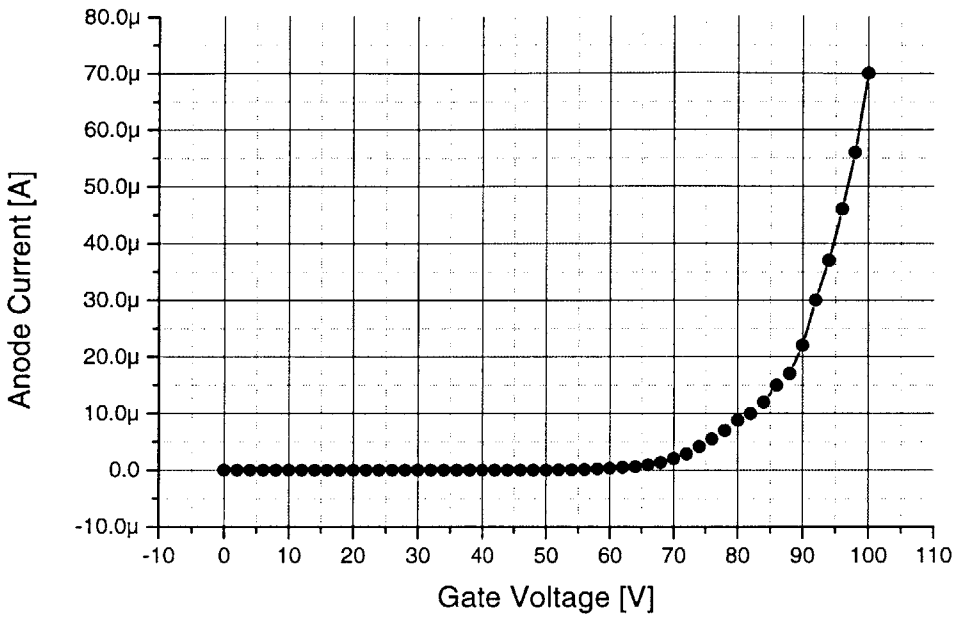

Figure 5.19 Three terminal characteristic of the same device as fig. 5.17, 5.18.

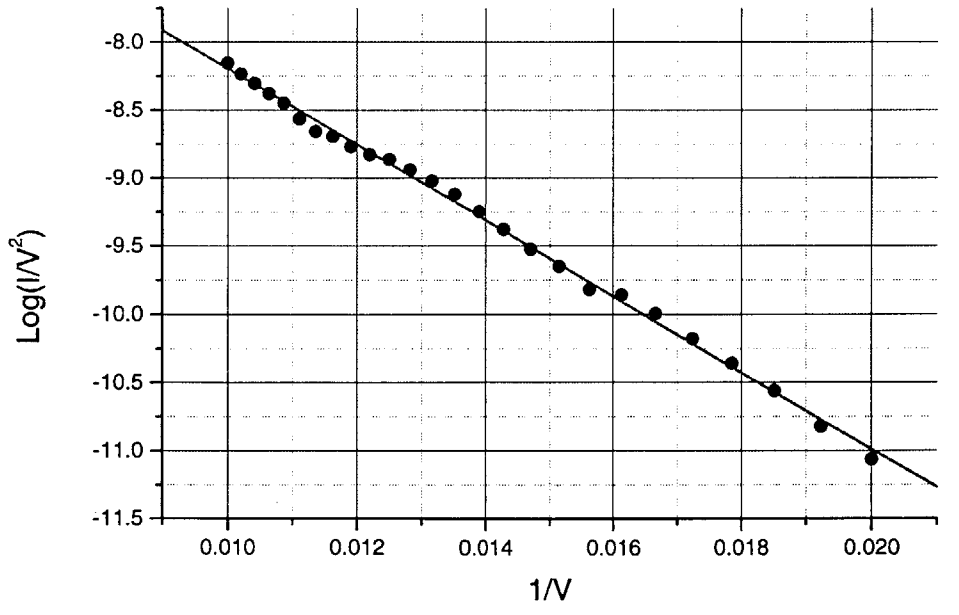

Figure 5.20 FN plot of the data on figure 5.19. A_{FN}=-5.4; B_{FN}=-279; SD=.044; R=-.9986

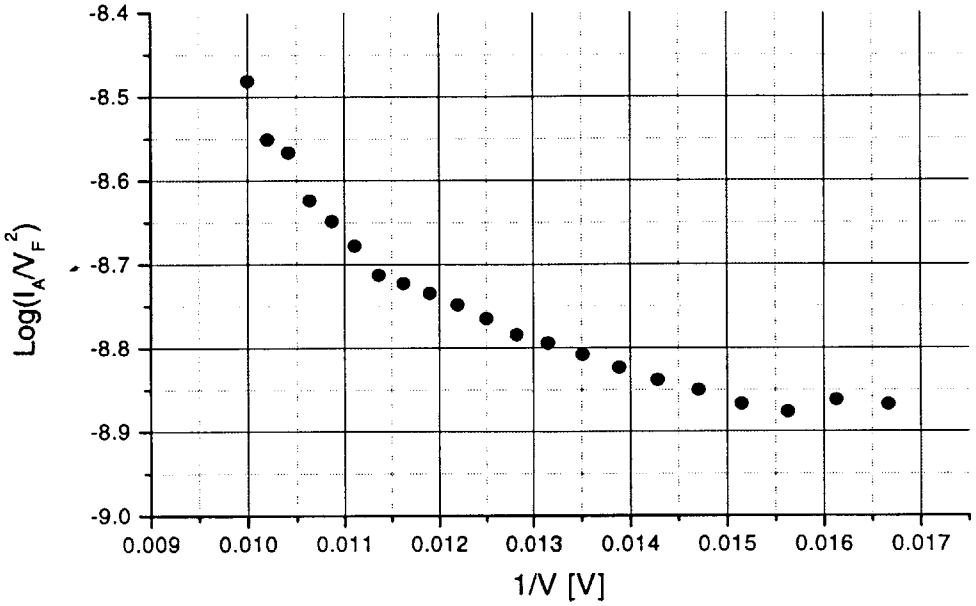

Figure 5.21 FN plot of data on fig. 5.14. (Focus Transfer Characteristic)

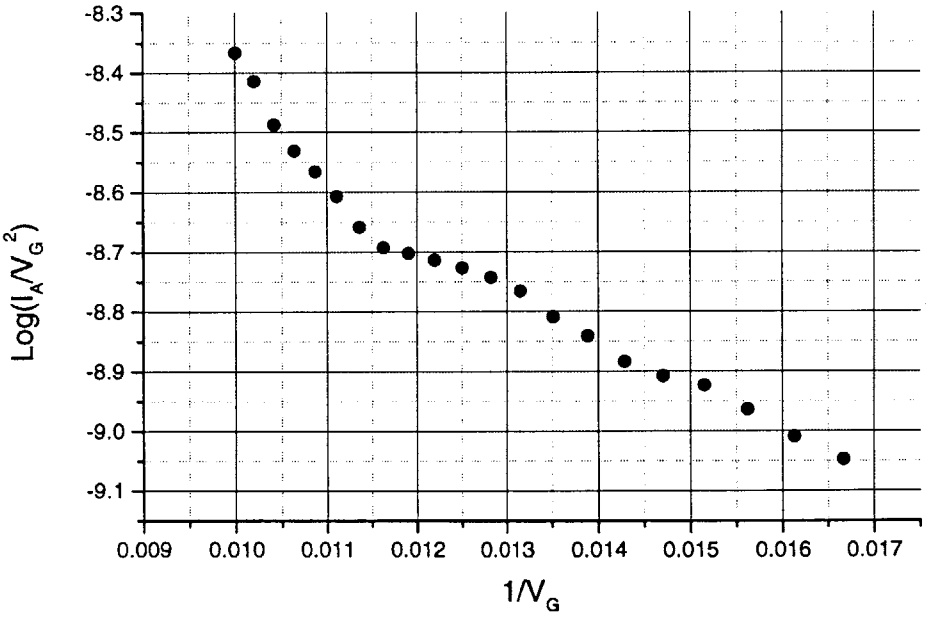

Figure 5.22 FN plot of data on fig. 515 (Gate Transfer Characteristic)

focus voltage was varied from 60 to 100 V in steps of 2 V. In the measurements of focus transfer characteristics and gate transfer characteristics (below), we tried to avoid having the voltage difference between gate and focus electrodes exceed 20 Volts so as not to risk or contribute to device breakdown.

To measure GTC (gate transconductance characteristics), focus voltage was kept constant at 80 V, and gate voltage was varied from 60 to 100 V. Figure 5.18 shows the data. As expected, GT is greater than FT.

It may come as a surprise that the FN plots of GTC and FTC (fig. 5.21, 5.22) are clearly not linear. In all 3-terminal FED's, as well as in our 4-terminal FED's tested in the 3-terminal mode, the FN plot of the IV characteristic is linear. The derivation of the analytical form of such plots from the FN equation and correspondig computations of FED parameters based on the FN data are presented in one of the first FED papers [C. Spindt et al , J. Appl. Phys, Vol. 47, No. 12, Dec 1976]. In the following section, we aim to extend that analysis to the case of 4-terminal FED's and then compare the resulting predictions to our data.

5.3.C Analytical Picture of Transfer Characteristics.

To derive the equations for the transfer characteristics of a 4 terminal FED, we start with the Fowler-Nordheim equation.

$$J = \frac{AE^2}{\phi t^2(y)} \exp\left[-B\frac{\phi^{3/2}}{E} v(y)\right] Amp/cm^2 \qquad (5.1)$$

where E is the electric field on the surface, in V/cm; J is the emitted current density; ϕ is the work function in eV,

$$A = 1.54 \times 10^{-6},$$
$$B = 6.87 \times 10^{7},$$
$$y = 3.79 \times 10^{-4} \frac{E^{1/2}}{\phi},$$
$$t^2(y) = 1.1,$$
$$v(y) = 0.95 - y^2.$$

After setting $J = \alpha I$, where I is the measured current, simple algebra can transform equation (1) into

$$I = aE^2 e^{-b/E} \tag{5.2}$$

$$a = \frac{\alpha A}{1.1\phi} \exp\left[\frac{9.9}{\phi^{1/2}}\right]$$
$$b = 0.95B\phi^{3/2}$$

In a 3-terminal FED, which has only one gate electrode, the typical substitution is $E = \beta V_G$. Here we use linear superposition of the effects of gate and focus voltages and write

$$E = \beta_G V_G + \beta_F V_F \tag{5.3}$$

Then, equation (5.2) becomes:

$$I = a\left(\beta_G V_G + \beta_F V_F\right)^2 \exp\left[-\frac{b}{\beta_G V_G + \beta_F V_F}\right] \tag{5.4}$$

At this point, it becomes clear (eq. 5.4) why linearity is lost in the FN plots of the 4-terminal FED (figs. 5.21-22).

As compared to the 3-terminal FED, 4-terminal FED gives rise to two additional parameters useful for describing device behavoir. They are the partitial derivatives of the total current with respect to gate and focus voltages, i.e. gate and focus *transconductances*:

$$G_{MG} \equiv \left.\frac{\partial I}{\partial V_G}\right|_{V_F} = \frac{\beta_G I(V_G, V_F = const)}{\beta_G V_G + \beta_F V_F}\left(2 + \frac{b}{\beta_G V_G + \beta_F V_F}\right)$$
$$G_{MF} \equiv \left.\frac{\partial I}{\partial V_F}\right|_{V_G} = \frac{\beta_F I(V_G = const, V_F)}{\beta_G V_G + \beta_F V_F}\left(2 + \frac{b}{\beta_G V_G + \beta_F V_F}\right) \tag{5.5}$$

Earlier we have mentioned several times that application of the focusing voltage reduces the emission current, and that this reduction can be overcome by increasing the gate voltage. Now, the gate and focus transconductances give us a way to calculate the relative magnitudes of the effects of the gate and focus electrodes, i.e. to extract the ratio of gate and focus voltage enhancement facotrs. This is done as follows:

$$\frac{G_{MG}(V_G = V_F)}{G_{MF}(V_F = V_G)} = \left.\frac{\partial I}{\partial V_G}\right|_{V_F = V_G} \Big/ \left.\frac{\partial I}{\partial V_F}\right|_{V_G = V_F} = \frac{\beta_G}{\beta_F} \tag{5.6}$$

Equations 5.3-5.6 describe the 4-terminal FED operated in the 4-terminal mode. To get the complete analytical picture of device behavoir, we need to derive the corresponding equations for the 4-terminal FED operated in the *3-terminal* mode. (As we shall see, these will be very similar to the equations governing a regular 3-terminal FED.)

When the device is operated in the three-terminal mode, i.e. when $V_G = V_F \equiv V$, equation (5.3) reduces to

$$E = (\beta_G + \beta_F) V . \tag{5.7}$$

And we can define the total transconductance,

$$G_{MT} \equiv \frac{dI}{dV} = \frac{I}{V}\left(2 + \frac{b}{V(\beta_G + \beta_F)}\right) \tag{5.8}$$

Now we can write down a total of three important conditions that hold when $V_G=V_F$:

1. $G_{MG} + G_{MF} = G_{MT}$;
2. $\frac{G_{MG}}{G_{MF}} = \frac{\beta_G}{\beta_F}$;
3. This should be the point of intersection of all three IV curves – gate transfer characteristic IV (fig. 5.18), focus transfer characteristic IV (fig. 5.17) and total (three-terminal) IV (fig. 5.19).

Next, we proceed to compare our transfer characteristic data (fig. 5.17-5.19) to the above analysis. We start by interpolating the data and then differentiating them. This yields transconductances as continuos functions of current and the corresponding voltage. (These operations are performed in Mathematica.) Figures 5.23 and 5.24 show the IV transfer and transconductance functions.

At the point where $V_G=V_F=80$ Volts, these functions give:

	Current [μA]	Transconductance, dI / dV[μS]
I vs. V_G	11	0.49
I vs. V_F	12	0.52
I vs V ($V_G=V_F$ data)	8.79	0.86

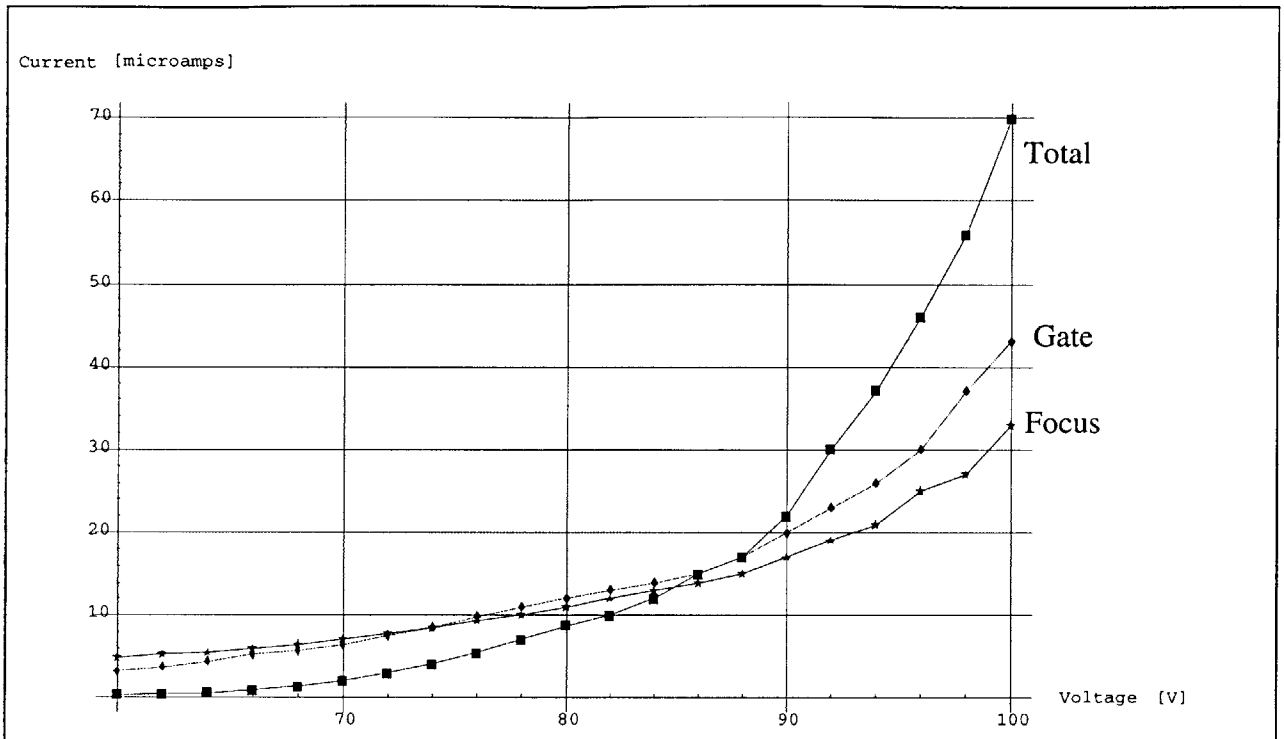

Figure 5.23 IV transfer functions.

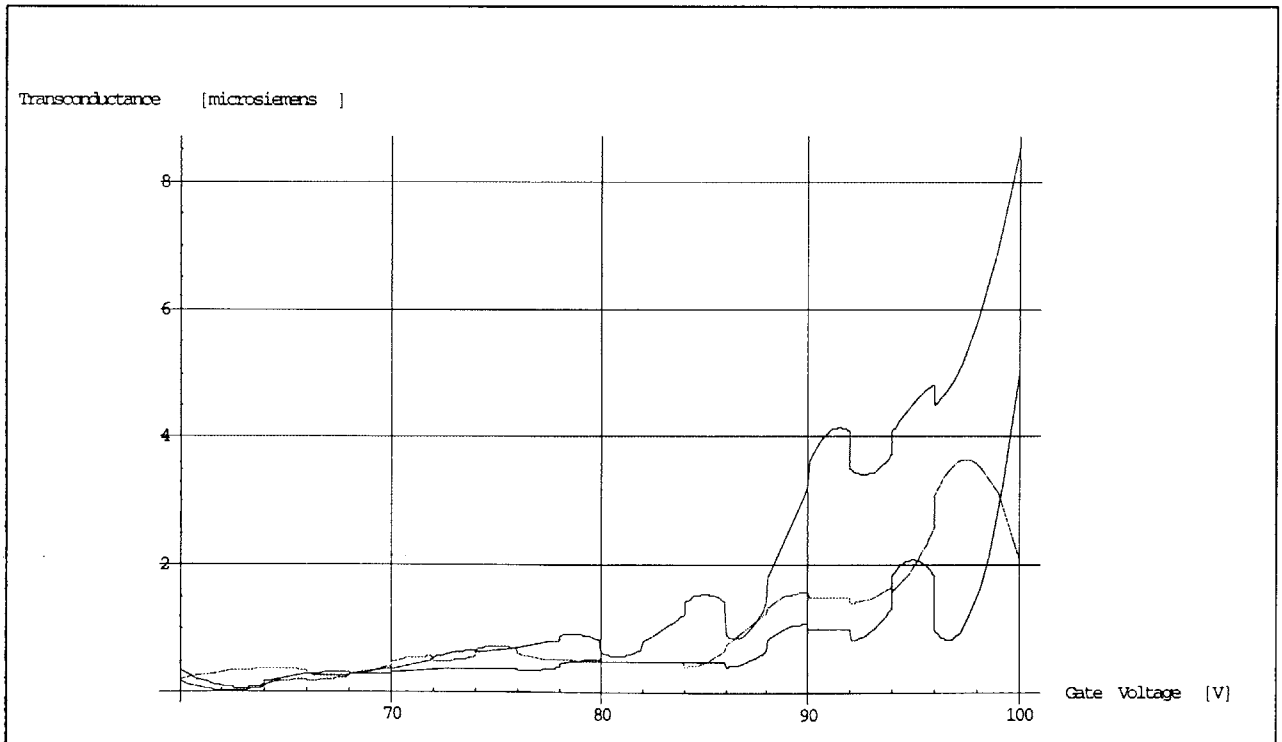

Figure 5.24 Transconductance functions: Total (the top curve at 100 V); Gate (bottom at 100V); and Focus (middle at 100 V)

Obviously, there were strong temporal fluctuations in the data, thus the three currents are not equal; focus transconductance exceeds the gate transconductance; and the sum of gate and total transconductances is 20% higher than the total transconductance.

In conclusion, we can say that we have derived the equations for the transfer characteristics and transconductances of a 4-terminal FED. Although our data is does not agree with the analytical predictions, we attribute the differences primarily to fluctuations and noise in the data.

5.4 Other electrical characterization

The subject of this section – dependence of the data on anode proximity and probe position – is important to know for future device design (positioning of contact pads in relation to device active area) as well as for avoiding systematic errors in the data.

5.4.A Effect of probe proximity.

To examine this dependency we collected data from two different 20x20 arrays – one laid out such that contact pads were within 200 microns from the emitters, and the other with contact pads about 2 mm away from the emitters. (On second thought, it may have been more conclusive to simply measure the device with 2 mm leads twice – the first time with the probes on the pads, 2 mm away from the emitters, and the second time with the probes on the leads, within 200 microns of the emitters.) The effect of probe proximity would be increased current to the gate and focus, as the probes capture a fraction of the emission current. Of course, there would also be a corresponding decrease in anode current, but since anode current is much higher, this decrease would be much harder to see. Hence, below I present three-terminal IV data showing emitter, gate and focus currents vs. gate voltages for two different devices. The data is summarized in Table 5.2.

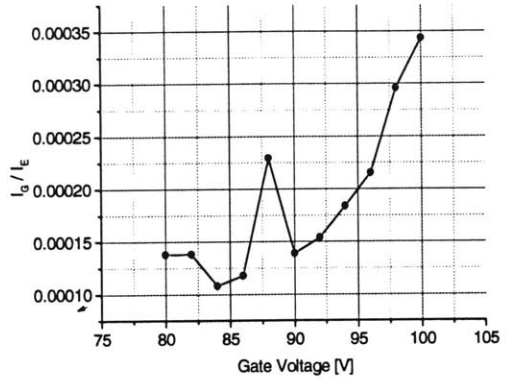

Figure 5.25 I_G / I_E vs. Gate Voltage for a device with 2mm leads.

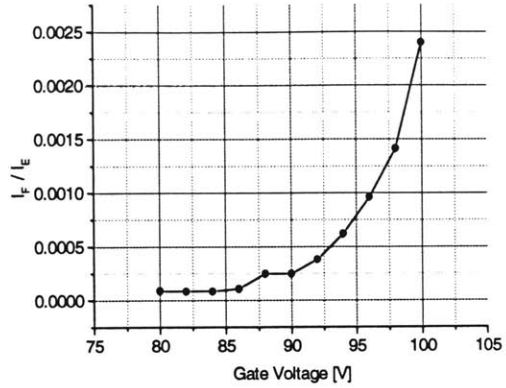

Figure 5.26 I_F / I_E vs. Gate Voltage for the device with 2 mm leads

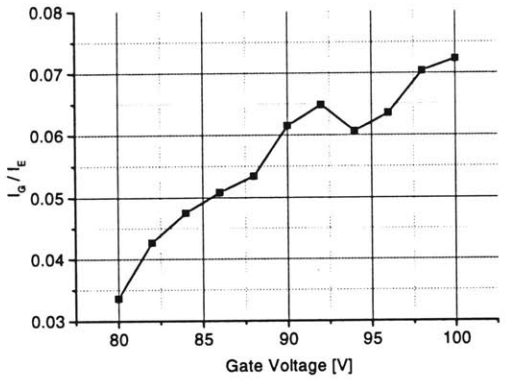

Figure 5.27 I_G / I_E vs. Gate Voltage for a device without leads

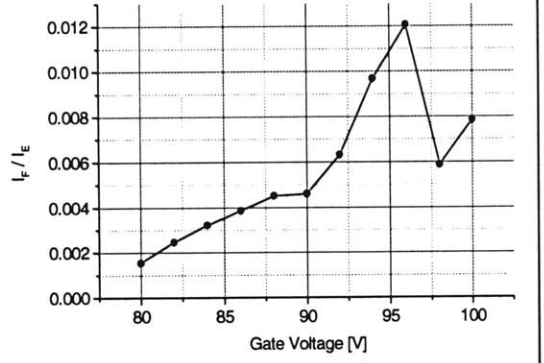

Figure 5.28 I_F / I_E vs. Gate Voltage for the device without 2 mm leads.

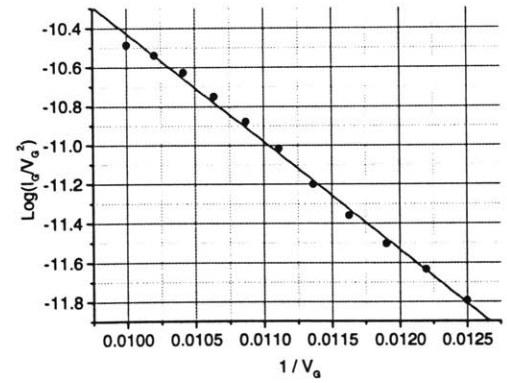

Figure 5.29 FN plot of data on fig. 5.27 proves that gate current is due to FE.

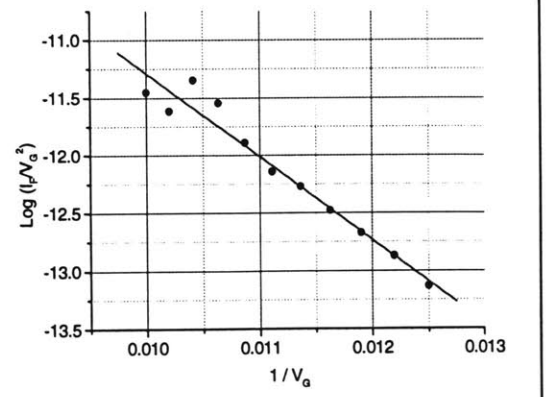

Figure 5.30 FN plot of data on fig. 5.28 proves that focus current is due to FE.

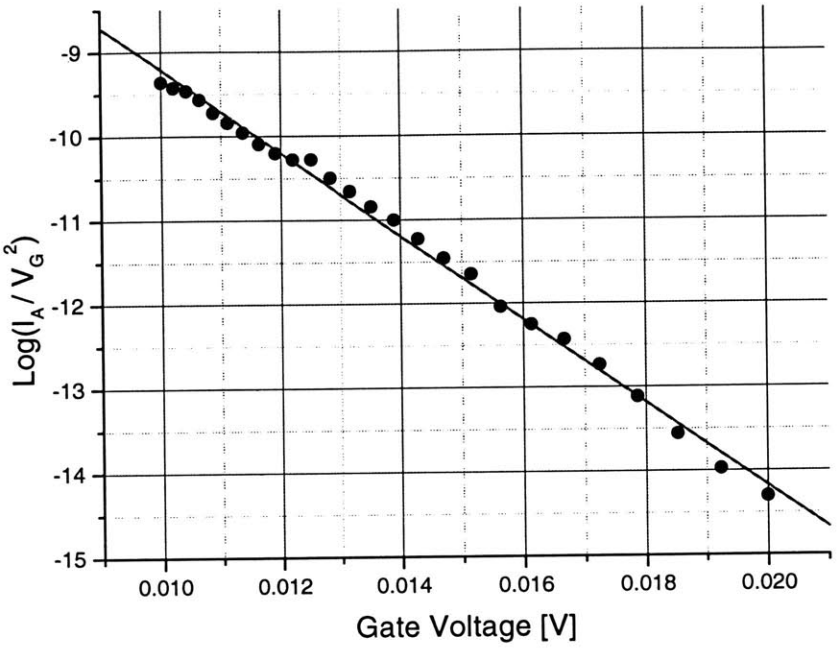

Figure 5.31 FN plot of anode current for the device without leads (cf. Fig 5.24-25)

Table 5.2. Summary of the effects of probe proximity (3T measurements, V_G=V_F).

	IG / IE @ VG = 100 V	IF / IE @ VG = 100 V	Intercept of FN plot, A_{FN}	Slope of FN plot, B_{FN}	SD of FN plot
Device with 2 mm leads	0.035 %	0.25 %			
Device w/out leads	7.2 %	0.8 %	-4.92±0.14 (I_G) -4.1± 0.58(I_F) -4.25±0.1 (I_A)	-551±12 (I_G) -721±51 (I_F) -496±7 (I_A)	0.03 (I_G) 0.13 (I_F) 0.11 (I_A)

Thus, it can be concluded that probe proximity causes the total of gate and focus currents to increase from a negligible fraction to about 8 % of emitter current. On the other hand, since the data with and without leads comes from different devices, it is possible that the second device simply has higher leakage currents. However, FN plots of gate and focus currents (figs. 5.29, 30) prove that this increase is indeed due to field-emission current.

The obvious assumption is that this field-emission current is due to the electrons emitted by the microtips being intercepted by the probes. (The competing hypothesis is that it's due to electrons tunneling through the *oxide*.) However, this is not quantitatively corroborated by the data. If the field emission current from the cone tip is split between the gate, the focus and the anode, we can write (using eq. 5.2)

$$I_E = aV^2 e^{-b/V} \equiv Total\ Current$$

$$I_G = C_G \times aV^2 e^{-b/V}; \quad I_F = C_F \times aV^2 e^{-b/V}; \quad I_A = C_A \times aV^2 e^{-b/V};:$$

It is immediately obvious, that if the anode, focus, and gate currents *are* described by these equations, their FN parameters can be written:

$$B_{FN}^{(G)} = B_{FN}^{(F)} = B_{FN}^{(A)} = -b;$$
$$A_{FN}^{(G)} = \ln(C_G) + \ln(a); \quad A_{FN}^{(F)} = \ln(C_F) + \ln(a); \quad A_{FN}^{(A)} = \ln(C_A) + \ln(a);$$
$$\Rightarrow A_{FN}^{(A)} - A_{FN}^{(G)} = \ln\left(\frac{C_A}{C_G}\right); \quad A_{FN}^{(A)} - A_{FN}^{(F)} = \ln\left(\frac{C_A}{C_F}\right);$$

In reality, the slopes of the FN plots of gate, focus and anode currents differ by about 3-4 error bars -- a possibly acceptable margin since the data is noisy -- while the relationship between the intercepts is given by the following:

$$A_{FN}^{(A)} - A_{FN}^{(G)} - = -4.2 + 4.9 = 0.7; \quad A_{FN}^{(A)} - A_{FN}^{(F)} = -4.2 + 4.1 = -0.1$$

$$\ln\left(\frac{C_A}{C_G}\right) = \ln\left(\frac{0.92}{0.072}\right) = 2.55; \quad \ln\left(\frac{C_A}{C_F}\right) = \ln\left(\frac{0.92}{0.008}\right) = 4.74;$$

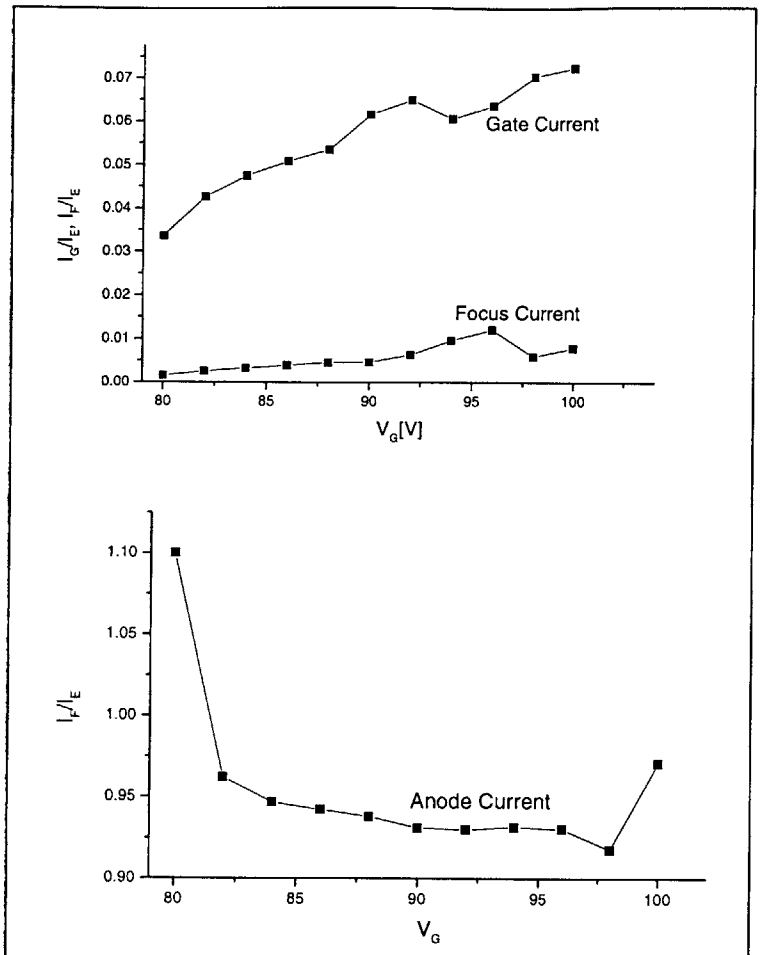

Figure 5.32 Ratios of Gate, Focus and Anode currents to the Emitter current.

Without further error analysis, it is clear that the values obtained from the intercepts disagree considerably. However, the values used in the above equation for C_A, C_G and C_F are taken at V_G=100 V. Figure 5.32 shows that in fact these values change considerably in the range $80V<V_G<100V$. Thus, in conclusion we can only say that noise and fluctuations in the data preclude a quantitative verification of our assumption that increased gate and focus currents are due to electron interception by the probes.

5.4.B Effect of anode-cathode separation

Electrons are attracted to the anode by an electric field that is equal to the anode voltage divided by the emitter to anode distance. Thus increasing this distance is equivalent, as far as anode current goes, to reducing anode field. The present data was collected at three anode positions "low" (about 10 mm), "mid." (about 18 mm), and "hi" (about 30 mm), corresponding to high E_A, mid E_A and low E_A respectively. The

measurements were made on a 20x20 array, characterized on fig. 5.19-20. In all the measurements, V_G=V_F, and V_A = 1000 V.. Since FE fluctuation makes the data inherently noisy, it is impossible to illustrate the effect of anode proximity by current values for a single value of voltage and varying anode heights.

The overall trend of current in figures 5.33 (decreasing) and 5.34 (increasing) is due to emission current increasing and coming to dominate leakage current (as illustrated on Figure 5.36), it is not related to the phenomenon we are investigating here. The effect that we are looking at – split of FE current between different electrodes – is thus best manifested near V_G = 100 V. It is seen that going from low to medium anode height leads to a much smaller change (esp. in gate current) than going from medium to high. The first step is equivalent to going from V_A =1000 V, to V_A = 500 V (see fig. 5.14-16), which is still on the flat part of the curve. While the change from low to high (from 10 mm to 30 mm) is equivalent to going down to VA = 300 V, which is the beginning of the transition region. We would expect a much greater difference for anode distances of 40-60 mm. (Physical limitations in the setup confine anode separation to 30 mm.) From the viewpoint of electron capture by gate and focus electrodes, the situation is identical to the measurement of output characteristics (p.81). The discussion given there still applies and explains why the focus electrode captures more current than the gate electrode.

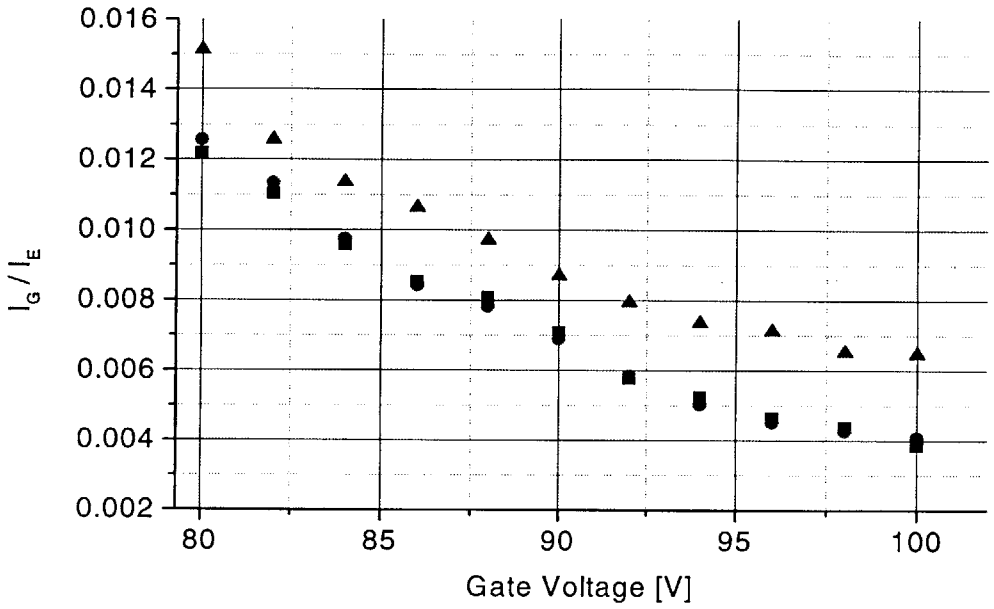

Figure 5.33 The ratio of gate current to emitter current for varying anode heights. ▲ -- low E_A; ● -- med. E_A; ■ -- high E_A

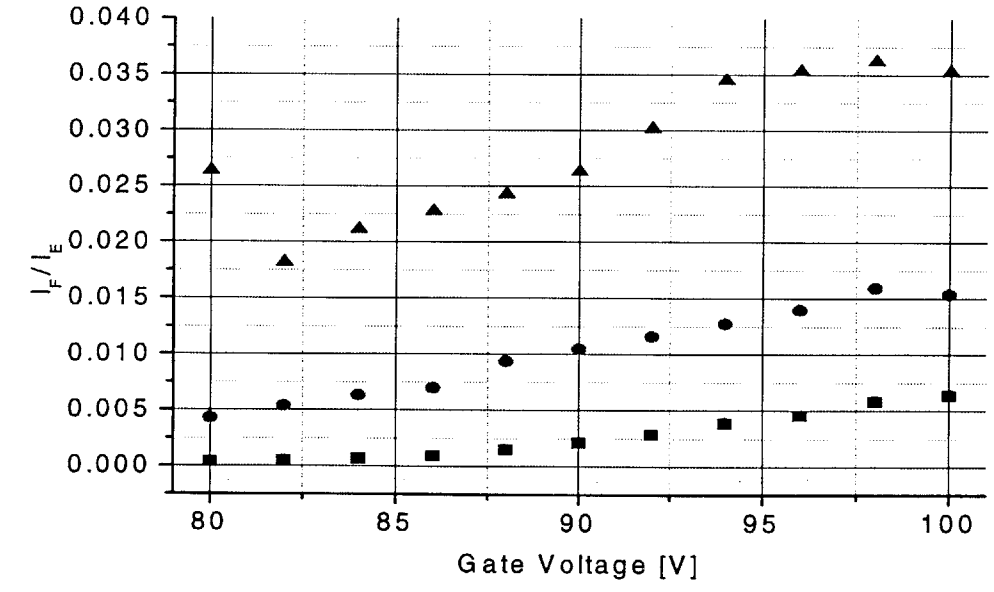

Figure 5.34 The ratio of focus current to emitter current for varying anode heights. ▲ -- low E_A; ● -- med E_A; ■ -- high E_A

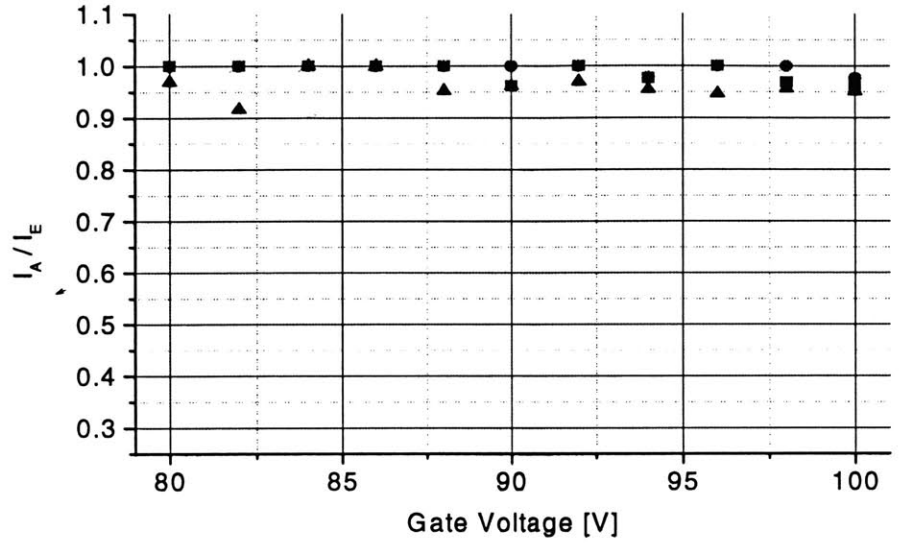

Figure 5.35 The ratio of anode current to emitter current for varying anode heights. ▲ -- low E_A; ● -- med. V_A; ■ -- high E_A

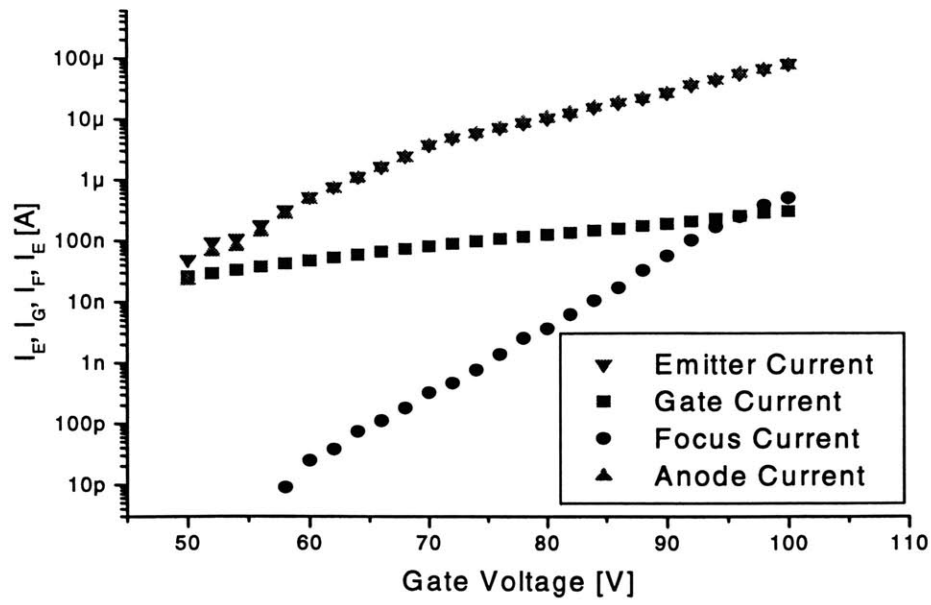

Figure 5.36 Currents vs. Gate Voltage for low E_A. Gate current is dominated by leakage. This figure explains the global trends in Figure 5.27, 5.28 and 5.30.

5.4.C Oxide breakdown

There are two principal modes of oxide breakdown – constant voltage and constant current. In the constant voltage breakdown, voltage across the oxide is increased until at some voltage value, the oxide undergoes a dielectric breakdown. In the constant current mode, a constant current is pumped through the oxide and after a certain time the oxide undergoes dielectric breakdown. So far, we have investigated constant voltage breakdown of the gate to cathode oxide and focus to gate oxide. The two oxides showed different breakdown behavior. We measured two kinds of devices – square pads with 200 micron sides and 400 micron sides.

To measure breakdown of the gate oxide (thermal oxide, 1 micron thick), we increased gate voltage from 0 to 500 in steps of 10 or 25 Volts. Above 250 Volts, the leakage current began to steadily increase, and around 425-500 Volts, the oxide suffered a dielectric breakdown, with leakage current increasing above 10 mA (the compliance value for the instrument.) Oxide breakdown is irreversible, i.e. lowering the voltage back

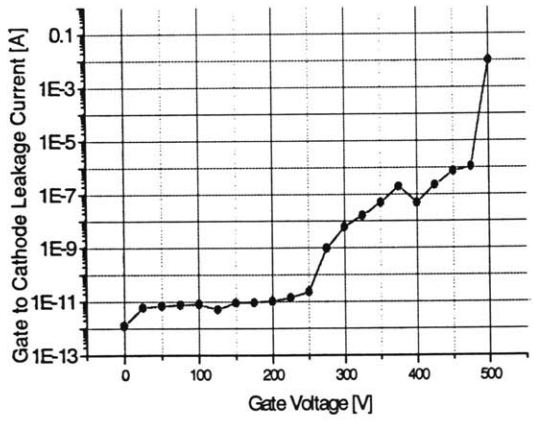

Figure 5.37 Dielectric breakdown for a 200x200 μm gate oxide pad.

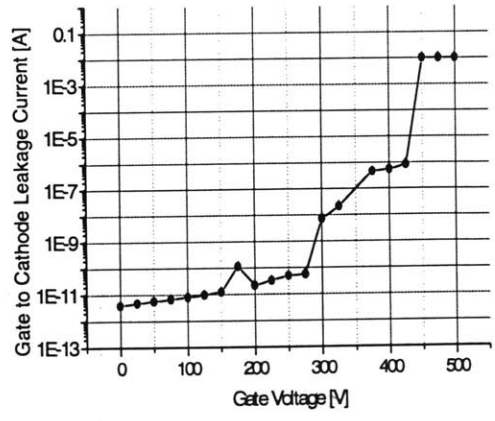

Figure 5.38 Dielectric breakdown for a 400x400 μm gate oxide pad.

down does "revive" the oxide. Figures 5.37-38 show the results for a 200 micron side pad and a 400 micron side pad. Note that the 200 micron has a breakdown voltage of 500 V, slightly higher than that for the 400 micron pad (450 V). This translates into breakdown strengths of $5x10^6$ V/cm and $4.5x10^6$ V/cm respectively. Figures 5.37-5.38 show that the maximum operating point at which the leakage current is negligible is about $2x10^6$ V/cm.

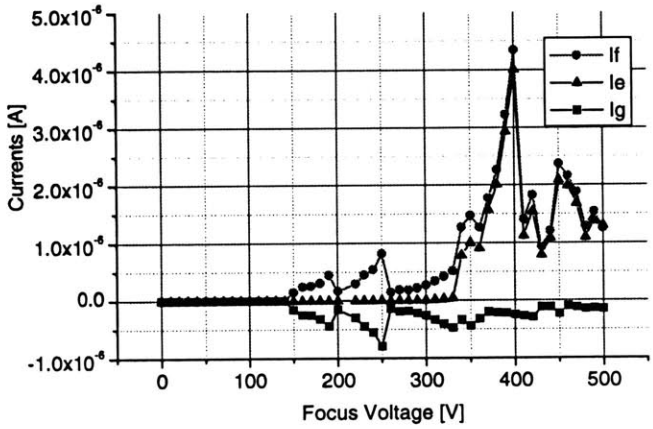

Figure 5.39 Dielectric breakdown of gate-to-focus oxide on a 200 μm pad. (Cathode, gate and focus currents are shown.)

Gate-to-focus isolation oxide was about 0.5 microns thick and consisted of densified low-temperature oxide on top of a thin layer of thermal oxide of polysilicon. To measure its breakdown, we made probe contact to gate and focus electrode and then increased the focus voltage while keeping gate voltage

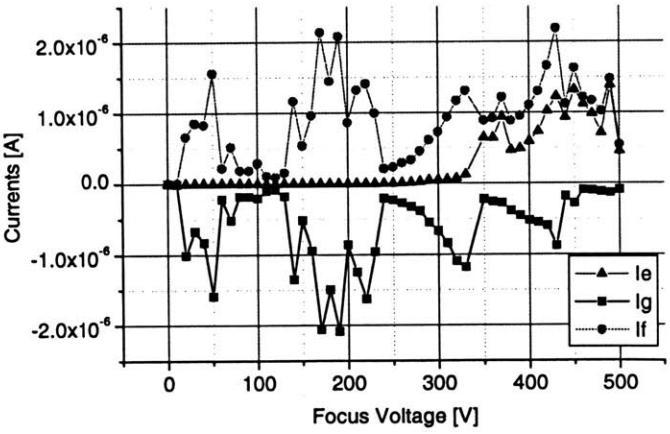

Figure 5.40 Dielectric breakdown of gate-to-focus oxide on a 400 μm pad. (Cathode, gate and focus currents are shown.)

constant. Again square pads with 200 and 400 micron sides were measured. Since this oxide is twice as thin as the gate oxide, and in addition consists of LTO, which has a lower dielectric strength than thermal oxide,

we expected a lower breakdown voltage. However, for voltages up to 500 V, no absolute breakdown (such as one in fig. 5.37-38) was observed at all. As shown on Figures 5.39-40, focus leakage current does not even systematically increase with focus voltage. Moreover, the data shows that the focus electrode draws some of its current directly through the cathode. (This current path can be eliminated by disconnecting the cathode contact, which would make the measurements easier to interpret. However, the present setup is how the device normally operates.) The breakdown of the focus isolation oxide is particularly critical since it determines the lifetime of IFE FEA operating in the focused mode. The preceding data poses several questions which we are presently unable to answer, namely: why does the focus leakage current decrease abruptly? (This cannot be due to contact burn out because the current then goes back up.) How does focus isolation oxide withstand 500 V (10^7 V/cm) without undergoing a dielectric breakdown? Understanding this topic would require further investigation.

5.5 Preliminary Optical Characterization

Evaluating the focusing performance of the devices involves replacing the anode with a phosphor screen and observing the size of the spot produced by a FEA as a function of focusing voltage. (There may be a non-optical way to examine the collimation of the beam, namely, using the effect of probe proximity, described in section 5.5.A. A beam well collimated by the focusing electrode may be less susceptible to probe interception.) At present, I could only carry out a preliminary investigation, since the instrumentation for measuring and recording the spot size is not installed yet.. Two pictures of the phosphor screen showing a light spot from FEA emission are shown on fig. 5.41-42. (The pictures were taken with a digital camera.) To achieve a visibly obvious reduction in spot size, focus voltage had to be reduced down to 25 V, 75 Volts below gate voltage. This caused anode current to drop from 10 μA (fig. 5.41) to 0.5 μA (5.42). Raising the current back to 10 μA required increasing the gate voltage to 130 V, at which point the spot produced on the phosphor screen was still smaller than in the unfocused state, but approximately equally bright. However, with V_G = 130 V and V_F = 25 V (i.e. a field of approximately $2x10^6$ V/cm applied across the gate-to-focus dielectric) the 100 Volt difference between the gate and the focus made the device easily subject to breakdown, so we were not able to take a picture of this configuration. This illustrates that reliable focusing probably requires devices with lower operating voltage or better gate-to-focus isolating layer.

Figure 5.41 Unfocused. Vg = Vf = 100 V; I_A = 10 μA

Figure 5.42 Focused. Vg=100 V; Vf = 25 V; I_A = 0.5 μA

5.6 Comparison of Results with Prior Work

Based on the discussion in the preceding chapters and sections, we identify a list of parameters by which to gauge the performance of IFE FED. Electrical performance, reliability, stability, and, perhaps, the most important – optical performance – are to be investigated.

Of all the prior works discussed in Chapter II, the present project comes closest to Itoh's device [1], that also utilizes local, out-of-plane focusing. As shown in Table 6.1, both gate and focus apertures of our device are about one third smaller than those of the Si tip devices (line 1). This advantage should contribute to lower turn-on and operating voltages, as well as to higher emission current. On the average, our devices do indeed show a slightly lower turn-on voltage (line 2); however, the per tip current is much lower than that in Si tip devices (line 3). The explanation of this poorer performance may lie in another performance parameter, namely, uniformity (scaling of total array current with the number of tips in the array) (line 4). Emission from arrays of Si tip devices is very uniform, i.e. the total current is almost proportional to the number of the tips in the array. This suggests that most of the tips contribute almost equally to the total array current. On the other hand, emission uniformity of our metal tip devices is poor, the total current is virtually independent of the size of the array. Apparently, only a small fraction of the total number of tips are functioning; thus, the per tip current (obtained by dividing the total array current by the number of tips) is low. The most likely cause of this non-uniformity is a large spread in the radii of curvature of metallic tips. This assumption, supported by SEM examinations, may point to a fundamental disadvantage of metal tips

fabricated with the Spindt cone process. Since the cones are formed by thermal evaporation of metal, there are several factors that inevitably lead to non-uniformity – particle size, dynamics of the final stages of aperture closing, and metal redistribution on the tip surface. This problem is very difficult to overcome if one wants to obtain uniform arrays of *sharp* tips. For example, any thermal treatment (e.g. "reflowing") is likely to remove the sharpest points.

One advantage of the Spindt cone process is the possibly of using thermal oxide, which has the best insulating properties of all silicon oxides (line 5), as the gate dielectric. Thus, ultrastrong gate dielectric in our devices in probably responsible for very low gate to cathode leakage (line 6), about 10 times lower than in the Si tip devices.

However, the gate-to-focus insulating layer, made of densified LTO, proved to be susceptible to breakdown (line 7). Given the typical gate operating voltage of 80-100 V, effective focusing required reducing the focus voltage to around 25 Volts, leading to fields of about 10^6 V/cm across the gate-to-focus isolation layer and quickly causing device breakdown. On the other hand, Si tip devices used the same kind of oxide for both isolation layers and demonstrated stable performance in the focusing mode. To achieve a similar performance in our metal tip devices, we need to first understand the mechanisms of oxide breakdown, which our measurements (described in Section 5.3c) did not fully elucidate. Reducing the operating voltage is another approach to eliminating device breakdown.

Thus, in the ultimate test of IFE FEA performance – optical characterization – our devices showed inferior performance. We did observe effects of focusing; however, we could not achieve stable, prolonged operation in the focusing mode without the device

breaking down (line 10). Moreover, effects of current suppression by the focusing electrode were less pronounced in the Si tip devices (line 8).

One problem that plagued both devices was temporal instability of the emission current. This is to be expected since fluctuations are inherent to field emission. However, in a subsequent work [Ref. 2.7], Itoh and co-workers demonstrated the possibility of overcoming the temporal instability by integrating a transistor with the FEA. Addition of a transistor is expected to similarly improve the performance of our metal tip IFE FEA's.

Table 6.1 Comparison of performance of our device and a Si tip IFE-FEA [Ref. 2.1]

#	Criteria for comparing performance of IFE FEA's.	Stacked Double Gated Si Tips [1]	Our devices: stacked double gated Cr/Mo tips
1	Gate aperture radius [μm] Focus aperture radius [μm]	1 1.5	0.7 0.95
2	Turn-on voltage [V];	55-75	42-56V (except single tip – 72V)
3	Emission current at 80V [μA]	2.4 (5x5 array)	10 (best 20x20)
4	Uniformity (scaling of total array current with the number of elements in the array)	very good (array current almost proportional to the number of tips)	poor (array current virtually independent of the number of tips)
5	Oxide leakage and breakdown resistivity (Ω cm) at 1 MV/cm	5×10^{8}	$< 4 \times 10^{11}$ (thermal ox.) 1×10^{7} (LTO)
6	I_G/I_E I_F/I_E	<5% <1%	0.5 % [fig 5.27] 0.6% [fig. 5.28]
7	Susceptibility to breakdown under normal operating conditions	low	moderate-high (large voltage difference between gate and focus have caused breakdown)
8	Emission current dependence on focus voltage	moderate dependence	strong dependence
9	current stability over time	poor (but improved greatly by integrating a stabilizing transistor [7]	poor (maybe can be improved by longer burn-in time)
10	Optical performance (change in spot size with focus voltage)	reliable, continuos decrease of spot size with focusing voltage to a max of >10x reduction in spot size	demonstrated focusing, but performance is unstable and unreliable

CHAPTER 6

THESIS SUMMARY

The ultimate goal of the project was to overcome the problem currently facing the Field Emission Display, namely, the trade-off of brightness and luminous efficiency versus display resolution. Making FED's with higher brightness and luminous efficiency requires increasing the cathode-anode separation. This impairs display resolution due to pixel-to-pixel crosstalk that results from the inherent spread in the field emission current beam. We attempted to overcome this problem by collimating the field emission current beam with a focusing electrode that was incorporated into the field emission unit cell by a microfabrication process.

Before starting fabrication, we made a comprehensive survey of the possible focusing geometries and narrowed down our choice to the out-of-plane local focusing geometry because it had the potential for the most effective focusing. To gain a further insight into the performance of a IFE FEA (integrated focusing electrode field emission array), we constructed an analytical model of the device, which produced (i) a simple closed form solution for the electric field at the tip of the field emission cone and (ii) a solution for the electric field throughout all space that enabled us to calculate electron trajectories. Most importantly for device design, the formulas derived from the model highlighted the effects of various parameters of device geometry on device performance.

We have successfully fabricated a IFE FEA and demonstrated that the focus electrode does produce a better collimated electron beam. In addition, we carried out

extensive electrical characterization of the IFE FEA, which is electrically different from regular FEA's because it is a four-terminal device. To our knowledge, this is the first comprehensive characterization of the 4-terminal FEA.

Thus, the project has become a step toward fabricating the Field Emission Display with improved resolution. One major issue we need to address to make our device suitable for a display application is device instability and susceptibility to breakdown. If the device was left in the focusing mode for more than a few minutes, it was destroyed by breakdown between the gate and focus electrodes. Further investigation is needed to determine the exact mechanism of breakdown, which could be due to dielectric breakdown of the gate-focus isolation layer, surface leakage, or other factors. Depending on the cause of breakdown, device performance may be greatly improved by (i) improving the quality of oxide in the gate-focus isolation layer or (ii) cleaning or baking out the device to eliminate mobile ions on the surface that cause surface leakage.

An additional contribution to breakdown, and otherwise a drawback of device performance, was a rather high operating voltage. It is possible to reduce the operating voltage by decreasing the diameter of the gate aperture, which at 1.4 μm was about 0.4 μm higher than the limit of the lithography equipment in the lab. However, another major cause of the high operating voltage probably came from the non-uniformity in the tip radii of curvature, which led to the situation where only a small fraction of the tips in the array were actually functioning. It is hard to make uniform metal tips; however, as evidenced by several prior works, improved uniformity can be readily achieved by going to silicon tips formed by undercut technology.

2970-03